BER the international journal of bridge engineering management and research

Editorial
Inaugural Issue of the International Journal of Bridge Engineering, Management and Research (IJBEMR)

Anil K. Agrawal, Dist. M. (ASCE), Ph.D., P.E.

Editor-in-chief, International Journal of Bridge Engineering, Management and Research,
Herbert G. Kayser Professor of Structural Engineering
The City College of New York, New York, NY, 10031

Submitted: 22 August 2024 **Accepted:** 24 August 2024 **Publication date:** 03 September 2024

DOI: 10.70465/ber.v1i1.10

It is my pleasure to serve as Editor-in-Chief (EIC) or Chief Editor (CE) of the newly established International Journal of Bridge Engineering, Management and Research in partnership with FABRE Consortium[1], which is a collaboration among Italian universities to promote and coordinate the participation of universities and consortium research institutions in scientific activities in the fields of Civil Engineering and Architecture, with particular reference to the evaluation of bridges, viaducts, and other structures.

The International Journal of Bridge Engineering, Management and Research (BER) is a fully open access online-only journal. It serves as a forum for the publication of scientific and technical papers related to all aspects of bridge engineering and management, including structural, seismic, hydraulic and geotechnical risk analysis, structural health monitoring, static and dynamic assessments, structural retrofitting, and resiliency enhancement. The journal also publishes research papers on tunnels focusing on the areas mentioned above. However, the journal does not consider papers that are purely related to construction technology, construction management of bridges and tunnels, and railway engineering. Technical research papers and case studies dealing with innovative technological or computational solutions to bridges and tunnels, as well as experimental methods and novel design and theoretical analysis procedures are strong candidates for publication in the journal.

It was possible to establish this journal only through extensive discussions and collaborative work with colleagues at FABRE Consortium, particularly the managing editors, Dr. Filippo Ubertini (University of Perugia, Italy), Dr. Francesco Ballio (Polytechnic University of Milan, Italy), Dr. Gianfranco De Matteis (University of Campania "Luigi Vanvitelli," Italy), Dr. Carmelo Gentile (Polytechnic University of Milan, Italy), Dr. Carlo Pellegrino (University of Padua, Italy), Dr. Vincenzo Simeone (Polytechnic University of Bari, Italy) and Dr. Paolo Clemente (FABRE Consortium, Italy). I am grateful for their extensive support and collaboration in establishing the journal. I am also very thankful to Dr. Walter Salvatore, President of the FABRE Consortium and Professor at the University of Pisa, Italy, for providing financial support to establish the journal. While the current editorial team has been instrumental in laying the foundation of the journal, we are in the process of establishing an international editorial board to outreach authors and reviewers worldwide so that the journal could highlight progress in bridge engineering technology from all parts of the world.

The review policy of the journal is double-blind (i.e., both author and reviewer identities are not disclosed). The decision to accept or deny a paper is based on review comments from reviewers. The editorial board of the journal has final discretion on the final decision on a paper. However, authors can appeal the decision. In that case, a declined paper will be allowed a second review by a different set of reviewers, which will be the final round of review for that paper.

Although there are several journals that publish articles in bridge engineering, the mission of this journal is to provide the authors and readers a platform that will harness innovative concepts through the use of Generative Artificial Intelligence (AI) in all our published papers. While our peer review process for all articles will ensure the confidentiality of reviewers' identities, we plan to disclose technical discussions through an attachment linked to the published articles during the peer review process. We are also preparing the journal to be indexed by SCOPUS and other engineering journal indexing databases and be assigned an impact factor once the journal meets the eligibility criteria; all papers published in the journal will be indexed by Google Scholar and other open indexes automatically in the meantime. Our journal is hosted on the the Public Knowledge Project's (PKP) Open-journal systems (OJS), which is a versatile

Discussion period open till six months from the publication date. Please submit separate discussion for each individual paper. This paper is a part of the Vol. 1 of the International Journal of Bridge Engineering, Management and Research (© BER), ISSN 3065-0569.

[1] https://www.consorziofabre.it/en/homepage/

open-source, open-access system used by more than 30,000 journals worldwide. We are proud to partner with PKP to offer all the important and useful functionalities of a journal for disseminating new scientific knowledge as widespread and easy as possible.

Our peer-review policy requires that every paper be reviewed by at least three expert reviewers. A paper with insignificant technical contributions will be declined immediately, while decisions on other papers will be based on the final recommendation of peer reviewers as the paper undergoes the review process. Once accepted, the paper will be published within four weeks of final acceptance and will be assigned to an issue of the journal on a quarterly basis. All our published papers undergo rigorous editing for both language and production quality.

In this inaugural issue of the journal, we are pleased to bring to you five papers in innovative areas of bridge engineering. The paper entitled "**Sensing Skin Technology for Fatigue Crack Monitoring of Steel Bridges: Laboratory Development, Field Validation, and Future Directions**" by Liu, Han et al. presents an innovative sensing skin technology for discovering new fatigue cracks, which are generally difficult to detect because of the highly localized nature of the sensors currently being used. This sensing skin consists of soft elastomeric capacitors (SECs), which are large-area strain gauges that transduce strain into a measurable change in capacitance. This sensor can be easily deployed over large surfaces and thus can be used to discover new fatigue cracks. The technology has been developed and characterized in a laboratory environment over the last decade. It has been recently deployed in the field on a bridge located in Kansas, USA. This paper presents and discusses technological updates that were necessary to enable field deployment, with the objective of supporting the field deployment of the SEC and other SHM technologies.

The paper entitled "**Seismic Fragility and Risk Assessment of Reinforced Concrete Bridges Undergoing Elastomeric Bearing Deformations Induced by Landslide**" by Ruggieri, Sergio et al. presents a comprehensive study on the seismic fragility of Reinforced Concrete (RC) bridges isolated by elastomeric bearing devices subjected to differential displacements induced by slow-moving landslides. The seismic behavior of isolated bridges is ruled by the performance of elastomeric bearings to reduce and dissipate earthquake actions. These bridges are subjected to service loads that usually are accounted for in the design, but possible additional actions from the surrounding environment, such as landslides affecting substructure components, can seriously undermine their seismic response. The paper describes a practical approach to investigate the seismic fragility and risk of RC bridges isolated by elastomeric bearings, which may undergo early deformations induced by the differential displacements of substructure components. The study shows that it is possible to quantify the influence of landslide-induced effects on seismic fragility and risk by using only two numerical models in order to provide decision support to transportation authorities responsible for ensuring the safety of bridges and road networks. The proposed approach has been evaluated on a real-life case study, the *Santo Stefano* Viaduct in Italy, which was subjected in the past to relevant deformations of the elastomeric bearings due to an active landslide phenomenon.

The study entitled "**A New Methodology for the Diagnosis and Monitoring of Bridges Under Slow Deformation Phenomena**" by Meoni, Andrea et al. presents a comprehensive study on the onset of damage and collapse mechanisms during low deformation phenomena due to landslides. Timely identification of slow deformation phenomena on bridges and viaducts, as well as the evaluation of their extent and evolution over time, are therefore of crucial importance for preserving the safety conditions of road networks. In common practice, the preliminary analysis of slow deformation phenomena could be carried out over large geographical areas; hence, it can be used by managing institutions to set intervention priorities among the assets under their responsibility. This paper proposes a new methodology for the diagnosis and monitoring of bridges under the effects of slow deformation phenomena based on the combined use of Synthetic Aperture Radar Interferometry (InSAR) techniques, visual inspections, geometric surveys, destructive and non-destructive testing methods, and numerical analyses. Specifically, InSAR is adopted to remotely identify bridges affected by slow deformation phenomena within large geographical areas/road networks. A practical application of the proposed methodology for the diagnosis and monitoring of a curved roadway bridge subjected to landslide phenomena is presented in the paper. The results obtained in the case study provide a sound demonstration of the effectiveness of the proposed approach.

The paper entitled "**Seismic Resilience Assessment for Steel-Concrete Composite Bridges Including Impacts of Near-Fault Earthquakes**" by Liu, Yang et al. proposes a seismic resilience assessment method for steel-concrete composite bridges (SCCB) subjected to near-fault earthquake hazards. Based on conventional probabilistic seismic hazard disaggregation analysis, a correction factor is defined to represent the proportion of the occurrence probability of the near-fault pulse-like, near-fault non-pulse-like, and far-field earthquake conditioned on a given intensity level concerning the total occurrence probability of all earthquakes. The parameters of functionality recovery functions are modified using the factor proposed, and then the restoration processes after each type of earthquake are estimated. Correspondingly, vulnerabilities of a typical SCCB under near-fault and far-field earthquakes are developed as a case study. Based on the seismic hazard and fragility results, the seismic risk for each type of earthquake in a 50-year horizon is estimated. After that, the modified functionality recovery function is derived from the expected functionality. To implement the proposed method, the expected seismic resilience indices of a typical SCCB involved in the SEQBRI project are estimated, and the seismic resilience assessment is conducted. The seismic resilience assessment without considering earthquake type is also conducted for comparison analysis using the same bridge. The result shows that the seismic resilience of bridges in near-fault earthquake scenarios can be analyzed by the method proposed, and reducing the structural vulnerability under low-intensity level earthquakes and improving

the structural recovery efficiency for slight and moderate damage states are more meaningful to enhance the seismic resilience of bridges.

Finally, the last paper on "**Demand Model for Concrete Barriers Subject to Tractor Tanker-Trailer Impact**" by Cao, Ran et al. presents results on Test-Level 6 (TL-6) barriers for bridges. Test-level-6 (TL-6) barriers are specified in the U.S.A. for situations that involve a high percentage of truck traffic or unfavorable site conditions, where truck rollover or penetration beyond the railing could result in severe traffic consequences. Previous studies of TL-6 barriers impacted by tractor tanker-trailers (the truck category that creates the highest impact demands) assumed that the barriers behave rigidly. The rigid barrier assumption is investigated in this paper through simulation studies in which validated nonlinear models of the truck and barrier are employed. Parametric simulations are carried out to evaluate the effects of truck velocities, weights, and barrier heights on the impact force demands. The demand model in the current design guideline is critiqued based on the simulation results, and a discrepancy was found between the predicted barrier performance by AASHTO-LRFD loading and the truck impact. A revised demand model is proposed based on the simulation results.

All these five papers have gone through a rigorous peer review process of the journal and present innovative research in bridge engineering. They are openly accessible from the journal website and can be downloaded freely.

With this editorial note, it is also my pleasure to invite you to submit your papers addressing research with new and substantial contributions in bridge engineering to the International Journal of Bridge Engineering, Management and Research. The journal is committed to a prompt peer review process and online publication of the paper within four weeks of acceptance. We also are committed to completing our peer review process within 90 days of paper submission.

BER the international journal of bridge engineering management and research

Sensing Skin Technology for Fatigue Crack Monitoring of Steel Bridges: Laboratory Development, Field Validation, and Future Directions

Han Liu[1,*]; Simon Laflamme[1,2]; Jian Li[3,4]; Austin R. J. Downey[5,6]; Caroline Bennett[3]; William N. Collins[3]; Paul Ziehl[5,6]; Hongki Jo[7]; and Michael Todsen[8]

Submitted: 26 January 2024 **Accepted:** 10 June 2024 **Publication date:** 03 September 2024

DOI: 10.70465/ber.v1i1.8

Abstract: A significant number of steel bridges are vulnerable to fatigue cracks, and the timely discovery of damage is critical in ensuring safety and continuous operations. Despite various crack monitoring methods available in the field of structural health monitoring (SHM) to empower real-time feedback, few commercially-available technologies are applicable to the task of discovering new cracks because of the highly localized nature of the sensors. The authors have developed a sensing skin constituted of -soft elastomeric capacitors (SECs). An SEC is a large-area strain gauge that transduces strain into a measurable change in capacitance. It can be easily deployed over large surfaces and thus can be used to discover new fatigue cracks. The technology has been developed and characterized in a laboratory environment over the last decade. It has been recently deployed in the field on a bridge located in Kansas, USA. The aim of this paper is to present and discuss technological updates that were necessary to enable field deployment, with the objective of supporting the field deployment of the cSEC and other SHM technologies. In particular, it reviews the following SEC technology modifications: 1) corrugation of the surface of the dielectric, creating a corrugated SEC or cSEC, to improve sensing performance; 2) development of a dedicated wireless data acquisition system; and 3) improvement of the data fusion algorithm to account for higher signal contamination in the field. After this review, challenges in conducting field deployment are examined. Lastly, a discussion on the path to commercialization is provided.

Author keywords: Structural health monitoring; soft elastomeric capacitor; capacitive sensor board; fatigue; steel bridges

Introduction

Fatigue cracks are one of the primary mechanisms that may compromise the structural integrity of steel bridges.[1] Timely detection, evaluation, and repair of fatigue damage are necessary for ensuring safe and continuous operations by preventing excessive deterioration and catastrophic failures.[2,3] Visual inspection is the most common approach used for fatigue crack detection, but this process relies on the inspector's judgment and thus presents challenges for early-stage hairline-thin crack detection because of low contrast between the crack and the adjacent metallic surface.[4,5] Various nondestructive evaluation technologies have recently been proposed to assist visual inspections. Examples include magnetic particle,[6] ultrasonic,[7,8] computer vision,[9–11] and X-ray imaging.[12] While these approaches are well accepted by the bridge management community, they rely on the use of trained agents, are sporadic, and may be expensive and time-consuming to conduct.

A promising solution is to use structural health monitoring (SHM) technologies to automate the crack discovery and evaluation process by leveraging tailored signal processing and decision-making algorithms.[13,14] However, the use of conventional SHM technologies for fatigue crack discovery is difficult because the most available solutions are too small in size and have one-dimensional sensing capabilities, which makes the discovery of a crack unlikely from a probabilistic perspective,[15] with a few exceptions including acoustic emission technology.[16,17] To address this issue, researchers have proposed large-area electronics (LAE) that can be deployed as a dense sensor network, often termed sensing skin.[18,19]

*Corresponding Author: Han Liu. Email: liuhan@iastate.edu
[1]Department of Civil, Construction, and Environmental Engineering, Iowa State University, Ames, IA, USA
[2]Department of Electrical and Computer Engineering, Iowa State University, Ames, IA, USA
[3]Department of Civil, Environmental and Architectural Engineering, The University of Kansas, Lawrence, KS, USA
[4]Department of Electrical Engineering and Computer Science, The University of Kansas, Lawrence, KS, USA
[5]Department of Mechanical Engineering, University of South Carolina, Columbia, SC, USA
[6]Department of Civil and Environmental Engineering, University of South Carolina, Columbia, SC, USA
[7]Department of Civil, Architectural, Environmental Engineering and Mechanics, The University of Arizona, Tucson, AZ, USA
[8]Bridges and Structures Bureau, Iowa Department of Transportation, Ames, IA, USA

Discussion period open till six months from the publication date. Please submit separate discussion for each individual paper. This paper is a part of the Vol. 1 of the International Journal of Bridge Engineering, Management and Research (© BER), ISSN 3065-0569.

Specific examples of LAE developed for fatigue crack monitoring include piezoelectric sensor/actuator networks,[20] carbon nanotube-based sensing skin,[21] and strain sensing sheets.[22] Compared to commercially available strain sensors, sensing skins provide large area coverage, thus enabling direct damage discovery at pre-determined resolutions over large-scale components.[23,24]

The authors have previously proposed a soft elastomeric capacitor (SEC) technology. The SEC is a flexible, low-cost, compliant, and skin-type strain sensor that transduces strain into a measurable change in capacitance. A new generation of the SEC was recently proposed by texturing the top surface to ameliorate its sensing performance, termed corrugated SEC (cSEC).[25] The cSEC has been characterized and applied for monitoring fatigue cracks in steel compact, C(T), specimens[26] and corner welds,[27] and demonstrated in the field on a bridge located in Kansas, USA.[28] The aim of this paper is to present technological updates that were required to bridge the gap between laboratory studies[25–27] and field deployment.[28] Syntheses of sensor development work in the structural health monitoring community are rarely disseminated, and thus, the novelty of this manuscript resides in summarizing 15 years of research and development that led to a field demonstration. Through this overview of "lessons learned," the authors anticipate supporting further field implementations of new SHM technologies.

Fig. 1 presents an overview of key technological updates that were implemented. These are discussed sequentially in the sections that follow. First, the SEC itself was modified with a corrugated pattern to improve sensing performance in terms of signal-to-noise ratio and resolution, giving rise to the cSEC. Second, a dedicated wireless data acquisition system was designed to read and transmit capacitance data. Third, the signal processing algorithm, originally termed the crack growth index (CGI), was modified to improve accuracy and robustness with respect to real-world traffic loading and environmental noise (now termed "modified CGI"). Fourth, challenges in conducting field validation are reviewed. Fifth, a discussion on a path to commercialization is provided.

Sensing Skin Technology

Soft elastomeric capacitor (SEC)

The SEC is a robust large-area capacitor that transduces strain into a measurable change in capacitance. Its design, fabrication, and sensing principle are described in detail in

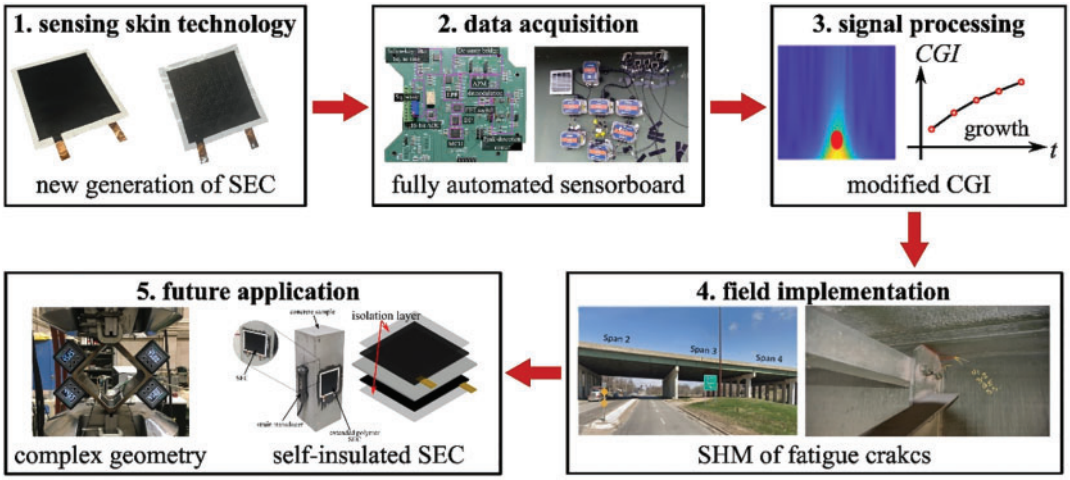

Figure 1. Overview of technological updates enabling field deployment of the SEC technology

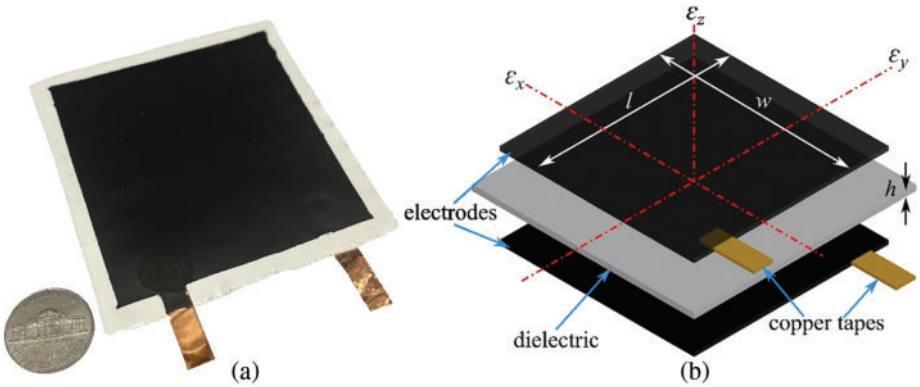

Figure 2. Picture of a 76 mm × 76 mm SEC; and (b) an exploded view of the sensor architecture with key components annotated

Laflamme et al.[29] Fig. 2a presents a square-shaped SEC of 76 mm × 76 mm. The technology is a flexible and stretchable parallel capacitor constituted by a dielectric layer sandwiched between conductive plates, as shown in Fig. 2b.

The dielectric layer of the sensor is fabricated by doping titania (TiO_2) particles at 7.5 w% into a block co-polymer matrix of styrene-ethylene/butylene-styrene (SEBS), used to increase permittivity and durability. The conductive plates (i.e., electrodes) are also constructed from an SEBS matrix but doped with carbon black particles at 2.5 w% to provide conductivity while improving the stability of SEBS against UV degradation. Two adhesive copper tapes are installed onto the top and bottom electrodes to enable the mechanical connection. Here, the top electrode is used as input to the data acquisition (DAQ) system, and the bottom electrode is used for grounding. The inclusion of the titania and carbon black is critical in providing the sensor with high durability and weatherability protection for field implementation.[30]

The SEC is an excellent technology for fatigue crack detection, localization, and monitoring of metallic structures. It can cover large areas in a networked configuration due to its high scalability arising from the use of readily available, inexpensive raw materials and its simple fabrication process. Its ultra compliance guarantees robustness and durability with respect to fatigue crack quantification and long-term monitoring. Assuming under a low measurement frequency (<1 kHz), the initial capacitance C_0 of the SEC is formulated as:

$$C_0 = e_0 e_r \frac{A}{h} \tag{1}$$

where $e_0 = 8.854\ \text{pFm}^{-1}$ is the vacuum permittivity, e_r is the dielectric permittivity, $A = w \times l$ is the sensing area of the SEC, with w and l being the width and length of the electrode, and h is the thickness of the dielectric, as denoted in Fig. 2b.

When installed over a fatigue crack, the opening and closing of the crack causes a geometric deformation of the sensor, thus provoking a measurable change in its capacitance. It is a remarkable fact that prior studies demonstrated that the sensors' signal can detect cracks in its vicinity, not only those located underneath.[9] Its electromechanical behavior, under the assumption of in-plane stress when deployed onto a steel surface, can be modeled as:[26]

$$\frac{\Delta C}{C_0} = \frac{1}{1-\nu}(\varepsilon_x + \varepsilon_y) \tag{2}$$

where ΔC is the measured differential change in capacitance, ν is the Poisson's ratio with $\nu \approx 0.49$ at small strain,[25] $\frac{1}{1-\nu}$ is the gauge factor λ, and ε_x and ε_y are the strains in the x and y directions, respectively. Eq. (2) reveals that ΔC varies linearly with the in-plane strains ε_x and ε_y, and thus its signal can be used to measure fatigue crack growth. That relationship in Eq. (2) assumes full adhesion of the sensor onto the monitored surface. When subjected to a fatigue crack, the sensor stretches over the opening of the crack and

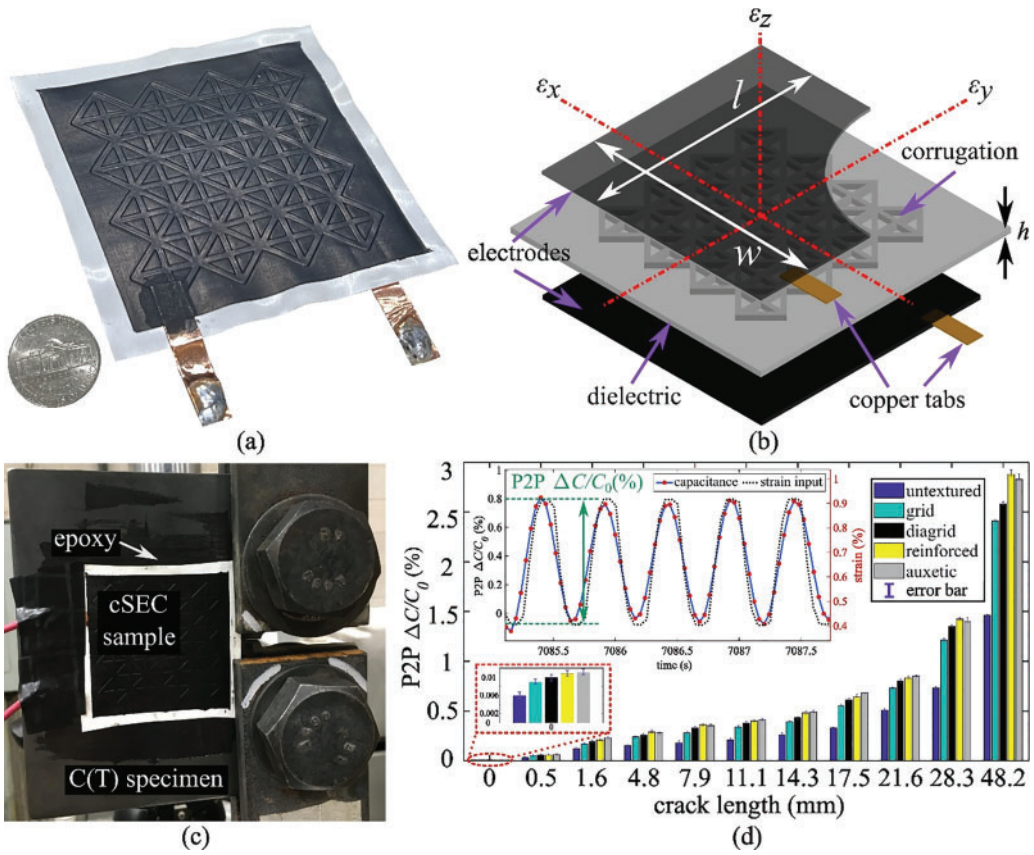

Figure 3. A cSEC with reinforced diagrid pattern; (b) schematic of the cSEC; (c) experimental setup showing a cSEC on a C(T) specimen; and (d) typical time series results of the P2P versus crack length under different corrugation patterns

measures the localized strain that significantly boosts the signal's magnitude.

Corrugated soft elastomeric capacitor (cSEC)

The design of the SEC has been altered recently to improve signal stability and sensitivity to facilitate field implementation. This was done by corrugating the top surface of the dielectric to tune the sensor's stiffness, resulting in lowering the sensor's Poisson's ratio and improving its mechanical stability. This new generation cSEC is shown in Figs. 3a and 3b. Its design, fabrication process, and electromechanical model were reported in Liu et al.[25] Experimental results conducted on C(T) steel specimens confirmed that the cSEC produces a net improvement in the sensing performance in terms of linearity, sensitivity, resolution, and accuracy.[26] A key result is presented in Fig. 3d for the experimental setup shown in Fig. 3c. Four corrugation patterns were investigated (symmetric grid, diagonal diagrid, reinforced diagrid, and re-entrant hexagonal honeycomb) and benchmarked against the original SEC, which was untextured. Experimental results were evaluated by cross-comparing the three-sample averaged peak-to-peak (P2P) amplitudes of the signals between each pattern over different crack lengths. Results are graphed in Fig. 3d. The cSEC exhibited an increase in the P2P amplitudes of approximately 50% to 100% when compared to the untextured SEC applied over various crack lengths. The reinforced diagrid pattern, depicted in Figs. 3a and 3b, was selected for field implementation because it 1) outperformed most other patterns in terms of sensitivity to crack opening and 2) was a symmetric design, thus making it easier to deploy in the field.

Data Acquisition

Experimental works on the SEC and cSEC used a wired commercial capacitance measurement device termed PCAP (model PCAP02). However, the use of a wired DAQ impedes the practicality of any field application because of added difficulties in installation, costly cabling, inefficient data transmission, high energy dissipation, and poor accessibility.[31] To this end, a dedicated, wireless DAQ was developed, consisting of a capacitive strain sensor board (c-strain board) integrated with a smart sensor platform (Xnode). The c-strain board is a De Sauty bridge-based capacitive strain sensing interface that can transform the strain-induced dynamic capacitance changes of the SEC into analog voltage signals.[32] Yet, the precise alternating current (AC)-bridge balancing, signal amplification control, and shunt calibration process associated with the c-strain sensor board operation were originally achieved manually, which also constitutes an important limitation to field deployments.[33] Fig. 4a shows the picture of the automated c-strain sensor board.

The newly developed capacitive strain sensing node was built by integrating the automated c-strain sensor board with a commercial wireless smart sensor platform, Xnode. The Xnode is the wireless transmission node that consists of a processor board, radio and power board, and the 24-bit data acquisition board in a layer-up configuration, as shown in Fig. 4b. It is known as a versatile wireless sensor system through its various functionalities: flexible interface with external sensors, low power radio transceiver (Atmel AT 86RF233), onboard dual-core signal processing (ARM cortex M0/M4), optional high quality of long-range wireless communication through 4G LTE module (Sierra Wireless HL7588 LTE-CAT4), expandable data storage, 24-bit analog-to-digital conversion (ADS131E8), user-configurable middleware software library, and so on Oliva et al.,[34] Hoang et al.,[35] Fu et al.,[36] Fu et al.[37] The Xnode also has a high-capacity lithium-ion rechargeable battery, which is here equipped with solar panel support to provide an autonomous energy source in the field (inset of Fig. 10d).

The performance of the developed wireless capacitance sensor in combination with the SEC was evaluated through free-vibration tests using a cantilever beam. The experimental setup is presented in Fig. 5a. Two cSECs of similar initial capacitance were adhered onto a steel plate using epoxy (JB Weld), and a foil-type strain gauge (OMEGA kFH-3-120-C1-11L3M3R) was installed between them for comparison. The automated c-strain sensor board and the wired commercial capacitance measurement device PCAP (PCAP02) were subsequently connected to the same SEC for data collection at 100 Hz, and the data from the foil-type strain gauge was recorded using a National Instrument CompactDAQ chassis (cDAQ-9178) with the NI9235 module at a sampling

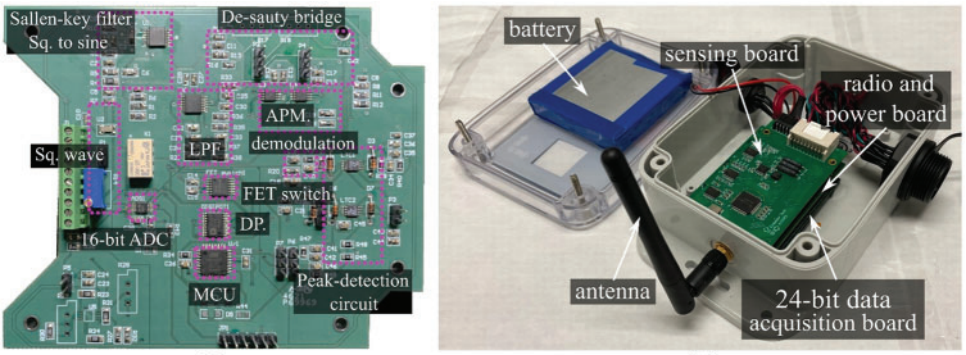

Figure 4. Wireless capacitive sensor node: (a) automated c-strain sensor board; and (b) Xnode smart sensor platform

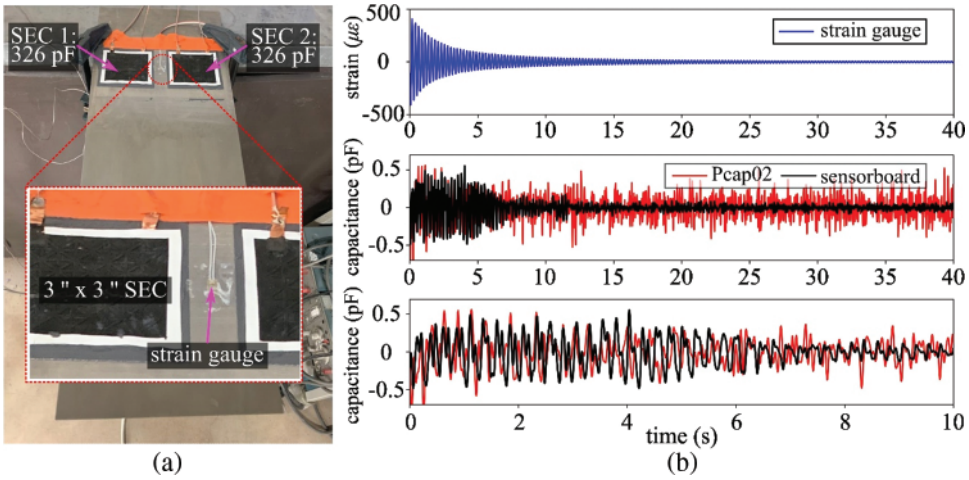

Figure 5. (a) Cantilever plate setup for free vibration test; and (b) experimental results comparing signal measured from strain gauge (top), PCAP02 (middle), and sensor board (bottom)

frequency of 2 kHz. The cantilever plate was subjected to free vibration generated by pushing down and releasing the free end of the beam, introducing about 400 micro-strains measured by the strain gauge, which was within the effective strain range experienced by a cSEC monitoring fatigue cracks in the steel. Fig. 5b presents the strain measured from the strain gauge and compares the signal collected by the c-strain sensor board and PCAP02. It can be noticed that both the sensor board and PCAP02 showed a very similar trend at the initial stage when the vibration amplitude was large. The sensor board's signal decayed was more similar to that of the strain gauge compared to the PCAP02 signal, exhibiting approximately 34% lower measurement noise. The fluctuation of the sensor board's signal after 10 seconds can be attributed to electromagnetic noise. More details about the c-strain sensor board and associated experimental tests can be found in Jeong et al.[33]

Signal Processing

A crack growth index (CGI) was initially developed to fuse SEC signals into a metric related to fatigue crack length. The CGI was taken as the ratio between the power spectral density (PSD) peak of $\Delta C\,(t)$ and the applied $F(t)$ to normalize $\Delta C\,(t)$ (i.e., removing the impact of the changing traffic load magnitude), making the CGI an input-independent metric.[38] Note that $F\,(t)$ can be any signal that relates to the input, for example the reading of a strain gauges measuring the axial strain of a member of the cross-frame of a girder bridge provoked by the passage of a vehicle.[39]

The original CGI works well for the proof-of-concept laboratory tests, where the $\Delta C\,(t)$ and $F(t)$ were both sinusoidal signals.[38] The CGI was further improved by introducing a moving-average filter to smooth the PSD curves to deal with signals with randomized frequencies and amplitudes.[40] However, traffic-induced bridge response measurements in the real world resemble impulse-like signals induced by individual vehicle passing, as opposed to sinusoidal signals, and they are subject to noise contamination, such as low-frequency drift likely arising from the intrinsic electrical behavior exhibited by many sensors fabricated using hyper-elastic polymers,[41,42] as exemplified in Fig. 12 that compares sensor measurements collected in the laboratory and in the field. These issues limited the success of using the Fourier transform in the CGI. Thus, the CGI was modified to utilize, instead, wavelet transform to accurately detect the amplitude of each individual impulse event that tracks potential fatigue crack growth under traffic load. The developed new CGI algorithm presents a complete system for long-term fatigue crack monitoring in the field with the procedure diagrammed in Fig. 6 and is conducted as follows:

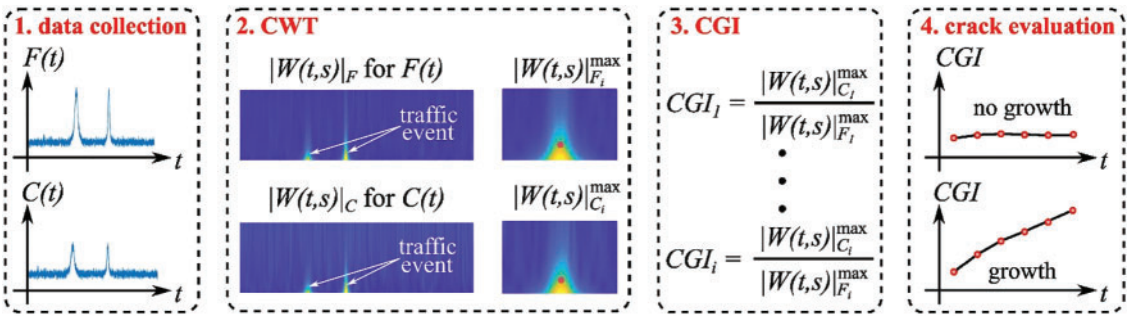

Figure 6. Workflow of the modified CGI algorithm

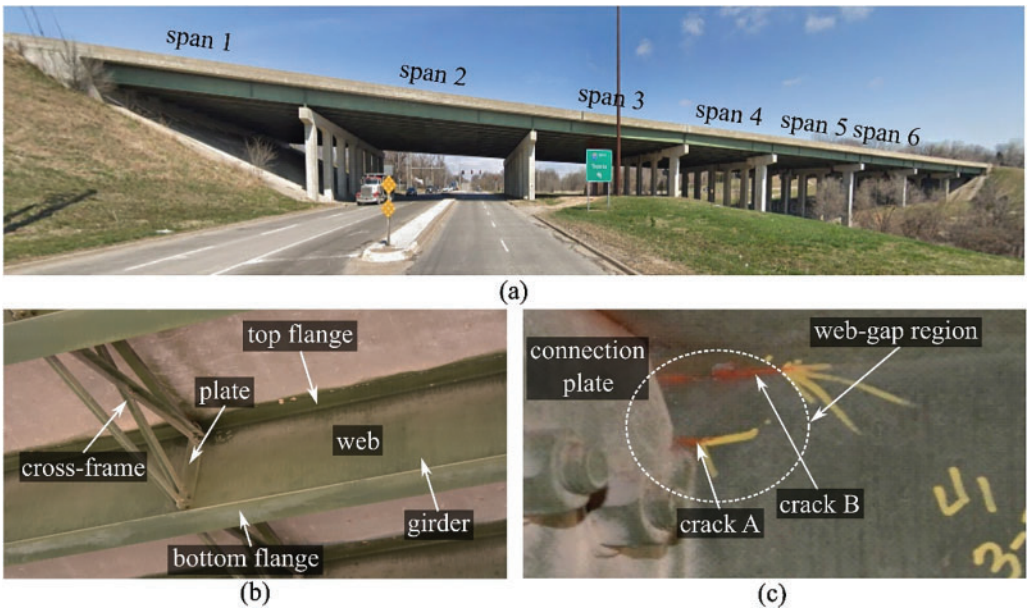

Figure 7. I-70 bridge: (a) span layout of the bridge; (b) cross-frame between the adjacent girders; and (c) detail of the web-gap region with distortion-induced fatigue cracks (adapted from Taher et al.[28])

First, traffic detection is conducted using an accelerometer installed on the bridge. When the acceleration is above a user-defined threshold, signals from the cSECs are collected, as well as that from a strain gauge, the latter of which is used to indirectly obtain $F(t)$. Second, a continuous wavelet transform using Morse wavelet is conducted on the signal and peaks in the data are identified. See references[43,44] for additional details on the wavelet transform technique. The signal is further processed within windows of interest $\text{WOI}_i = [t_i - t_d, t_i + t_d]$, where $i = 1, 2, \ldots, n$ represents the number of detected peaks n, and t_d is a time window separating peaks. Third, the maximum values from the capacitance $|W(t,s)|_{C_i}^{\max}$ and input $|W(t,s)|_{F_i}^{\max}$ signals within each WOI_i are extracted and represent the detected traffic events. An example of such an event is indicated by a pink dot in Fig. 6 (step 2). Third, the CGI is taken as:

$$\text{CGI}_i = \frac{|W(t,s)|_{C_i}^{\max}}{|W(t,s)|_{F_i}^{\max}} \tag{3}$$

Fourth, crack size and its growth are determined through a spatio-temporal study of the CGIs. Laboratory results reported in Kong et al.[38] showed a linear relationship between the CGI and the fatigue crack length. Therefore, the CGI would gradually increase if the crack grows. Otherwise, the CGI remains constant if there is no crack growth.

Field Implementation

The SEC was deployed in the field on a multi-span steel highway bridge. The bridge (Fig. 7a), designated 70-105-41732-128 (eastbound), is located at the intersection of N. 57$^{\text{th}}$ Street and I-70 highway near Kansas City, Kansas. According to the inspection report released by the Kansas Department of Transportation (KDOT), the bridge has multiple fatigue cracks. Fig. 7b shows a typical cross-frame (Span 3) connected to the girder web using a transverse connection plate. Span 3 was monitored, which had two distortion-induced fatigue cracks on one of the girders, as shown in Fig. 7c, where crack A is near the web-gap region along the weld between the transverse connection plate and the girder web, and crack B is along the weld toe between the top flange and web.

The field installation process (diagramed in Fig. 8) occurred as follows. First, SECs were installed on the web-gap region directly over the fatigue cracks, and foil-type strain gauges (FLA-5-11-3LJCT) were installed on the cross-frame to capture the out-of-plane force indirectly $F(t)$ acting on the web-gap region exerted by the cross-frame, proportional to the traffic loading. A direct current (DC) Wheatstone bridge circuit module, shown in Fig. 9a, was used to convert the strain ε to a voltage signal. The c-strain sensor board and DC Wheatstone bridge were connected to the SECs and strain gauge to measure analog voltage signals relating to $\Delta C(t)$ and $F(t)$. In this application, the $F(t)$ value corresponding to a 30 $\mu\varepsilon$ was selected as the event detection threshold, here, by heavy vehicles. A minimum peak distance $t_d = 1.3$ s was selected to avoid closely spaced peaks that would likely be caused by noise.

Second, the Xnode used in this work was equipped with an 8-channel 24-bit AD converter, in which the first three channels were used for the onboard tri-axial accelerometer, and the remaining five channels were used for external sensors such as the strain gauge and SECs. A breakout box, shown in Fig. 9b, was employed to connect both the c-strain sensor board and DC Wheatstone bridge module to the Xnode to split a multi-cable line into eight compound connectors, ensuring robust connections for power supply and receiving external sensor voltage signals, and supporting integration testing and troubleshooting processes.

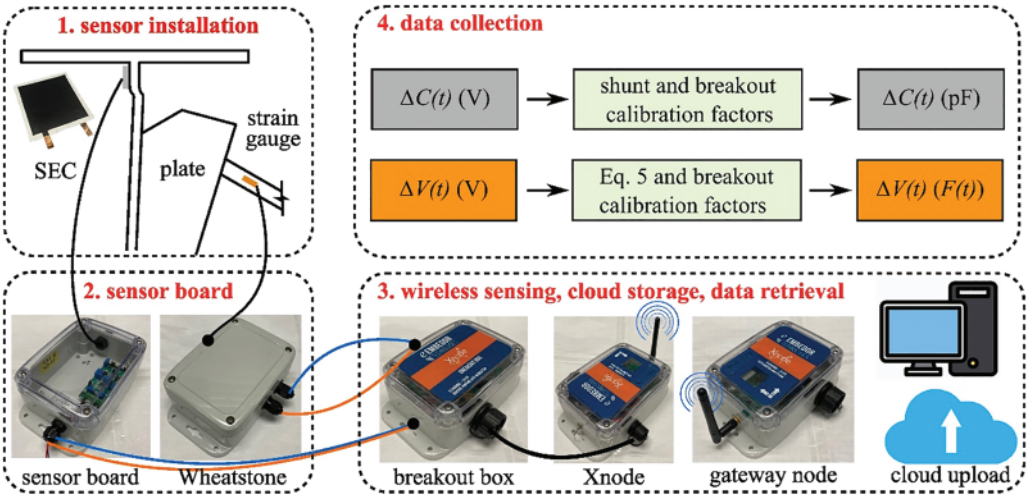

Figure 8. Developed in-field fatigue crack sensing flow chart

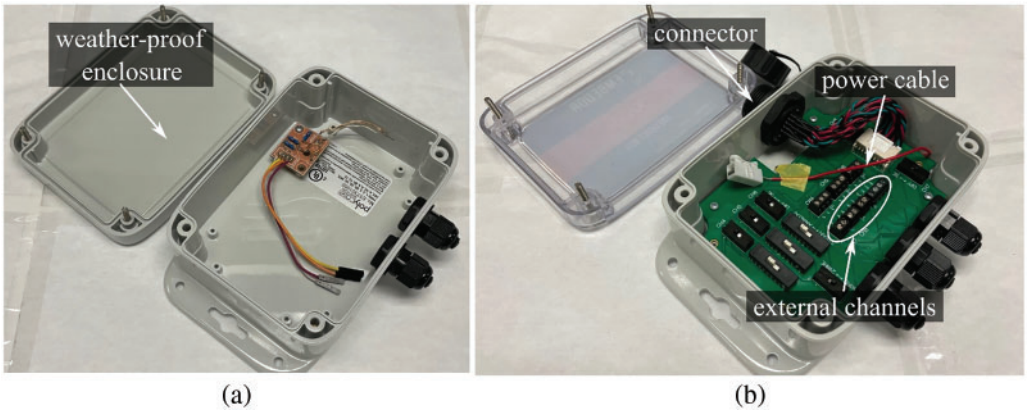

Figure 9. Pictures of (a) the DC Wheatstone bridge module; and (b) the breakout box

The Xnode was also equipped with a low-power trigger accelerometer (ADXL362 by Analog Devices) to enable event-triggered sensing mode with a predefined acceleration threshold. This event-triggered sensing mode is used to tailor data collection to meaningful events and to optimize the Xnode power usage. In this application, acceleration thresholds of 150 and 250 mg were selected depending on the stiffness of the structural components to ensure that only significant loading events were collected.

Third, a cellular gateway node was equipped with a 4G-LTE modem to receive the signals from the Xnode and to upload data to the cloud server for wireless communications and remote data retrieval.[35] Fourth, cloud data was accessed using a PC, and the desired $\Delta C(t)$ and $F(t)$ were obtained by applying the shunt calibration coefficients along with the breakout box factor on the voltage signals of $C(t)$ and $V(t)$, respectively.

Structural surfaces shown in Fig. 10a were sanded and cleaned to remove paint and debris prior to sensor installation. Subsequently, a thin layer of an off-the-shelf bi-component epoxy (JB Weld) was applied over the crack on the web-gap-region, and SECs adhered to the epoxy layer (Fig. 10b). Foil-type strain gauges were installed on a diagonal member (Fig. 10c) of the cross-frame with the Wheatstone bridge configuration using adhesive and coating. Fig. 10d is an annotated picture showing the installed sensor network under the first girder of Span 3, and the inset shows the facia side of the girder with cSECs installed. All components of the integrated system, except the capacitive sensor board, were deployed on the bottom flange of the girder. The capacitive sensor board was installed close to the cSEC to reduce cable length, thus minimizing the noise from capacitance measurement. Additionally, data analysis focuses on extracting the peaks associated with dynamic responses during a short period of time, which has a minimum impact from temperature change. After installation, AC bridge balancing and a two-step Shunt calibration were performed on the capacitive sensor board. All devices and sensor boards, except the cSECs, in this application were packaged in a weather-proof enclosure to improve durability and offer protection against environmental hazards. Prior work showed that the SEC was robust with respect to aging, attributable to the use of titania and carbon black, where the titania doped dielectric layer provides the sensor with a level of durability against weathering, while the carbon black inclusions to the conductive layer improved the sensor's durability and weatherability protection.[30] The bridge is not equipped with any other monitoring system, and the

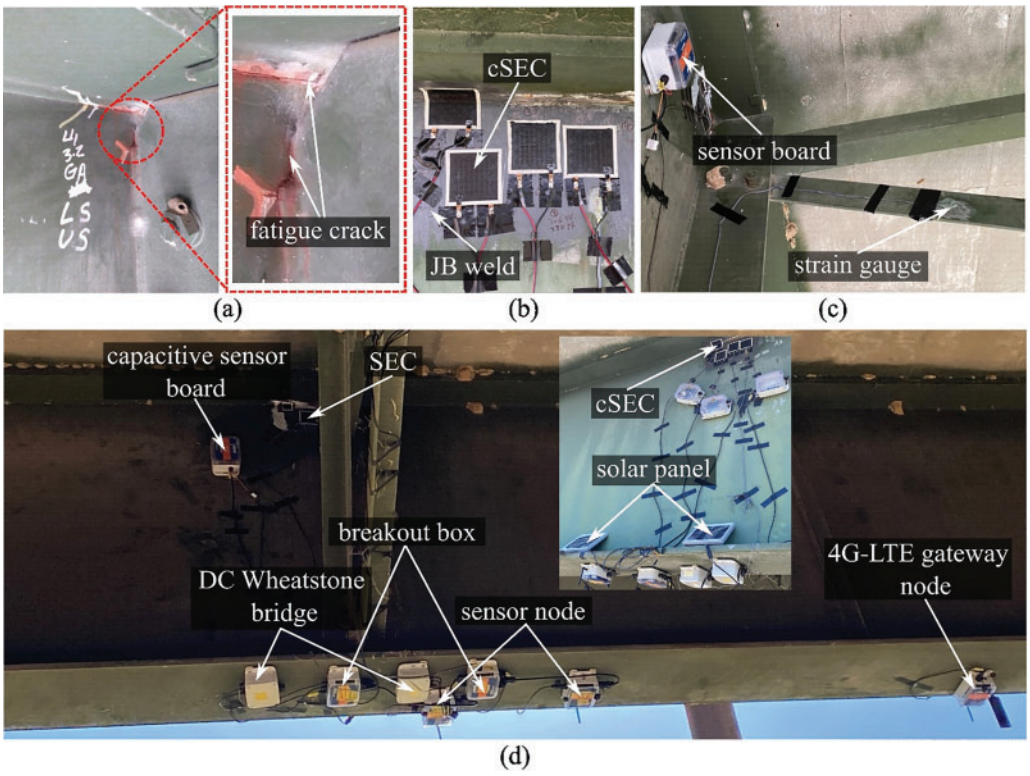

Figure 10. Installation of the sensor network: (a) fatigue crack location; (b) cSEC; (c) strain gauge location; and (d) overall wireless sensor network showing key hardware (adopted from Taher et al.[28] with the inset showing the facia side of the girder)

research team plans to conduct an ultrasonic test in the near future to verify the length of the fatigue crack measured by a cSEC. Data collection is scheduled to continue throughout the upcoming years.

A large-scale, non-skewed bridge girder connection was tested in a laboratory environment to validate field sensing data.[38] The test reproduced distortion-induced fatigue cracks in a structural system similar to that of the bridge, with the difference being that the girder to cross-frame connection is a simplified subassembly of the entire bridge system without considering the effect of the bridge deck. As shown in Fig. 11a, the bridge girder was mounted upside-down to simulate the boundary conditions due to the deck. A cross-frame was connected to the girder through the connection plates, with a 90° skew angle between the cross-frame and girder. SECs were deployed at the bottom web-gap region to assess fatigue cracks, as shown in Fig. 11b, and foil-type strain gauges were installed on the top horizontal cross-frame member to indirectly capture load $F(t)$. An actuator was vertically installed at the far end of the cross-frame to apply fatigue load on the girder. This setup was designed

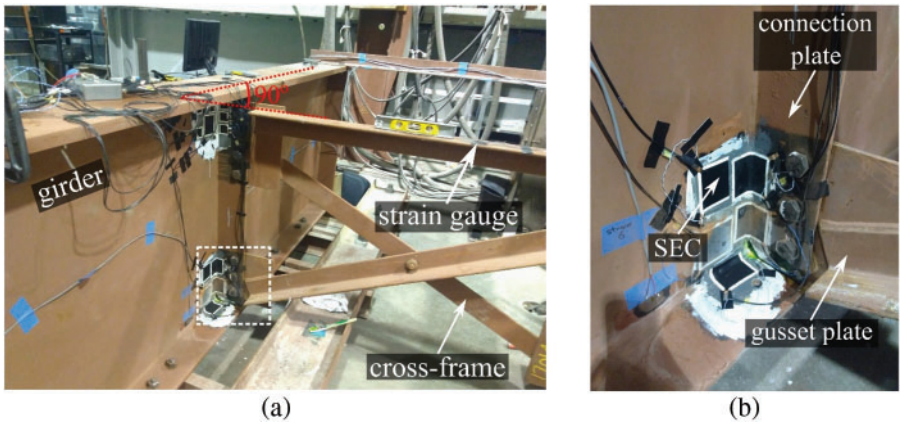

Figure 11. (a) Laboratory setup showing the non-skewed bridge girder and cross-frame connection; and (b) zoom on the installed SECs (adapted from Kong et al.[38])

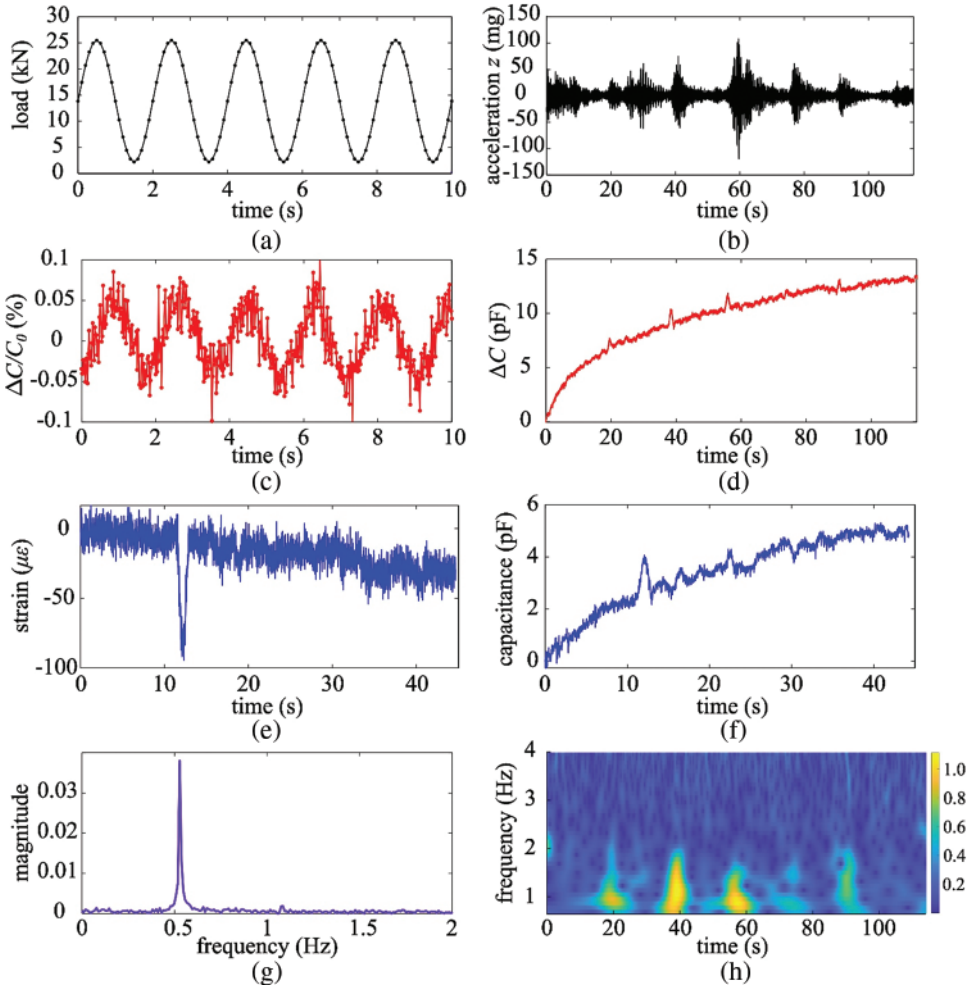

Figure 12. (a) Compression load applied on the laboratory non-skewed bridge girder connection; (b) acceleration measurements collected under multiple impulse traffic events; (c) time series plots of relative change in capacitance $\Delta C(t)/C_0$ measured from the laboratory non-skewed bridge girder; (d) time series plot of change in capacitance $\Delta C(t)$ measured from field bridge girder; (e) strain measurements collected by the strain gauge; (f) strain measurement collected by the SEC; (g) frequency spectrum of the SEC applied on laboratory bridge girder; and (h) CWT spectrogram plot of the magnitude of capacitance $|W(t, s)|_{C_i}$ signal collected from the field bridge girder

to allow vertical movement only by preventing lateral movement and rotation of the girder web. A 0.5 Hz harmonic excitation with a constant load range of 2.2 to 25.5 kN (0.5 to 5.75 kip) was applied (Fig. 12a). This load is under a symmetric distribution (±2.62 kip) in order to consider the reversal behavior of the traffic load in the field. SECs were removed after a total of 18,900 fatigue cycles to inspect the newly initiated fatigue crack beneath the sensor. Laboratory results, presented in Kong et al.,[40] used the original CGI, and demonstrated a linear relationship between the CGI and the number of actuation cycles once the fatigue crack was initiated, as shown in Fig. 13.

Results and Discussion

Fig. 12 presents key differences between laboratory-acquired data (left) and field-acquired data (right). In the field, the signal is that of an SEC installed at the bottom web-gap region of the laboratory bridge girder and located in front of the crack propagation path. The capacitance signal acquired in the laboratory environment (Fig. 12c) was typically acquired from a harmonic loading (Fig. 12a). In comparison, the capacitance data (Fig. 12d) acquired from field events (Fig. 12b) contains impulsive traffic events, is noisy, and exhibits a nonlinear DC component that may be attributable to a thermal effect when loading the sensor.

Figs. 12e and 12f show an example of the raw data measured by the strain gauge installed on the cross frame and the SEC installed in the web-gap region during a large impulsive event caused by traffic loading. A good match of the signal peaks is visible between 11 and 13 s, which also corresponds to the peak acceleration measured by the accelerometer. Figs. 12g and 12h compare Fourier and Wavelet transforms from the laboratory and field signals, respectively, illustrating the differences in signal complexity. The field signal is the result of multiple vehicular loading events, at 20, 40, 58, and 91 seconds. Fig. 12e shows a fundamental frequency peak at 0.5 Hz that can clearly be observed, consistent with

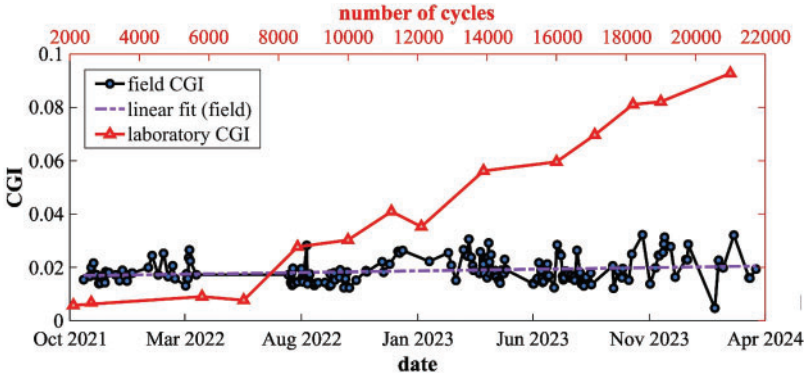

Figure 13. Comparison of averaged field CGI with the laboratory CGI

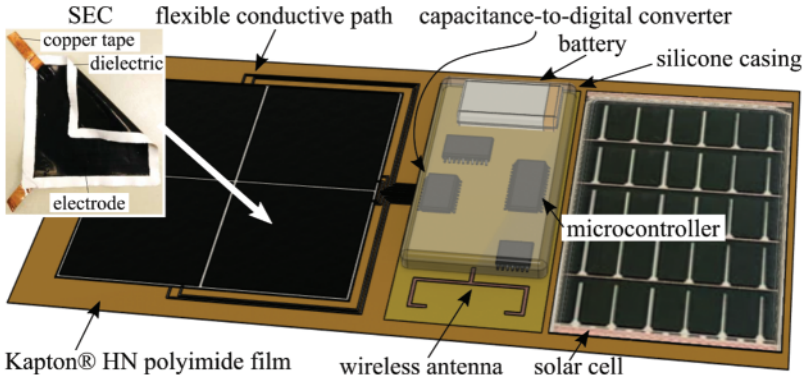

Figure 14. Visualization of an SEC-based, fully integrated sensing skin constructed as a printed hybrid flexible electronic device that will enable the fast and efficient deployment of the sensor for the monitoring of civil infrastructure

the input loading frequency. For the field data, the capacitance time series was filtered using detrending, high-pass filtering, and low-pass filtering to remove the low-frequency drift and high-frequency noise in the data, respectively. The cutoff frequencies of the high-pass and low-pass filters were 0.05 Hz and 4 Hz, respectively. The resulting CWT plots (Fig. 12f) exhibit concentrated signal energy in both time and frequency during traffic events, obtained by using the modified CGI algorithm illustrated in Fig. 6.

The modified CGI was extracted in the field from mid-October 2021 to mid-March 2024. A total of 168 datasets containing 1035 impulse events were collected and processed. These CGIs are plotted in Fig. 13. The presented field CGI are mean values averaged over one to two days using a minimum of two events. It can be observed that the linear fit of the field CGI has a positive slope, indicating the CGI slightly increased and that the fatigue crack propagated further during the monitoring period. Some fluctuations may be attributed to seasonal effects, whereas the magnitude of the crack opening with traffic is expected to vary with the bridge's temperature. This investigation is left to future work. Fig. 13 also compared field CGI values against those obtained from laboratory tests (using a Fourier transform) reported in Kong et al.,[38] where an array of SECs was used to cover a full-scale bridge girder to cross-frame welded connection to construct a CGI mapping the progression of a fatigue crack. The laboratory CGI increases starting at approximately 7000 cycles when the crack began initiating and then increases linearly with the number of cycles, correlating with crack length. It follows that the field CGI corresponds to an early crack size, as expected.

Recommendations for Future Work

Preliminary results obtained from the field deployment presented in this paper have demonstrated the successful transition of the SEC technology from the laboratory to the field environment, constituting a major step towards widespread deployment. The next major gap will be that of commercialization, where the technology will require another round of major updates to allow for a cost-effective and easy installation. The vision is a flexible and stretchable product that can be easily adhered to critical surfaces. To do so, improved fabrication techniques are needed to facilitate the integration of micro- and nano-particles in the polymer matrix, produce large sheets, and perhaps even update the polymer mix itself to eliminate the need for any solvent. This can be possible, for example, through the adoption of roll-to-roll manufacturing and the use of silicones. Also, the produced sheets of cSECs will require the integration of hardware and the minimization of hard wires. This includes the integration of flexible interconnects, and the development of strategies to join flexible, stretchable, and hard substrates.

The authors propose a possible path to bridging this gap to commercialization through the development of a fully integrated sensing skin.[45–47] The vision for such a sensing skin is shown in Fig. 14. It consists of SECs either attached or fabricated from a base film onto which the required electronics for data acquisition, processing, and transmission are also adhered. This self-contained printed hybrid flexible electronic sensor would form the backbone of a decentralized network of crack-monitoring flexible sensors. Printed hybrid flexible electronics are a type of printed flexible electronic that include semiconductor devices to expand the capabilities of printed flexible electronics beyond just conductive traces.[48] Aspects of these flexible electronics would be produced through additive manufacturing, reducing assembly cost and allowing for the rapid manufacturing of custom sensor arrangements based on a specific monitoring need.

Conclusion

This paper reported technological updates that were required to enable the field deployment of a sensing skin, termed soft elastomeric capacitor (SEC), developed for fatigue crack discovery and monitoring. Technological updates included: 1) corrugation of the surface of the dielectric, creating a corrugated SEC or cSEC, to improve sensing performance; 2) development of a dedicated wireless data acquisition system; and 3) improvement of the data fusion algorithm to account for the nature of traffic loading and higher signal contamination in the field.

In particular, it was found that the cSEC offered improved sensing properties compared to the original SEC through a higher signal-to-noise ratio and better linearity and sensitivity to strain. This was attributable to the corrugation adding lateral stiffness. The dedicated data acquisition system included a data readout circuit paired with an Xnode for wireless transmission. The data fusion algorithm, termed crack growth index (CGI), was modified by using a continuous wavelet transform instead of a Fourier transform to detect and isolate vehicular events and improve robustness with respect to noise.

Challenges in field deployment were also presented. Importantly, a method had to be developed to assess field performance. A large-scale laboratory setup was constructed to mimic field deployment, and laboratory-acquired CGIs were compared against those obtained in the field. The comparison of results showed good agreement and thus demonstrated the success of the field deployment. Lastly, a path to commercialization was discussed. Namely, the technology will require another round of important updates to enable the production of large sensing sheets with integrated flexible electronics.

Acknowledegments

The authors gratefully acknowledge the financial support of the Departments of Transportation of Iowa, Kansas, South Carolina, and North Carolina through the Transportation Pooled Fund Study TPF-5(449).

Data Availability Statement

The data that support the findings of this study are available from the corresponding author upon reasonable request.

Disclaimer

The statements, opinions, and data contained in all publications are solely those of the individual author(s) and contributor(s) and not of the editor(s).

Supplemental Materials

This paper does not include any supplemental materials. The information and findings presented in the main text constitute the entirety of the content related to the research study.

References

[1] Campbell FC. *Fatigue and Fracture Understanding the Basics*. Materials Park, OH: ASM International; 2012.
[2] Biezma MV, Schanack F. Collapse of steel bridges. *J Perform Constr Facil*. Oct 2007;21(5):398–405.
[3] Haghani R, Al-Emrani M, Heshmati M. Fatigue-prone details in steel bridges. *Buildings*. Nov 2012;2(4):456–476.
[4] Dorafshan S, Campbell LE, Maguire M, et al. Benchmarking unmanned aerial systems- assisted inspection of steel bridges for fatigue cracks. *Transp Res Rec: J Transp Res Board*. Mar 2021;2675:154–166.
[5] Campbell LE, Connor RJ, Whitehead JM, et al. Benchmark for evaluating performance in visual inspection of fatigue cracking in steel bridges. *J Bridge Eng*. Jan 2020;25(1).
[6] Zolfaghari A, Zolfaghari A, Kolahan F. Reliability and sensitivity of magnetic particle non- destructive testing in detecting the surface cracks of welded components. *Nondestruct Test Eval*. Jan 2018;33(3):290–300.
[7] Jeon I, Lim HJ, Liu P, et al. Fatigue crack detection in rotating steel shafts using noncontact ultrasonic modulation measurements. *Eng Struct*. Oct 2019;196:109293.
[8] Sampath S, Sohn H. Detection and localization of fatigue crack using nonlinear ultrasonic three-wave mixing technique. *Int J Fatig*. Feb 2022;155:106582.
[9] Kong X, Li J. Vision-based fatigue crack detection of steel structures using video feature tracking. *Comput-Aided Civil Infrastruct Eng*. Feb 2018;33:783–799.
[10] Dellenbaugh L, Kong X, Al-Salih H, et al. Development of a distortion-induced fatigue crack characterization methodology using digital image correlation. *J Bridge Eng*. Sep 2020;25(9).
[11] Mojidra R, Li J, Mohammadkhorasani A, et al. Vision-based fatigue crack detection using global motion compensation and video feature tracking. *Earthq Eng Eng Vibr*. Jan 2023;22:19–39.
[12] Qian W, Wu S, Wu Z, et al. In situ x-ray imaging of fatigue crack growth from multiple defects in additively manufactured AlSi10mg alloy. *Int J Fatig*. Feb 2022;155:106616.

[13] Lynch JP, Farrar CR, Michaels JE. Structural health monitoring: technological advances to practical implementations [scanning the issue]. *Proc IEEE*. Aug 2016;104(8):1508–1512.
[14] Sony S, Laventure S, Sadhu A. A literature review of next-generation smart sensing technology in structural health monitoring. *Struct Control Health Monit*. Jan 2019;26(3):e2321.
[15] Kharroub S, Laflamme S, Song C, et al. Smart sensing skin for detection and localization of fatigue cracks. *Smart Mater Struct*. May 2015;24(6):065004.
[16] Yan Y, Shen Y, Cui X, et al. Localization of multiple leak sources using acoustic emission sensors based on MUSIC algorithm and wavelet packet analysis. *IEEE Sens J.*. Dec 2018;18(23):9812–9820.
[17] Ai L, Zhang B, Ziehl P. A transfer learning approach for acoustic emission zonal localization on steel plate-like structure using numerical simulation and unsupervised domain adaptation. *Mech Syst Signal Process*. Jun 2023;192(9):110216.
[18] Wang Y, Qiu L, Luo Y, et al. A stretchable and large-scale guided wave sensor network for aircraft smart skin of structural health monitoring. *Struct Health Monitor*. Jun 2019;20(3):861–876.
[19] Yan J, Downey A, Cancelli A, et al. Concrete crack detection and monitoring using a capacitive dense sensor array. *Sensors*. Apr 2019;19(8):1843.
[20] Gresil M, Yu L, Shen Y, et al. Predictive model of fatigue crack detection in thick bridge steel structures with piezoelectric wafer active sensors. *Smart Struct Syst*. 2013;12(2):97–119.
[21] Ahmed S, Schumacher T, Thostenson ET, et al. Performance evaluation of a carbon nanotube sensor for fatigue crack monitoring of metal structures. *Sensors*. Aug 2020;20:4383.
[22] Yao Y, Glisic B. Detection of steel fatigue cracks with strain sensing sheets based on large area electronics. *Sensors*. Apr 2015;15(4):8088–8108.
[23] Liao Y, Zhou P, Pan D, et al. An ultra-thin printable nanocomposite sensor network for structural health monitoring. *Struct Health Monit*. Jul 2019;20:894–903.
[24] Wang Y, Hu S, Xiong T, et al. Recent progress in aircraft smart skin for structural health monitoring. *Struct Health Monit*. Dec 2021;21:2453–2480.
[25] Liu H, Yan J, Kollosche M, et al. Surface textures for stretchable capacitive strain sensors. *Smart Mater Struct*. Sep 2020;29:105037.
[26] Liu H, Laflamme S, Li J, et al. Investigation of surface textured sensing skin for fatigue crack localization and quantification. *Smart Mater Struct*. Sep 2021;30:105030.
[27] Liu H, Laflamme S, Li J, et al. Investigation of textured sensing skin for monitoring fatigue cracks on fillet welds. *Meas Sci Technol*. May 2022;33:084001.
[28] Taher SA, Li J, Jeong J-H, et al. Structural health monitoring of fatigue cracks for steel bridges with wireless large-area strain sensors. *Sensors*. Jul 2022;22(14):5076.
[29] Laflamme S, Saleem HS, Vasan BK, et al. Soft elastomeric capacitor network for strain sensing over large surfaces. *IEEE/ASME Trans Mechatron*. Dec 2013;18:1647–1654.
[30] Downey A, Pisello AL, Fortunati E, et al. Durability and weatherability of a styrene-ethylene-butylene-styrene (SEBS) block copolymer-based sensing skin for civil infrastructure applications. *Sens Actuators A: Phys*. Jul 2019;293:269–280.
[31] Spencer B, Park J-W, Mechitov K, et al. Next generation wireless smart sensors toward sustainable civil infrastructure. *Proc Eng*. 2017;171:5–13.
[32] Jeong J-H, Xu J, Jo H, et al. Development of wireless sensor node hardware for large-area capacitive strain monitoring. *Smart Mater Struct*. Nov 2018;28:015002.
[33] Jeong J-H, Jo H, Laflamme S, et al. Automatic control of AC bridge-based capacitive strain sensor interface for wireless structural health monitoring. *Measurement*. Oct 2022;202:111789.
[34] Oliva PV, Wu Y, He C, et al. Towards fast weak adversarial training to solve high dimensional parabolic partial differential equations using XNODE-WAN. *J Comput Phys*. Aug 2022;463:111233.
[35] Hoang T, Fu Y, Mechitov K, et al. Autonomous end-to-end wireless monitoring system for railroad bridges. *Adv Bridge Eng*. Dec 2020;1(17).
[36] Fu Y, Hoang T, Mechitov K, et al. Sudden event monitoring of civil infrastructure using demand-based wireless smart sensors. *Sensors*. Dec 2018;18:4480.
[37] Fu Y, Mechitov K, Hoang T, et al. Development and full-scale validation of high-fidelity data acquisition on a next-generation wireless smart sensor platform. *Adv Struct Eng*. Aug 2019;22:3512–3533.
[38] Kong X, Li J, Collins W, et al. A large-area strain sensing technology for monitoring fatigue cracks in steel bridges. *Smart Mater Struct*. Jul 2017;26:085024.
[39] Kong X, Li J, Collins W, et al. Sensing distortion-induced fatigue cracks in steel bridges with capacitive skin sensor arrays. *Smart Mater Struct*. Oct 2018;27:115008.
[40] Kong X, Li J, Bennett C, et al. Thin-film sensor for fatigue crack sensing and monitoring in steel bridges under varying crack propagation rates and random traffic loads. *J Aerospace Eng*. Jan 2019;32(1).
[41] Cai L, Song L, Luan P, et al. Super-stretchable, transparent carbon nanotube-based capacitive strain sensors for human motion detection. *Sci Rep*. Oct 2013;3(3028).
[42] Pasadas F, Jimenez D. Large-signal model of graphene field-effect transistors—part i: compact modeling of GFET intrinsic capacitances. *IEEE Trans Electron Dev*. Jul 2016;63(7):2936–2941.
[43] Lilly J, Olhede S. Higher-order properties of analytic wavelets. *IEEE Trans Signal Process*. Jan 2009;57(1):146–160.
[44] Aguiar-Conraria L, Soares MJ. The continuous wavelet transform: moving be-yond Uni- and bivariate analysis. *J Econ Surv*. Feb 2013;28:344–375.
[45] Aygun LE, Kumar V, Weaver C, et al. Large-area resistive strain sensing sheet for structural health monitoring. *Sensors*. Mar 2020;20:1386.
[46] Smith C, Downey AR. Additively manufactured flexible hybrid electronic sensor for discrete fatigue crack detection. In: *AIAA SCITECH 2023 Forum*. National Harbor, MD: American Institute of Aeronautics and Astronautics; Jan 2023.
[47] Qiu L, Lin X, Wang Y, et al. A mechatronic smart skin of flight vehicle struc- tures for impact monitoring of light weight and low-power consumption. *Mech Syst Signal Process*. Oct 2020;144:106829.
[48] NextFlex. About flexible hybrid electronics: defining flexible hybrid electronics (FHE). 2022. https://www.nextflex.us/about/about-fhe/

BER the international journal of bridge engineering management and research

Seismic Fragility and Risk Assessment of Reinforced Concrete Bridges Undergoing Elastomeric Bearing Deformations Induced by Landslide

Sergio Ruggieri[1]; Andrea Nettis[1]; Domenico Raffaele[1]; Biagio Guido[2]; and Giuseppina Uva[1,*]

Submitted: 09 January 2024 **Accepted:** 09 July 2024 **Publication date:** 03 September 2024

DOI: 10.70465/ber.v1i1.6

Abstract: The paper presents a study on the seismic fragility of Reinforced Concrete (RC) bridges isolated by elastomeric bearing devices subjected to differential displacements induced by slow-moving landslides. The seismic behavior of isolated bridges is ruled by the performance of elastomeric bearings to reduce and dissipate earthquake actions. These bridges are subjected to service loads that usually are accounted for in the design, but possible additional actions from the surrounding environment, such as landslides affecting substructure components, can seriously undermine the seismic response. The paper describes a practical approach to investigate the seismic fragility and risk of RC bridges isolated by elastomeric bearings, which may undergo early deformations induced by the differential displacements of substructure components. Based on previous existing studies, the proposed methodology is based on numerical modeling accounting for landslide-induced substructure displacements and proper modifications on the constitutive law and hysteretic response of the elastomeric bearings. Subsequently, after establishing specific limit-states, nonlinear time history analyses of the seismic response are used to estimate fragility curves and risk indicators. The study points out that it is possible to quantify the influence of landslide-induced effects on seismic fragility and risk by using only two numerical models in order to provide decision support to transportation authorities responsible for ensuring the safety of bridges and road networks. The proposed approach has been tested on a real-life case study, the *Santo Stefano* Viaduct in Italy, which was subjected in the past to relevant deformations of the elastomeric bearings due to an active landslide phenomenon.

Author keywords: Seismic fragility; existing RC bridges; elastomeric bearings; landslides, multi-hazard risk

Introduction

The study of the vulnerability of existing Reinforced Concrete (RC) bridges under natural and human-related hazards is one of the main challenges that the scientific community, public institutions, and road management companies are currently facing in light of recent tragic events that have been reported structural collapses and intangible financial and human losses, as well as the occurrence of extended downtime. For bridges and viaducts, the causes of collapse may be related to a combination of different hazardous sources, which should be considered together to correctly assess the structural health condition and prioritize retrofit interventions. Within this framework, several studies have been proposed in recent years by the scientific literature, with the aim of investigating multi-hazard risk sources affecting existing bridges (e.g., Gidaris et al.[1]). Seismic risk prioritization is one of the most studied topics in seismic hazard-prone areas. Starting from a view of the entire bridge stock in Italy, Borzi et al.[2] proposed an automatic tool to estimate the seismic fragility of bridges at two limit states (i.e., damage and collapse). The tool was tested on a sample of around 500 existing bridges for which good level information was available, and a WebGIS graphical user interface was released to observe real-time damage scenarios. Abarca et al.[3] investigated seismic risk and losses of more than 600 existing bridges in Southern Italy, creating a proper taxonomy on the basis of full complete structural information given by another bridge dataset and statistically investigating the seismic response of simulated archetypes. Obviously, large-scale studies based on typological approaches are possible when enough information is available. For portfolio-scale bridge assessment, single-structure simplified approaches can be mentioned, where the seismic fragility can be estimated through displacement-based assessment techniques characterized by different bridge typologies[4,5,6].

Current research trends are increasingly focusing on the vulnerability of bridges under geohazards and flood

*Corresponding Author: Giuseppina Uva.
Email: giuseppina.uva@poliba.it
[1]DICATECH Department, Polytechnic University of Bari, Via Orabona 4, 70125, Bari, Italy
[2]ALEANDRI S.p.a, Corso Vittorio Emanuele II 52, 70122, Bari, Italy

Discussion period open till six months from the publication date. Please submit separate discussion for each individual paper. This paper is a part of the Vol. 1 of the International Journal of Bridge Engineering, Management and Research (© BER), ISSN 3065-0569.

actions. Regarding geohazards, damages can be induced by differential settlements of the bridges related to soft soil strata (not properly considered in the design) or by low-moving ground movements affecting bridge foundations, typical of areas affected by active landslides. In these cases, for an appropriate risk assessment, monitoring campaigns should be provided, by employing specific instruments and long-time observations. Nevertheless, an important resource exploited in the last years is represented by multi-temporal satellite-based differential interferometry (MTInSAR) techniques, which allow to detect displacements of the terrestrial surface over a long range of time and assess the possible interference with existing bridges (or more in general with structures). Peduto et al.[7] proposed a framework based on MTInSAR data and on-site surveys to probabilistically assess the structural condition of existing bridges in Amsterdam and proposed fragility functions to describe current ground motion-induced damage conditions. Nettis et al.[8] developed an automated tool that elaborates the displacement histories of persistent scatters on bridges belonging to road networks and identifies the units subjected to geological motions so that interventions can be prioritized. The tool was also implemented in a GIS environment, in which the worst elements of the investigated road network, requiring on-field refined inspections, are visualized in real-time with a colored scale. With regard to flood actions, the action of river water can apply hydrostatic and hydrodynamic forces to the structural elements of bridges, implying an overloading effect. Nevertheless, the real danger is represented by the combination of the flood (and the velocity of the water) affecting a bridge and the debris (e.g., log) that the flowing water can drag along, colliding with the structural elements. In addition, flowing water could also scour a portion of the soil, characterizing the bridge foundation and reducing the lateral capacity of piles and, therefore, of the entire structure. Anisha et al.[9] proposed a methodology to estimate flood-induced risk for different limit states, providing flood fragility curves. Pregnolato et al.[10] developed a multi-physics modeling approach for assessing the influence of hydrodynamic actions on bridges and the consequent structural response and impact on the road network.

Several studies also aim to combine the above-mentioned risk sources by providing approaches that can be used for improving the study of the structural capacity of existing bridges. For example, Yilmaz et al.[11] investigated the combination of flood and seismic hazards for investigating an existing bridge in California. Similarly, Gehl & D'Ayala[12] developed a multi-hazard risk assessment procedure based on Bayesian network models to account for flood and seismic actions on bridge networks. Mantakas et al.[13] analyzed the seismic response of a case-study bridge in Greece, which was affected by ground movement induced by an active landslide. They performed numerical analyses considering the coupling effect of the seismic-induced motions on stabilization of the soil foundation and the structure, considering the variability of different foundation schemes and stabilization techniques.

Currently, public institutions and transportation managers are working towards the development of procedures for efficient multi-hazard risk assessment and the definition of mitigation strategies. Taking into consideration the Italian case, all the above risk sources are involved in the new risk-mitigation model developed by the Italian Ministry of Transportation[14], released after the well-known collapse of the Polcevera Viaduct[15]. The new Italian guidelines[14] propose a multi-level procedure to be applied to the entire existing bridge stock, which road management companies should adopt for the appropriate management of bridges based on monitoring, maintenance, and retrofit. In this framework, one of the most important phases is represented by the periodical bridge-specific on-site visual inspection, in which expert engineers check the health state of each structural element. This phase covers a key role in the Italian risk-mitigation model, especially for those elements that were scarcely inspected in the past, such as the bearing devices. These latter assume paramount importance in the safety and serviceability of the structure, both from the static (gravity load transfer to substructure) and seismic (transfer of seismic inertia forces to substructure or isolation/dissipation) points of view.

Appropriate schemes of bearing devices, consisting of high-damping elastomeric bearings eventually equipped with lead plugs, can guarantee seismic isolation and dissipation[16]. The seismic response of isolated bridges is characterized by a large vibration period, given by the flexibility of isolators, inducing relevant displacement demand, which is appropriately mitigated by increasing damping provided by the isolation devices. In these structures, the displacement demand is lumped to the isolation systems that are subjected to relevant deformations during the seismic-induced ground motion and can achieve significant deformation-based damage states. Differential displacements of the substructure components subjected to low-moving ground motions induced by active landslides can cause deformation in elastomeric bearings, affecting their capacity during seismic events and increasing the fragility of the bridge.

On this basis, the paper presents a study on the seismic behavior of existing isolated reinforced concrete (RC) bridges subjected to preliminary landslide-induced elastomeric bearing deformation. In particular, a framework is introduced to estimate the influence of landslide-induced bearing deformations on seismic fragility and risk considering several deformation-based damage states. The framework is based on nonlinear time history analyses performed by using scaled natural ground motions and numerical models in which the cyclic behavior of preliminary deformed elastomeric bearings is simulated based on experimental tests available from the scientific literature. The proposed approach was tested on a real-case study, the Santo Stefano viaduct in the Basilicata region (Southern Italy), which was subjected in the past to the abovementioned phenomenon. For the case study, seismic fragility curves were provided, considering and not the observed landslide-induced deformations in elastomeric bearings.

Related Studies

Seismic isolation in RC bridges: the use of elastomeric bearings

When talking about RC bridges, the isolation system is placed on substructure components and acts as a flexible layer, uncoupling the superstructure from the substructure[17]. The low stiffness of isolation devices induces large values during the vibration period, inducing significant displacement demand under seismic excitation, which is lumped in the isolation layer. In the case of strong seismic actions, the nonlinear response (and hysteretic dissipation) is lumped into the isolation bearings, while the other components (superstructure and substructure) behave elastically. In general, two types of isolation systems can be employed in RC bridges: (1) elastomeric bearings; and (2) sliding bearings[18]. The elastomeric bearings allow the shift of the fundamental frequencies of the structure through a specifically designed horizontal stiffness for the purpose of resonance averting. Instead, the sliding bearings works according to the concept of dissipation through friction, thanks to specific frictional devices that allow seismic isolation. For the purpose of this study, the focus of this section is related to the elastomeric bearings and the seismic behavior of isolated RC bridges equipped by these devices.

The most adopted elastomeric bearings in the practice are the laminated rubber bearings, which are characterized by alternate thin layers of rubber and steel. Low-damping natural rubber bearings (NRB) or high-damping rubber bearings (HDRB) can be used for isolation purposes. Additionally, lead-rubber bearings are characterized by the presence of a central lead core that increases the dissipation capacity. The scientific literature provided several studies over the last 50 years regarding the seismic behavior of bridges with elastomeric bearings, the design of these devices, and the assessment through experimental and numerical analyses. For the purposes of this study, a brief summary of the seismic fragility of isolated bridges is reported. Gardoni & Trejo[19] proposed some probabilistic models to investigate the seismic demand in isolated RC bridges, with the aim of providing a reliability-based approach to bridge design. With this goal in mind, the authors generated a sample of RC NRB-isolated bridges, which were analyzed through sets of ground motion records to derive fragility curves via an approximate formulation. Siqueira et al.[20] investigated the seismic behavior and fragility of isolated RC bridges in Canada retrofitted via NRB. The authors considered the uncertainties related to the mechanical properties of NRBs based on experimental tests in which size and shape factors varied. Dezfuli & Alam[16] investigated the influence of different elastomeric bearing typologies on the seismic fragility of isolated RC bridges. Using NRBs, HRBs, and LRBs on a three-span continuous bridge, the authors assessed the most vulnerable typology despite highlighting the pros of the isolation. Bayat et al.[21] investigated the seismic fragility of skewed RC isolated bridges, accounting for more than 10 types of elastomeric devices, with the aim to define the sub-optimal combination for improving the design of the isolation system. Hassan and Billah[22] investigated the effect of ground motion duration on the seismic response of isolated bridges, equipped with three different types of isolation bearings (among which, LRB). Results suggest that long-duration and high-intensity earthquakes significantly affect the performance of bridges and the isolation system efficiency. Maghsoudi-Barmi et al.[23] investigated the seismic performance of highway isolated bridges equipped with unbonded NRBs. Despite the evident advantages of this system (e.g., easiness and cost of production), properties like bearing connection type, friction coefficient, and aging were considered in the analyses showing possible implications in terms of fragility. Kurino et al.[24] analyzed the seismic fragility of isolated highway bridges, accounting for the rubber deterioration. Results in terms of fragility curves provided an evident lower performance of the isolated bridge when deterioration is accounted, and the necessity of a retrofit solution based on cable restrainers. Wei et al.[17] proposed a study on the seismic fragility of isolated bridges accounting for two aspects: (a) the pier height; (b) the behavior of elastomeric bearings. Firstly, authors performed and experimental campaign comprising different kinds of elastomeric bearings combined with different height piers. From the estimate of the seismic fragility, authors proposed an optimal combination of the above parameters, in a view of new designs. Aghaeidoost and Billah[25] performed a sensitivity analysis on bridge fragility using different modeling approaches for considering the LRBs in isolated RC bridges. Results revealed that hardening effect of elastomer and strength degradation due to the lead core heating assumes a key role.

Influence of preliminary deformation of elastomeric bearings in RC bridges

The seismic behavior of isolated RC bridges is strongly correlated to the performance of bearings devices, which connect substructure with the superstructure. In the case of elastomeric bearings, the design and the assessment of the devices consist in the consideration of axial forces to which they are subjected under gravity loads and the allowable horizontal displacements that they can achieve in the case of seismic excitation. According to the goal to purse through the isolation system, several experimental, analytical, and numerical studies were proposed in the past to investigate the capacity of elastomeric bearings and their behavior under vertical-horizontal actions (e.g., Kikuchi et al.[26], Vemuru et al.[27]). On the other hand, the most recent literature pointed out to consider other factors affecting the nonlinear behavior of elastomeric bearings. With this regard, Mitoulis[28] performed a parametric analysis accounting for uplift effect in elastomeric bearings when horizontal actions invest an isolated bridge. Results showed that a tensile displacement in bearings occurs if the pier is subjected to rotation and emphasized if bearings are placed eccentrically with respect to the pier axis. Very significant are the studies proposed by Moghadam and Konstantinidis[29,30] which investigated with axial loads and horizontal displacements also the top plate rotation of bearings. In the first work, authors proposed a detailed finite element model for elastomeric

bearings subjected to top plate rotation and compared the numerical performance with other literature works, while in the second work, authors provided a macro-model for the same purpose. The main results showed that rotation influences the critical shear force of the bearings instead of critical displacement. In addition, a larger vertical stress can provide a decrease of tangent stiffness. Still, Moghadam & Konstantinidis[31] carried out an experimental campaign in which authors investigated the role of plate rotation in LRB for different axial loads and horizontal displacement. The main result presents a shift up of the hysteresis loop, with a critical force reduction for negative actions (where the term "negative" indicates the opposite direction of the action, assuming a reference system). This problem was recently faced by different authors, which proposed some new mechanical models on the base of Moghadam and Konstantinidis achievements (e.g., Zhang et al.[32], Pishgahi & Taghikhany[33]).

Although several studies are provided for describing the real behavior of isolation systems in bridges under horizontal loads, very few studies face the occurrence of induced deformation in elastomeric bearings, induced for example by landslides. Hence this paper attempts to provide a practical approach for evaluating the variation in terms of seismic fragility of isolated bridges characterized by the above problem. Nevertheless, it is necessary to anticipate that authors do not dispose of any experimental campaigns to accurately evaluate the real performance of the bearings, but this would be a first step in this direction, considering slow and invisible phenomena like landslides can strongly limit the efficiency and the life of such structures.

Influence of Landslide-induced Bearing Deformation on the Seismic Response of Isolated Bridges: Proposal of a Practical Approach

The main aim of this study is to provide a practical methodology to characterize the influence on the seismic performance of bridges isolated by elastomeric bearings when these latter present pre-existing deformations induced by low-moving ground movement. The steps of the proposed procedure are described in the following subsections and briefly summarized in Fig. 1.

Basic knowledge of the bridge

The first step involves a comprehensive knowledge characterization of the bridge under investigation. Being an existing structure (even if built in the recent past), it is necessary to collect data on bridge's geometry and structural features by performing an accurate knowledge process according to the reference code (e.g., see Hendy et al.[34] for Eurocode). The most important aspects to be characterized concern the geometry (e.g., dimensions of each structural element), gravity loads to be considered for seismic analysis and, particularly, information on the nonlinear cyclic response of isolation devices. Considering that the bridge nonlinear response is governed by the isolation system, the mechanical properties of structural materials are of minor importance since superstructure and substructure components are modeled as elastic components (see sub-Section 3.3). A key information is represented from the original technical documents on elastomeric bearings which are needed to numerically reproduce their response under gravity and seismic loads. Given a sufficient documentation, this step is aimed to determine a numerical (e.g., finite element, FE) model of the investigated bridge without any interference from the surrounding environment. This numerical model (named Model 1—Undeformed) represents the reference one.

Survey and monitoring of landslide-induced deformative phenomena

The second step of the procedure regards the survey and monitoring of the bridge subjected to deformative phenomena. This phase can be performed through several operations, which depend on the available time and economic sources dedicated to the phenomenon identification (this latter can depend also on the importance of the structure within the road network). The operations are subdivided in two categories: (a) short-term survey; (b) long-term monitoring. Regarding to the short-term survey, when the deformation on the structures occurs, expert engineers are involved to carry out an accurate survey of each structural element. Simple methodologies can be employed, such as a full-photographic survey or a plumb line method to detect horizontal deformations of elastomeric bearings. These simple measures allow us to understand at what point the phenomenon is and, above all, what is the current difference with the undeformed configuration, according to the original documentation. In addition, the short-term survey allows establishing the strategy to employ for the long-term monitoring. About the long-term monitoring, several experimental campaigns can be employed, depending on the type of manifested phenomenon. The expression long-term refers to the necessity of carrying out experimental campaigns for a long period, depending on the efficiency of the monitoring system and on the intensity/velocity of the monitored phenomenon. To generalize this step in a view of a landslide action, three types of monitoring campaigns are strongly suggested: (i) a topographic monitoring; (ii) a geotechnical monitoring; (iii) a structural monitoring. The topographic monitoring is useful to accurately define the position of the structural elements for a given acquisition and estimate the displacement trend by repeating acquisitions of the position over time. These measurements should detect displacements and deformations of the substructure components. The measurements can be performed by using the most recent survey techniques (e.g., drones with high-accuracy photogrammetry, laser scanner acquisitions) or by simply using a total station with some collimation points materialized on the structures with reflective devices (e.g., measuring prisms). The campaign should provide periodical measurements, considering a time step of a couple of

months, for ensuring appropriate understanding of seasonality effects on the deformation trends. The geotechnical monitoring is essential in problems related to geohazards, and then measurements of slow motions and the evolution of the underground water level are the minimum requirements. In this case, a static monitoring should be employed, by using inclinometers and piezometers. The monitoring time should be quantified as previously stated for the topographic monitoring. Finally, a structural monitoring is suggested, even if it should be the most expensive among the three above actions and it can provide information about the structural evolution in consequence to base deformations. Accurate monitoring systems (e.g., strain gauges) placed in the right position can suggest the displacement and the velocity of the structural elements motions. Also in this case, the time of the experimental campaign should follow the above suggestions. As output of this step, for purpose of structural and seismic assessments, the following data should be detected: (a) the displacements and the rotations at the base of the piers (and the abutments); the horizontal deformation of the elastomeric bearings and the related rotation of the top steel plate.

Numerical simulations

Once all data are available, two numerical models can be realized, accounting and not for the landslide-induced deformative phenomenon (Model 1-Undeformed and Model 2-Deformed as reported in Fig. 1). For both models, considering the goal to estimate seismic behavior and fragility, simple numerical models can be employed, depending on the analysts' preferences. The modeling strategy is shown in Fig. 2a, where the numerical model should appropriately consider the nonlinear cyclic response of elastomeric bearings, while substructure components and superstructure elastomeric bearings are considered elastic. Particularly, the superstructure can be schematized through a simple frame equipped with an appropriate inertia moments and mass distribution. Three-dimensional models are suggested for analysis in both longitudinal and transverse direction (separately or contemporarily). The elastomeric bearings are characterized by a backbone curve equipped with the proper hysteretic behavior. In the case of LBRs or HDRBs, the backbone is usually elasto-plastic with high hardening while the hysteretic behavior is like-isotropic. If significant, depending on the investigated bridge structural features, the nonlinear behavior of other components should be included in the model[35]. For example, pounding between adjacent decks (for simply supported girder schemes) and between deck and abutments should be modeled by simulating impacts between different elements after gap closure. Similarly, the impacts between superstructure and shear keys in case of large displacements should be represented. If needed, abutment-backfill and soil-structure interactions can be considered.

While the undeformed model does not include the landslide-induced effects, the deformed model should represent the seismic behavior of the bridge under landslide-induced deformed conditions. A schematic and qualitative representation of a landslide-induced displacement scenario resulting in deformation on elastomeric bearings is provided as shown in Fig. 3. In detail, the slow action of low-moving active landslide provokes a roto-translation of the substructure components (a pier is represented in Fig. 2, although the same effect can be recorded for abutments). Given their high flexibility, elastomeric bearings experience deformations since their lower plate is connected to the pier cap, while

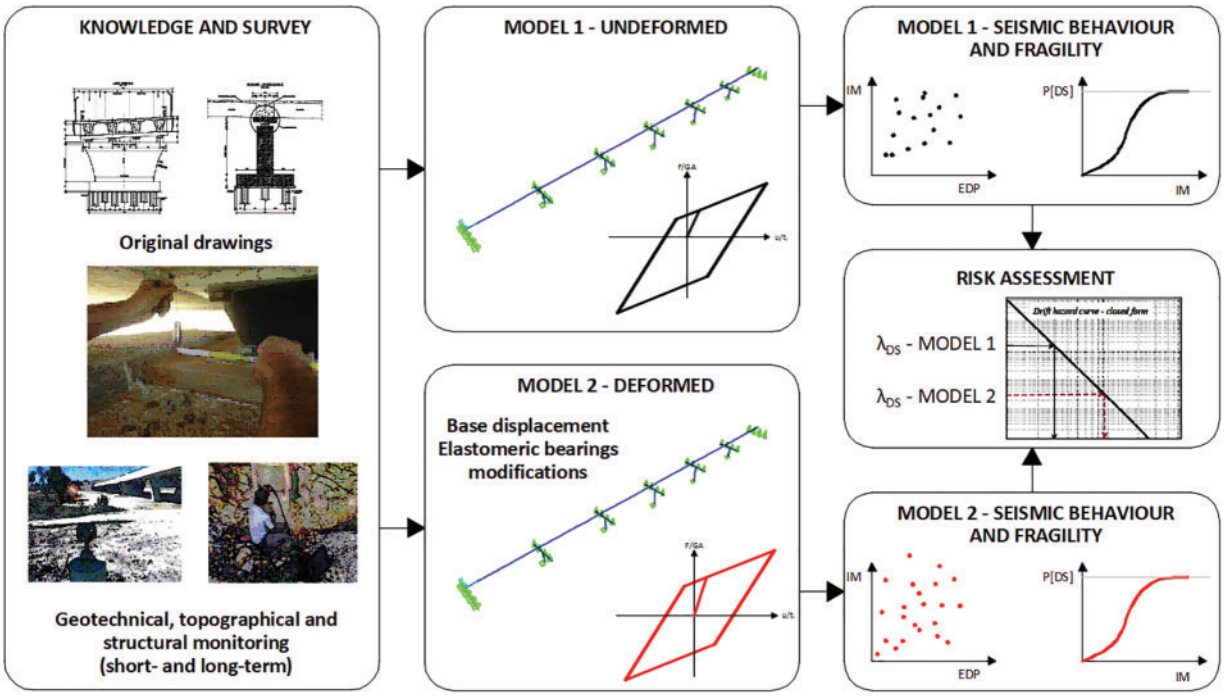

Figure 1. Summary of the proposed approach

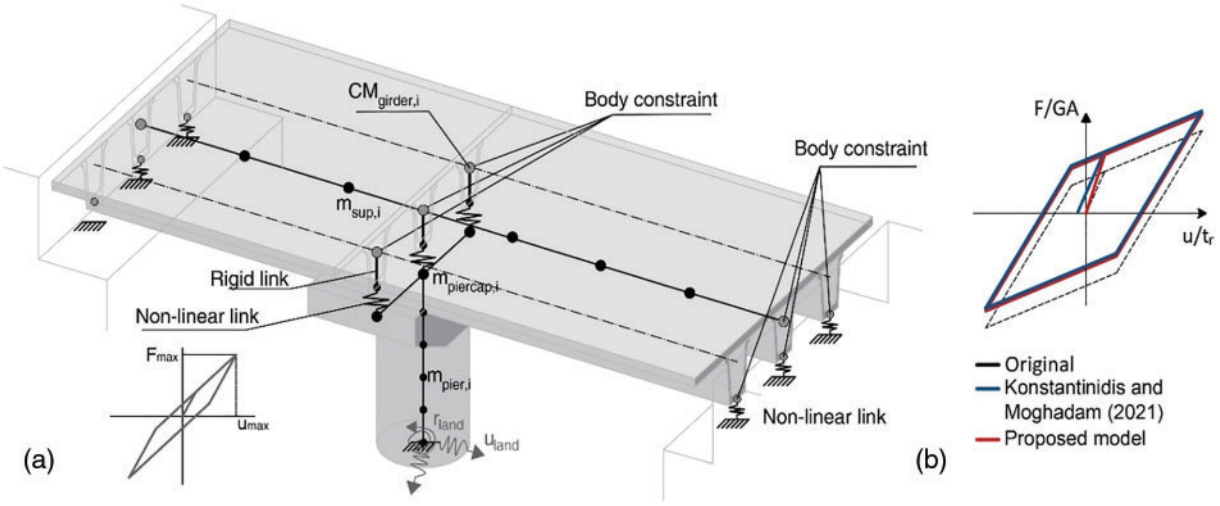

Figure 2. a) Strategy for numerical modeling; b) Proposed modification to elastomeric bearing constitutive law. F/GA represents the ratio between the horizontal force and the elastomer area and shear modulus. u/tr represents the ratio between the horizontal displacement and the rubber thickness

the upper plate is connected with the superstructure, which behave as an hyperstatic system, counteracting the displacement of the pier. Clearly, bearing deformations are enhanced in continuous-superstructure bridges, while these can be mitigated in simply supported (e.g., isostatic) bridges. The phenomenon can be simply described by a roto-translation of the pier and a different roto-translation of the elastomeric bearings (this latter depends on several factors, such as the transverse and torsional stiffness of the superstructure and their vertical stiffness, which in this study were not considered). To simulate the horizontal displacement, if the output of geotechnical monitoring is available, the model can account for soil-structure interaction and then, soil-structure interaction could be also modeled. On the other hand, if the monitoring is not complete and to benefit the modeling simplicity, it is suggested to simulate the base of the pier like fix and to apply a static displacement pattern with specific values detected in a precise moment, for both analysis directions.

As stated by Moghadam & Konstantinidis[31], preliminary bearing rotation involves modification in the nonlinear response of elastomeric bearings. Given the axial force calculated considering gravity loads, the rotation can be analytically computed after some in-situ measures of each elastomeric bearing. As shown in Fig. 3, right, at the base of the support there is a bottom rotation, θ_B, which is equal to the rotation of the pier if no deformation occurs (it is likely, considering that the landslide action is static, and the pier is subjected to a rigid roto-translation). If the surveyor detects the right and left height of the focused elastomeric bearing (H_1 and H_2 respectively), and the new base in the deformed configuration (L_1), the top rotation, θ_T, can be simply computed as

$$\theta_T = \frac{max\,(H_1, H_2) - min\,(H_1, H_2)}{L_1} \qquad (1)$$

The value of θ_T is relative to the rotated pier and then, it does not depend on the base rotation of the pier.

For sake of completeness, if θ_T should be computed in absolute value, it must be purified by the value of θ_B. Although the estimate is very simple, it provides a likely value of rotation which can be used to shift the elastomeric bearing backbone and the related hysteresis loop of a force computed according to Moghadam & Konstantinidis[31]. The response in terms of hysteresis loop is shown in Fig. 2b, in which the original constitutive law (dashed-black), the abovementioned literature solution (blue) and the simplified proposed ones are shown (red). In detail, in the proposed simplification, the value of the initial stiffness is slightly changed, considering that commercial software does not allow to define a backbone law that does not go through the origin of the axes. It is worth noting that the proposed modification for the backbone of the elastomeric bearings tends to modify only the elastic branch of the real constitutive law, by modifying its stiffness. This numerical trick brings to increase the bearings stiffness, allowing a conservative effect in the achievement of the yielding. Both simplified modeling techniques (displacements at the base of the pier and modified backbone of elastomeric bearings) allows to modify the model according to the observed effect.

Seismic analysis, fragility, and risk quantification

Once numerical models are ready, a probabilistic seismic analysis can be performed to estimate the possible differences on fragility and risk. For this purpose, nonlinear response history analyses (NRHAs) are strongly suggested in literature. For this scope, a record selection is required, which can be performed according to the specific hazard characteristics of the bridge site and the related soil amplification. The record selection should be performed based on the methodology adopted to carry out the probabilistic seismic assessment (e.g., cloud analysis). In this study, a cloud-based fragility analysis[36] by using natural scaled ground-motion records is performed. Regarding to the number of records, being a single-scale analysis, record-to-record

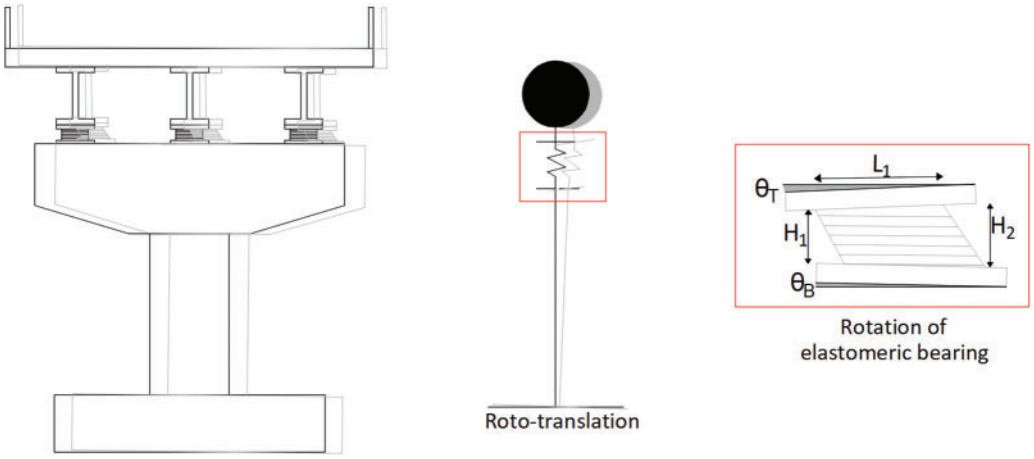

Figure 3. Schematization of landslide effect on a pier with isolation system made through elastomeric bearings

variability assumes high significance in the result and then, a high number of records should be desirable. On the other hand, a practical approach as the one proposed cannot require high computational efforts. Hence, the suggestion is to adopt at least 11 records, according to the suggestions provided in ASCE 7-16.[37]

The number of ground motion components depends on the observed displacement. If the displacement occurs in one direction (e.g., transversal), the main effects shall be observed in that direction and monodirectional analysis can be performed, but in general, bi-directional analysis can be employed. The intensity of the record is quantified in terms of and intensity measure, IM, which for the case at hand can be set in terms of peak ground acceleration, PGA, or spectral acceleration of the first vibration period, $Sa(T_1)$ (for more information, see O'Reilly[38]). After running analysis, the results can be recorded in terms of engineering demand parameter, EDP, which for the case of isolated RC bridge can be selected as the shear strain of elastomeric bearings (γ), according to Aghaeidoost & Billah[25]. Given the distribution of EDP|IM, fragility curves can be quantified, by referring to different damage states or different limit states. For the case at hand, the suggestion is to refer to the damage states (DS) as a percentage of γ values, according to Zhang & Huo[39]. It is worth specifying that for a row of elastomeric bearings on the same pier of pier cap, the DS can be considered exceeded when the first support exceeds the predefined limit. Eq. (2) shows the generic analytical form used in this study for a given fragility relationship, expressing the probability of violating, given a DS, $P(DS|IM)$. The fragility model is expressed by the normal cumulative distribution function, $\phi(\cdot)$, based on the probabilistic seismic demand model represented by a power-law model ($EDP = aIM^b$) which is fitted to the "cloud data" in the $\log IM - \log EDP$ plane. The parameters a and b are estimated through regression analysis resorting to the least square method. This logarithmic standard deviation (or dispersion, $\beta_{EDP|IM}$) is quantified via Eq. (3), where N is the number of ground motions gm.

$$P(DS|IM) = \phi\left(\frac{\ln EDP_{DS} - \ln aIM^b}{\beta_{EDP|IM}}\right) \tag{2}$$

$$\beta_{EDP|IM} = \sqrt{\frac{\sum_{gm=1}^{N}\left(\ln EDP_{gm} - \ln aIM_{gm}\right)^2}{N-2}} \tag{3}$$

Given the fragility curve for each DS and for both numerical models, risk can be quantified. The risk is quantified as the mean annual frequency of exceeding the damage state λ_{DS}. For this last step, the simplified formulation of the risk can be employed[40]:

$$\lambda_{DS} = \lambda_{IM,50}^{DS} e^{\left(\frac{1}{2}k_{DS}^2\beta_{EDP|IM}^2\right)} \tag{4}$$

where $\lambda_{IM,50}^{DS}$ is the mean annual frequency of exceeding of the median IM causing a DS (associated to 50% probability of exceedance) and k_{DS} is the slope of the hazard curve for the median IM causing the DS. From the quantification of the risk for both model configurations (undeformed and deformed), monetary losses could be estimated in the case of earthquake occurrence for each specific performance. This quantification can easily support the transportation managers in near-future decisions, where a strong increment of λ_{DS} from the undeformed case to the deformed case implies a timely structural and geotechnical intervention, while a limited reduction could lengthen the time.

Case-Study Application of the Proposed Procedure: Santo Stefano Viaduct

Description of the S. Stefano Viaduct and landslide-induced deformations

The "Santo Stefano" Viaduct is placed on the Bradanica road, which links the municipalities of Matera and Candela, between the regions Basilicata and Puglia, Southern Italy. The bridge was built in 2013 to overpass the Santo Stefano canal. It extends for about 180 m with six spans. A graphic description of the case-study bridge is reported in Fig. 4. The continuous superstructure is composed of four precast U-shaped girders with height of 1.80 m, covered by an RC slab having a thickness equal to 0.25 m. The piers are founded on large-diameter bored piles. Two abutments, consisting of RC walls, were built to support the access embankments

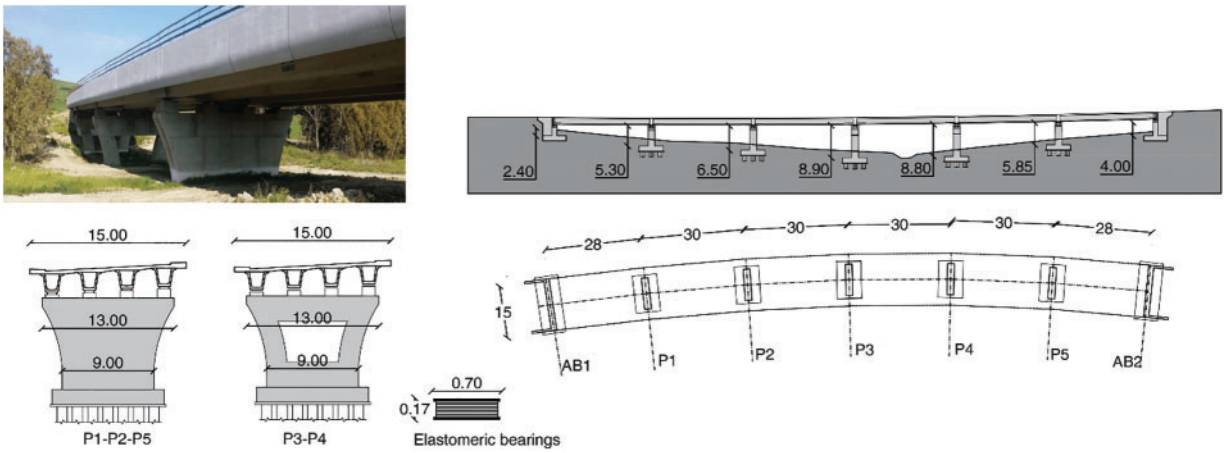

Figure 4. Description of the case-study bridge (photo, planimetric view, longitudinal view)

Table 1. Characteristics of the elastomeric bearings

Effective stiffness (k_h) [kN/mm]	Vertical stiffness (k_v) [kN/mm]	Elastomer diameter [mm]	Elastomer thickness [mm]	Total height [mm]	Side total length [mm]	Displacement capacity Δ_{max} [m]	Shear modulus (G) at $\gamma = 1$ [MPa]
3.08	2617	700	100	237	750	0.2	0.8

to the viaduct. The piers present height ranging from 5.70 and 8.90 m. As shown in Fig. 4c, three wall-type piers exhibit a like-trapezoidal shape with variable cross-section dimensions along the height, while the two highest piers are characterized by framed structure. The girders are connected to the piers through a line of elastomeric bearings placed on baggies. Four bearings are placed on each pier and designed to present an equivalent viscous damping equal to about 12%. Properties assigned to elastomeric bearings are listed in Table 1. In the end, it is worth noting that the bridge presents a slight curvature along its longitudinal extension, with a radius of about 700 m. In Fig. 4, a photo of the bridge, a planimetric view and a longitudinal view are reported.

On the basis of the preliminary in-situ observations, two specific monitoring campaigns were performed to identify the real causes of the bridge motion: (a) a geotechnical monitoring; (b) a topographic monitoring. The geotechnical monitoring was characterized by a combination of piezometers and inclinometers in the points of greater deformation (abutment in Candela direction), in order to highlight deep sliding surfaces. The results showed a sliding surface at 14 m below ground level, with an observed displacement of 2.5 cm in 3 months, which provokes the failure of some inclinometers. Piezometric measurements showed, in Candela direction, a piezometric level of about $1 \div 2$ m depth from the surface while, on the Matera side, it was close to ground level.

The topographic monitoring was elaborated by a precise measurement campaign aimed to identify all displacements with a millimetric accuracy. It was characterized by several measures made each three months and by using a total station and some measuring prisms placed on the structural elements of the bridge. The results show the evolution of the phenomenon, which was identified with a motion of the piers and abutments in the impluvium direction. From the global phenomenon point of view, the entire bridge was moving in the direction of the curvature radius center caused by the landslide, and each pier was subjected to a rigid motion. In the subsequent years, others monitoring campaigns were proposed to better characterize the phenomenon. Herein, of interest is not to define all experimental campaigns, but the definition of the mitigation actions to limit the landslide. To this scope, three drainage wells were inserted to intercept groundwater and lower neutral pressures in foundation soils and, thus, limit movements. In addition, a structural health monitoring system was permanently placed on the structure, with the aim to monitor all the effects that the observed phenomenon has on the bridge over the time.

In conclusion, from the structural point of view, some interventions were carried out: (a) controlled demolition of the abutment back-walls in the contact areas with the beams and reconstruction of the back-walls to restore the original gap size; (b) replacement of deformed bearing devices (lifting of the superstructure, removal of the deformed elastomeric bearings as shown in Fig. 5 and positioning of new ones).

Numerical modeling

Although the deformed elastomeric bearings were replaced and appropriate mitigation interventions were carried out to prevent further damages, the aim of this study is to assess the sensitivity of the seismic fragility of the bridge affected by landslide-induced deformation. In other words, the goal is to evaluate the seismic risk and damage probability referring to the evaluation and monitoring time period in which the elastomeric bearings presented a preliminary deformation.

Figure 5. Permanent deformation observed on the HDRBs, after one year from the bridge construction

To this scope, the framework defined in Section 3 was employed. It is worth noting that this approach should be adopted in cases similar to the analyzed one to evaluate variation in seismic fragility and risk considering long time periods ranging from the observation of the phenomenon to the execution of interventions. Additionally, the variation in seismic risk measured by the presented methodology should be adopted as a decision support for transport authority's operators which are in charge for defining if interventions are needed or not.

First, the numerical model of the bridge was created without considering any elastomeric bearing deformations (referred to as Model 1-Undeformed hereafter). In this study, the numerical model was built in SAP2000 software[41], although any software package suitable for bridge modeling can be adopted. The modeling strategy shown in Fig. 2 was used. In detail, all piers were modeled as frame elements fixed at the base, while abutments were simulated as fixed supports on which elastomeric bearings are leaned. The deck was simulated as a single frame element connected to the piers through a set of two-node links simulating the elastomeric bearings. As anticipated in sub-Section 3.3, this assumption strongly reduces modeling efforts in seismic analysis where the superstructure is considered to respond elastically and to simulate a realistic seismic mass distribution along the bridge length. To the frame simulating the superstructure, distributed loads were addressed, accounting for the seismic combination[42] of the structural and non-structural loads. These loads were considered according to the original drawings. Despite the bridge presents a slight curvature ratio along its longitudinal direction, the simplification of straight trend was assumed to penalize the response in transverse direction under horizontal actions (no longitudinal action components were considered). The nonlinear response of elastomeric bearings was simulated by using multilinear-plastic links, in which the backbone was defined according to Table 2, while the hysteresis loop was defined considering a kinematic hysteretic behavior.

The second model (hereafter referred to as Model 2-deformed) reflects the features of Model 1, while introducing some modifications accounting for landslide-induced effects. First, the displacements measured by means of the topographic monitoring system were assigned to the base node of substructure components in transverse direction. Additionally, the backbone response assigned to the elastomeric bearings were modified considering the effect of rotation of the upper plate, according to the approach proposed by Moghadam and Konstantinidis[29]. All the values of the landslide-induced base displacements and bearing-specific nonlinear parameters, in terms of yielding and ultimate force (F_y and F_u, respectively) and displacement (Δ_y and Δ_u) are reported in Table 2. The sign + or – indicates for the forces, the positive and negative values in the backbone.

Given the numerical models, eigenvalue analyses were performed. The first period of vibration for Model 1 and Model 2 is equal to 1.60 s. Therefore, a record selection was performed as follows. First, a target spectrum for the site of interest is extracted considering an expected PGA equal to 0.40 g. A dataset of ten scaled natural records is first extracted by using the tool REXEL proposed by Iervolino et al.[43]. Spectrum-compatibility was checked with respect to the target spectrum and by using the Eurocode 8 provisions that suggest to select records in order to have differences between mean and target spectra of +30% and −10% for a range of periods of interest. The period of interest is fixed between 1.00 and 2.50 s considering that high-frequency modes are of minor importance for the analyzed case study. Subsequently, this record dataset is further scaled for achieving a PGA of the target spectrum equal to 0.30 and 0.20 g. In this way, a total of 30 ground-motion records is obtained. In Fig. 6a, elastic (5% damping) acceleration spectra of the selected set of ground motion records, mean and target spectra are reported. Additionally, to perform the risk assessment, the hazard curve (Fig. 6b) for the site of interest is extracted by using the tool REASSESS by Chioccarelli et al.[44].

Fragility analysis and risk assessment

On this base, 30 runs of NRHA were performed on both numerical models. For the sake of simplicity, given the illustrative purpose of this study, only the seismic response in transverse direction was considered. For both models, a post-processing check was performed after NRHAs to avert the occurrence of nonlinear mechanisms in the structural elements (i.e., in the piers). EDP were extracted in terms of shear strain γ demand of the elastomeric bearings. To interpret the achieved results and for describing how NRHA results were elaborated to obtain bearing shear strains γ, the outcomes for a randomly selected record (in terms of

Table 2. Modeling parameters of elastomeric bearings and landslide-induced base displacement, indicated for each vertical element and model

Model	Component	Base displacement (m)	F_y[kN]	F_u [kN]	Δ_y [m]	Δ_u [m]
Model 1	All	–	40	627	0.004	0.20
Model 2	Ab1	0.10	40	−541/+713	0.004	0.20
	P1	0.12	40	−563/+691	0.004	0.20
	P2	0.07	40	−585/+669	0.004	0.20
	P3	0.03	40	−538/+716	0.004	0.20
	P4	0.06	40	−573/+781	0.004	0.20
	P5	0.07	40	−517/+737	0.004	0.20
	Ab1	0.07	40	−494/+760	0.004	0.20

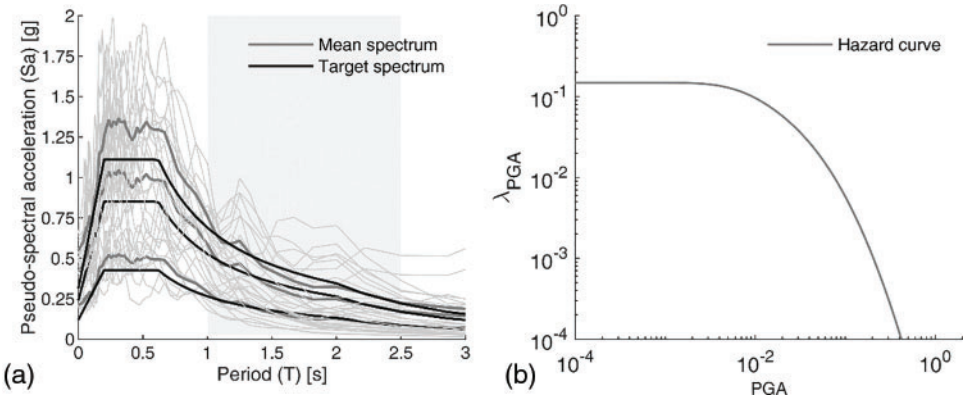

Figure 6. a) Acceleration spectra for the selected set of records, mean and target spectra; b) Hazard curve

displacement registered for significant nodes) are shown in Figs. 7a and 7b. The initial displacement (initial condition for NRHA) of the bearing top node is indicated as continuous dark-grey curve. Clearly, this is equal to 0 for model 1, while it reflects the initial landslide-induced deck deformed shape for model 2. The maximum displacement demand registered for bearing top nodes during NRHA (in positive and negative direction) is also presented via dashed light-grey curves. The position of the lower bearing node is additionally indicated by means of black circular markers. Note that no significant displacements of the lower bearing node (i.e., pier top node) are observed during the seismic excitations. Fig. 7c reports the shear strain demand calculated for the two models. The comparison between Figs. 7a and 7b shows the significant influence of the landslide-induced effects in the NRHA-based displacement profile. For model 1, the displacement demand for bearing devices reflects a "parabolic" distribution. This is also reflected on γ values for model 1 reported in Fig. 7c. The maximum demand was registered for the bearing device placed on the central pier (i.e., indicated as P3). Similar results were observed for the other NRHAs. For model 2, the initial displacement pattern of bearing top nodes reflects the hyperstatic response of the superstructure under landslide-induced differential pier displacements (black markers). Therefore, the bearings were subject to an initial shear strain demand before the NRHA was conducted. The displacement demand induced by NLRHA exhibited an irregular shape with respect to the former case. For each bearing device, the shear strain demand was computed considering the differential displacement between the top and the bottom nodes. As shown in Fig. 7c, this resulted in a general increase in shear strain demand with respect to model 1 for the bearing devices. Also, in this case, the highest γ was related to the central pier.

The maximum γ registered among the bearing devices was extracted for each NRHA and used as EDP for fragility analysis. The peak ground acceleration (PGA) was considered as IM. To compute fragility curves, the continuous relationship between IM and EDP was estimated by employing the power law approximation, as suggested by Cornell et al.[45]. Four damage states (DS) were considered, associated with slight, moderate, extensive, and complete damage conditions, as suggested by Zhang and Huo[38]. DS thresholds are indicated in Table 2. Note that although elastomeric bearings may experience shear strain values up to 400%, the DS4 was associated with a limit shear strain equal to 250% in order to avoid large deck displacements and deck unseating[25].

Accounting for all the above-mentioned DSs, fragility curves for the bridges in Model 1 and Model 2 are reported in the graphs in Fig. 8. As expected, landslide-induced deformations on elastomeric bearing induced a general increase in fragility for all the considered DSs. Observing the fragility

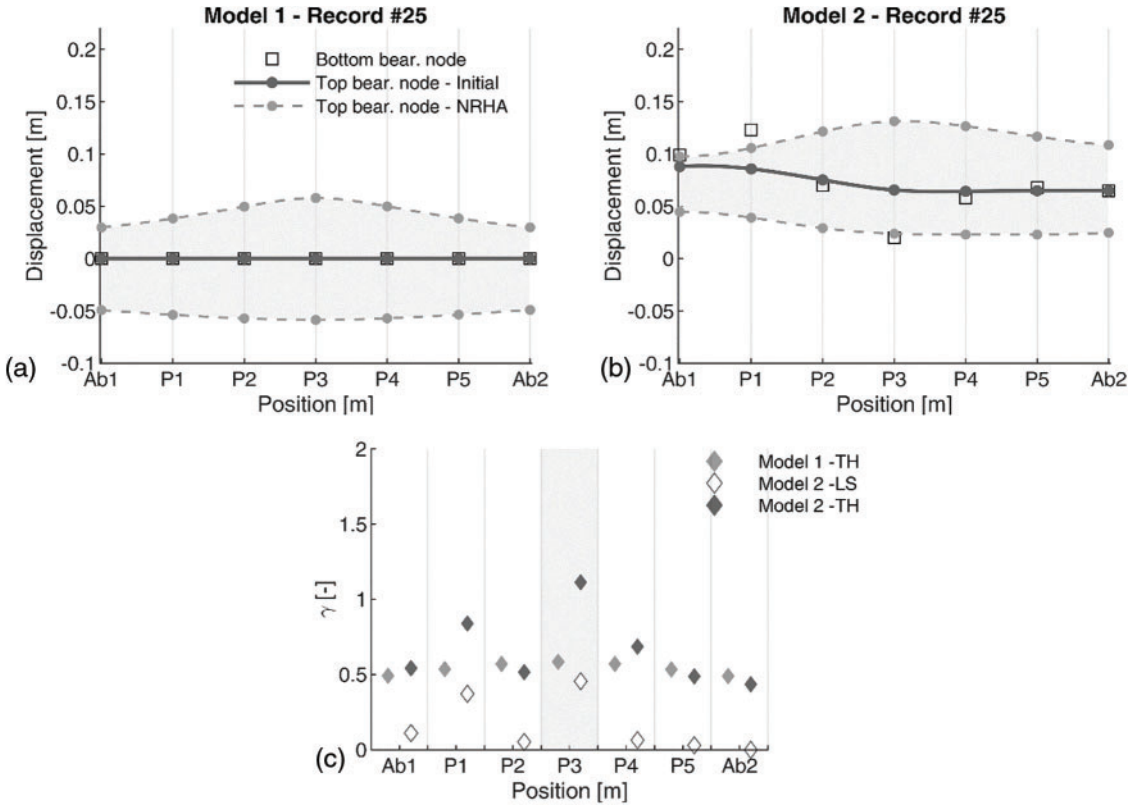

Figure 7. Displacement demand calculated for a randomly selected record (a) Model 1 and (b) Model 2 and shear strain demand (c)

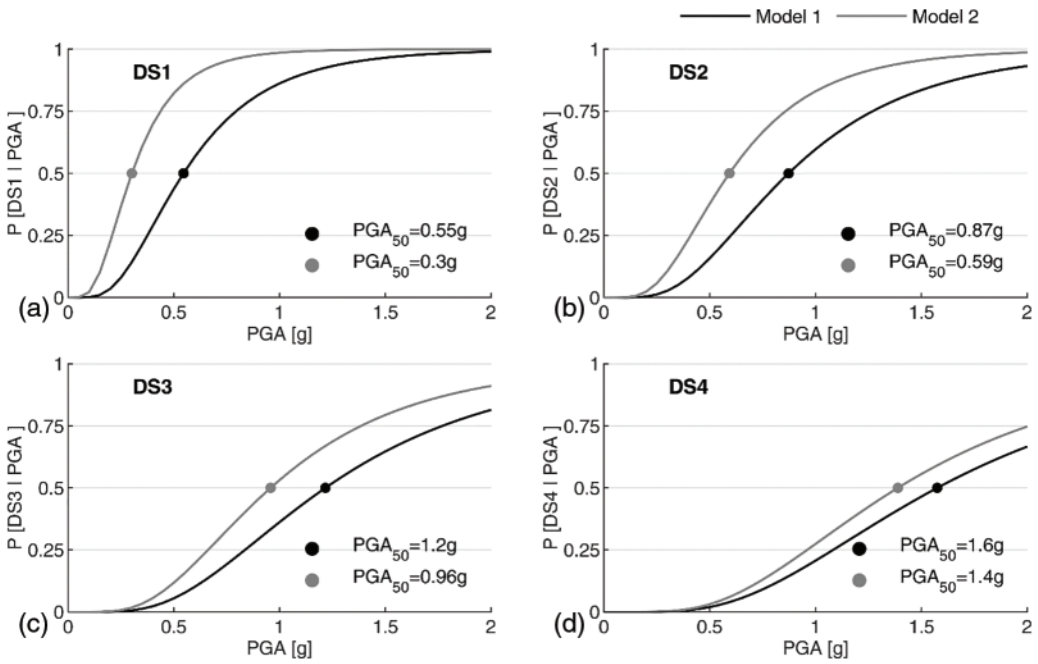

Figure 8. Fragility curves of Model 1 (Undeformed) and Model 2 (Deformed), accounting for damage states DS1, DS2, DS3, DS4

curves, the most significant fragility variation was registered to DS1 (Fig. 8a), where the median value of the fragility curve (probability equal to 50% of exceeding a given DS) presented an increase equal to 44.7%. Conversely, the influence of permanent landslide-induced deformations on elastomeric bearings decreased for increasing DS limits. Indeed, the variation in median fragility curves between Model 1 and Model 2 decreased to 32.0%, 21.2%, and 11.8%

Table 3. Damage state thresholds in terms of shear strain γ

Demand parameter	DS1	DS2	DS3	DS4
γ_{DS} (%)	100%	150%	200%	250%

Table 4. λ_{DS} values for MODEL 1 and MODEL 2, accounting for damage states DS1, DS2, DS3, and DS4

$\lambda_{DS}\left[10^{-3}\right]$	DS1	DS2	DS3	DS4
Model 1–Undeformed	0.1863	0.0429	0.0134	0.0050
Model 2–Deformed	0.8955	0.1406	0.0298	0.0076

for DS2, DS3, and DS4, respectively. For all the DS, a similar fragility dispersion was computed, equal to 0.5 and 0.55 for Model 1 and Model 2. As expected, the obtained results suggest that the initial landslide-induced phenomenon on the elastomeric bearings assumes a more important effect on the lower DSs (e.g., DS1 and DS2) than the higher DSs (e.g., DS3 and DS4). This is because the value of the initial displacement, expressed in terms of γ, represents a higher contribute with reference to the threshold values (see Table 3) for the lower DSs than the one observed with reference to the threshold values for the higher DSs.

Finally, from the probabilistic measure of the damage, the risk was quantified by means of the λ_{DS} values. Results for Model 1 and Model 2 and for all the considered damage states are reported in Table 4. As expected, the values of λ_{DS} were significantly higher for Model 2 than Model 1. The highest increase was observed for DS1, where λ_{DS} reaches $0.89 * 10^{-3}$ for Model 2, with respect to $0.18 * 10^{-3}$ for Model 1. Conversely, a slight increase was observed for DS4 where λ_{DS} values are comparable. Clearly, these outcomes in terms of risk are significantly correlated to the adopted hazard curve reflecting the hazard condition of the bridge location.

Conclusions and Further Developments

The study concerns seismic fragility and risk of reinforced concrete (RC) bridges isolated via elastomeric bearing devices subjected to differential displacements induced by slow-moving landslides. The paper describes a practical approach to investigate the seismic fragility and risk of RC bridges isolated via elastomeric bearings, which experience preliminary deformations induced by the landslide-induced effects involving the bridge. The proposed methodology was based on numerical modeling to represent the structure in undeformed and deformed conditions and adopts nonlinear response history analyses to generate fragility curves according to the cloud-based approach. Using two numerical models, it is possible to quantify the influence of landslide-induced effects on seismic fragility and risk and to provide decision-support indications to transport authorities in charge of ensuring the safety of bridges.

The proposed approach was tested on a real-life case study, the *Santo Stefano* viaduct in Italy, which was subjected in the past to elastomeric bearing deformation given by an active landslide phenomenon. The application proved that for the case at hand, the landslide-induced effects had a strong influence on the seismic fragility, particularly referring to the low-damage state. This effect was weakened for more severe damage states. Clearly, the results achieved are strictly related to the case study analyzed. However, the presented methodology can be adopted by means of typological approaches and parametric analysis to estimate the influence on fragility and risk by varying the intensity of landslide-induced differential displacements. Additionally, further developments of the methodology may consider introducing other components in the numerical model, such as shear keys and pounding effects, which can be significant for two-directional seismic analysis.

Acknowledgements

The authors acknowledge the Italian Consortium FABRE for the financial support.

References

[1] Gidaris I, Padgett JE, Barbosa AR, et al. Multiple-hazard fragility and restoration models of highway bridges for regional risk and resilience assessment in the United States: state-of-the-art review. *J Struct Eng*. 2017;143(3):04016188.

[2] Borzi B, Ceresa P, Franchin P, et al. Seismic vulnerability of the Italian roadway bridge stock. *Earthq Spectr*. 2015;31(4):2137–2161.

[3] Abarca A, Monteiro R, O'Reilly GJ. Exposure knowledge impact on regional seismic risk assessment of bridge portfolios. *Bull Earthq Eng*. 2022;20(13):7137–7159.

[4] Cademartori M, Sullivan TJ, Osmani S. Displacement-based assessment of typical Italian RC bridges. *Bull Earthq Eng*. 2020;18:4299–4329.

[5] Gentile R, Nettis A, Raffaele D. Effectiveness of the displacement-based seismic performance assessment for continuous RC bridges and proposed extensions. *Eng Struct*. 2020;221(2):110910.

[6] Nettis A, Iacovazzo P, Raffaele D, et al. Displacement-based seismic performance assessment of multi-span steel truss bridges. *Eng Struct*. 2022;254(2):113832.

[7] Peduto D, Elia F, Montuori R. Probabilistic analysis of settlement-induced damage to bridges in the city of Amsterdam (The Netherlands). *Transp Geotech*. 2018;14:169–182.

[8] Nettis A, Massimi V, Nutricato R, et al. Satellite based interferometry for monitoring structural deformations of bridge portfolios. *Autom Constr*. 2023;147:104707.

[9] Anisha A, Jacob A, Davis R, et al. Fragility functions for highway RC bridge under various flood scenarios. *Eng Struct*. 2022;260:114244.

[10] Pregnolato M, Winter AO, Mascarenas D, et al. Assessing flooding impact to riverine bridges: an integrated analysis. *Nat Hazards Earth Syst Sci*. 2022;22(5):1559–1576.

[11] Yilmaz T, Banerjee S, Johnson PA. Uncertainty in risk of highway bridges assessed for integrated seismic and flood hazards. *Struct Infrastruct Eng*. 2018;14(9):1182–1196.
[12] Gehl P, D'Ayala D. System loss assessment of bridge networks accounting for multi-hazard interactions. *Struct Infrastruct Eng*. 2018;14(10):1355–1371.
[13] Mantakas A, Tsatsis A, Loli M, et al. Seismic response of a motorway bridge founded in an active landslide: a case study. *Bull Earthq Eng*. 2023;21:605–632. doi:10.1007/s10518-022-01544-3.
[14] Ministero delle infrastrutture (MIT). Linee guida per la classificazione e gestione del rischio, la valutazione della sicurezza ed il monitoraggio dei ponti esistenti. 2020 (in Italian).
[15] Calvi GM, Moratti M, O'Reilly GJ, et al. Once upon a time in Italy: the tale of the morandi bridge. *Struct Eng Int*. 2022;29:198–217. doi:10.1080/10168664.2018.1558033.
[16] Dezfuli F, Alam MS. Effect of different steel-reinforced elastomeric isolators on the seismic fragility of a highway bridge. *Struct Control Health Monitor*. 2017;24(2):e1866.
[17] Wei W, Yuan Y, Igarashi A, et al. Experimental investigation and seismic fragility analysis of isolated highway bridges considering the coupled effects of pier height and elastomeric bearings. *Eng Struct*. 2021;233(7):111926.
[18] Kunde MC, Jangid RS. Seismic behavior of isolated bridges: a-state-of-the-art review. *Electron J Struct Eng*. 2003;3:140–170.
[19] Gardoni P, Trejo D. Probabilistic seismic demand models and fragility estimates for reinforced concrete bridges with base isolation. *Earthq Struct*. 2013;4(5):527–555.
[20] Siqueira GH, Sanda AS, Paultre P, et al. Fragility curves for isolated bridges in eastern Canada using experimental results. *Eng Struct*. 2014;74:311–324.
[21] Bayat M, Daneshjoo F, Nistico N, et al. Seismic evaluation of isolated skewed bridges using fragility function methodology. *Comput Concrete*. 2017;20(4):419–427.
[22] Hassan AL, Billah AM. Influence of ground motion duration and isolation bearings on the seismic response of base-isolated bridges. *Eng Struct*. 2022;222(2):111129.
[23] Maghsoudi-Barmi A, Khansefid A, Khaloo A, et al. Probabilistic seismic performance assessment of optimally designed highway bridge isolated by ordinary unbonded elastomeric bearings. *Eng Struct*. 2021;247(3):113058.
[24] Kurino S, Wei W, Igarashi A. Seismic fragility and uncertainty mitigation of cable restrainer retrofit for isolated highway bridges incorporated with deteriorated elastomeric bearings. *Eng Struct*. 2021;237(3):112190.
[25] Aghaeidoost V, Billah AM. Sensitivity of seismic fragility of base-isolated bridges to lead rubber bearing modeling technique. *Struct Control Health Monit*. 2022;e2971.
[26] Kikuchi M, Nakamura T, Aiken ID. Three-dimensional analysis for square seismic isolation bearings under large shear deformations and high axial loads. *Earthq Eng Struct Dyn*. 2010;39(13):1513–1531.
[27] Vemuru VS, Nagarajaiah S, Mosqueda G. Coupled horizontal–vertical stability of bearings under dynamic loading. *Earthq Eng Struct Dyn*. 2016;45(6):913–934.
[28] Mitoulis SA. Uplift of elastomeric bearings in isolated bridges subjected to longitudinal seismic excitations. *Struct Infrast Eng*. 2015;11(12):1600–1615. doi:10.1080/15732479.2014.983527.
[29] Moghadam SR, Konstantinidis D. Finite element study of the effect of support rotation on the horizontal behavior of elastomeric bearings. *Compos Struct*. 2017a;163:474–490.
[30] Moghadam, SR, Konstantinidis D. Simple mechanical models for the horizontal behavior of elastomeric bearings including the effect of support rotation. *Eng Struct*. 2017b;150:996–1012.
[31] Moghadam SR, Konstantinidis D. Experimental and analytical studies on the horizontal behavior of elastomeric bearings under support rotation. *J Struct Eng*. 2021;147(4):04021024.
[32] Zhang Z, Yang L, Xiang S, et al. New macroscopic model for predicting the horizontal behavior of elastomeric bearings under end-plate rotation. *Structures*. 2023;47(1):1086–1093.
[33] Pishgahi F, Taghikhany T. Mechanical model for seismic nonlinear behavior of rubber bearings with end-rotation in highway bridges. *Structures*. 2023;47(4):875–890.
[34] Hendy CR, Sandberg J, Shetty NK. Recommendations for assessment Eurocodes for bridges. In: *Proceedings of the Institution of Civil Engineers-Bridge Engineering*; 2011; Thomas Telford Ltd, pp. 3–14.
[35] Nielson BG, DesRoches R. Seismic fragility methodology for highway bridges using a component level approach. *Earthq Eng Struct Dyn*. 2007;36(6):823–839.
[36] Jalayer F, Ebrahimian H, Miano A, et al. Analytical fragility assessment using unscaled ground motion records. *Earthq Eng Struct Dyn*. 2017;46(15):2639–2663.
[37] ASCE 7–16. *Minimum Design Loads for Buildings and Other Structures: Commentary*. American Society of Civil Engineers; 2017. doi:10.1061/9780784412916.
[38] O'Reilly GJ. Seismic intensity measures for risk assessment of bridges. *Bull Earthq Eng*. 2021;19(9):3671–3699. doi:10.1007/s10518-021-01114-z.
[39] Zhang J, Huo Y. Evaluating effectiveness and optimum design of isolation devices for highway bridges using the fragility function method. *Eng Struct*. 2009;31(8):1648–1660.
[40] Jalayer F, Cornell CA. A technical framework for probability-based demand and capacity factor (DCFD) seismic formats. 2002. https://peer.berkeley.edu/sites/default/files/0308_f._jalayer_c._allin_cornell.pdf.
[41] CSI. *SAP2000 v.24, Advanced Structural Analysis Program–Manual*. Berkeley: Computer and Structures Inc.; 2022.
[42] DM 17/01/2018. *Aggiornamento delle Norme Tecniche per le Costruzioni*. Gazzetta Ufficiale n. 42. February 20. Rome; 2018 (in Italian).
[43] Iervolino I, Galasso C, Cosenza E. REXEL: Computer aided record selection for code-based seismic structural analysis. *Bull Earthq Eng*. 2010;8:339–362. doi:10.1007/s10518-009-9146-1.
[44] Chioccarelli E, Cito P, Iervolino I, et al. REASSESS V2.0: software for single- and multi-site probabilistic seismic hazard analysis. *Bull Earthq Eng*. 2019;17:1769–1793. doi:10.1007/s10518-018-00531-x.
[45] Cornell CA, Jalayer F, Hamburger RO, et al. Probabilistic basis for 2000 SAC federal emergency management agency steel moment frame guidelines. *J Struct Eng*. 2002;128(4):526–533.

BER the international journal of bridge engineering management and research

A New Methodology for the Diagnosis and Monitoring of Bridges Under Slow Deformation Phenomena

Andrea Meoni[1,*]; Laura Ierimonti[1]; Elisabetta Farneti[1]; Matteo Castellani[1]; Filippo Filippucci[1]; Agnese Natali[2]; Simone Celati[2]; Fabrizio Scozzese[3]; Michele Morici[3]; Nicola Cavalagli[1]; Ilaria Venanzi[1]; Anil Kumar Agrawal[4]; Andrea Dall'Asta[3]; Walter Salvatore[2]; and Filippo Ubertini[1]

Submitted: 06 February 2024 **Accepted:** 05 April 2024 **Publication date:** 03 September 2024

DOI: 10.70465/ber.v1i1.1

Abstract: Roadway bridges can be subjected to several pathologies affecting their structural performance during operational conditions. Among others, slow deformation phenomena due to landslides often represent the primary cause of the onset of damage and collapse mechanisms. The timely identification of slow deformation phenomena on bridges and viaducts, as well as the evaluation of their extent and evolution over time, are therefore of crucial importance for preserving the safety conditions of road networks. In common practice, the preliminary analysis of slow deformation phenomena could be carried out over large geographical areas; hence, it can be used by managing institutions to set intervention priorities among the assets under their responsibility. In this regard, this paper proposes a new methodology for the diagnosis and monitoring of bridges under the effects of slow deformation phenomena based on the combined use of Synthetic Aperture Radar Interferometry (InSAR) techniques, visual inspections, geometric surveys, destructive and non-destructive testing methods, and numerical analyses. Specifically, InSAR is adopted to remotely identify bridges affected by slow deformation phenomena within large geographical areas/road networks. Then, visual inspections are carried out on the identified structures to investigate their defectiveness and the detected deformation phenomenon. Depending on the evaluated damage state, a bridge may be subjected to continuous InSAR monitoring, thus enabling the systematic analysis of the evolution of the deformation phenomenon and relevant anomalies over time or an accurate structural assessment via numerical analyses. In this last circumstance, information gathered from geometric surveys and field tests can be used for the fine-tuning of the numerical models of the structures. A practical application of the proposed methodology for the diagnosis and monitoring of a curved roadway bridge subjected to landslide phenomena is also presented in the paper for illustrative purposes. Overall, the results obtained in the case study provide a sound demonstration of the effectiveness of the proposed approach.

Author keywords: Structural health monitoring; SAR interferometry; operational modal analysis; numerical analysis; prestressed concrete bridges

Introduction

Bridges and viaducts are crucial infrastructural assets for transportation networks; in some cases, they also hold historical and strategic importance. To avoid significant losses both in terms of human lives and economic resources, it is essential to maintain their functionality, detect damage at early stages, and prevent collapses.[1–3] During their lifetime, bridges and viaducts can experience material deterioration, structural aging, direct damage due to natural hazards, such as earthquakes, strong wind, and so on, as well as damage due to slow deformation phenomena, such as landslides, subsidence, ground consolidation, foundation scouring, and prestress losses. In recent years, non-destructive techniques have been spreading out, underlying Structural Health Monitoring (SHM) methodologies. SHM involves the continuous acquisition and post-processing of data using contact or contactless sensing systems. This technology provides essential information about the structural integrity of constructions, reduces risks, and guides preventive maintenance interventions.[4–7] Recently, traditional SHM techniques have been paired with Synthetic Aperture Radar Interferometry (InSAR)-based methods. InSAR is a well-established technology that measures and monitors movements on the ground, exploiting SAR observations acquired by satellites orbiting at more than 500 km above the Earth's surface.

*Corresponding Author: Andrea Meoni.
Email: andrea.meoni@unipg.it
[1]Department of Civil and Environmental Engineering, University of Perugia, Italy
[2]Department of Civil and Industrial Engineering, School of Engineering, University of Pisa, Italy
[3]School of Architecture and Design, University of Camerino, Italy
[4]Department of Civil and Environmental Engineering, The City College of the City University of New York, USA

Discussion period open till six months from the publication date. Please submit separate discussion for each individual paper. This paper is a part of the Vol. 1 of the International Journal of Bridge Engineering, Management and Research (© BER), ISSN 3065-0569.

This technique, which is particularly suitable for detecting and tracking slow deformations due to the dependence of the frequency of measurements on the satellite's revisit time over the area of interest, has recently been used for SHM of buildings and infrastructures.[8–14] The above-mentioned technique has significant benefits. Firstly, it allows for displacement information to be obtained on multiple points of a single structure without having to access the site physically. Secondly, it can monitor vast regions or even entire bridge inventories at a relatively low cost. Additionally, high-resolution satellite acquisitions can provide millimeter-scale precision for displacement measurements along the Line of Sight (LOS), which connects the satellite radar antenna to the target on the Earth's surface. To cite a few examples of the most recent and prominent studies in the scientific literature dealing with InSAR-based bridge monitoring, in Farneti et al.,[15] a post-processing methodology has been developed that can use SAR observations from two different viewing geometries to derive a two-dimensional reconstruction of the bridge's movements over time and quantify the uncertainties of the estimated displacements. An approach to identify and classify bridges experiencing slow deformations in large assets, then assign them monitoring/assessment priority classes based on information from InSAR data, has been proposed in Nettis et al.[16]. The effectiveness of InSAR data for monitoring the structural response of diverse bridge components, such as access lanes, piers, spans, and bearing supports, thus allowing the identification of possible unexpected behavior, has been demonstrated in Tonelli et al.[17].

In this context, it is crucial to develop systematic methodologies to account for InSAR data, with the main objective of making informed decisions and scheduling interventions, minimizing risks, progressive damages, and costs in the management of bridge inventories. The exploitation of SAR technology can provide a fundamental contribution to pathologies understanding when properly combined with on-site structural monitoring and survey activities. In this paper, an integrated approach combining InSAR-based monitoring with the outcomes from visual inspections, geometric surveys, and additional non-destructive techniques is proposed for the diagnosis and monitoring of bridges and viaducts experiencing slow deformation phenomena, especially those caused by landslides. InSAR-based methods are utilized for remote detection of bridges affected by gradual deformation phenomena across road networks. On-site visual inspections are conducted on the identified bridges to evaluate their state of deterioration and the extent of detected deformation phenomena. Depending on the severity of their damage state, bridges may be subjected to continuous InSAR monitoring to track the progression of slow deformation processes or advanced numerical analysis to predict their remaining service life. The results of geometric surveys and additional non-destructive testing help to enrich the knowledge of bridges and refine numerical models for better estimation of their remaining life. The proposed methodology is applied to a real case study bridge characterized by critical structural defectiveness to provide a sound demonstration of the effectiveness of the approach. The rest of the paper is structured as follows. The proposed methodology is introduced together with the case study bridge and the performed experimental investigations. Then, the numerical models defined to replicate the mechanical response of the case study bridge are illustrated. Afterward, experimental and numerical results are presented. A closing section ends the paper, outlining comments and remarks.

Methodology Description

Fig. 1 illustrates the flowchart of the proposed methodology for the diagnosis and monitoring of bridges and viaducts under the effects of slow deformation phenomena due to landslides. The InSAR-based monitoring is adopted to remotely identify bridges affected by slow deformation phenomena within large geographical areas/road networks. SAR screening methods aim to identify assets exhibiting displacement histories characterized by clear trends indicating the accumulation of irreversible deformation over time, and therefore the progression toward a potential critical condition.

Once a bridge affected by permanent deformations is remotely identified, on-site visual inspections are carried out to assess and quantify the entity of the deformation phenomenon, hence its interaction with the asset. The defectiveness of the selected structure is also evaluated and compared with the results from past inspection activities when available. This last operation can provide meaningful indications of the evolution over time of the defects detected on the asset. Based on the outcomes from visual inspections,

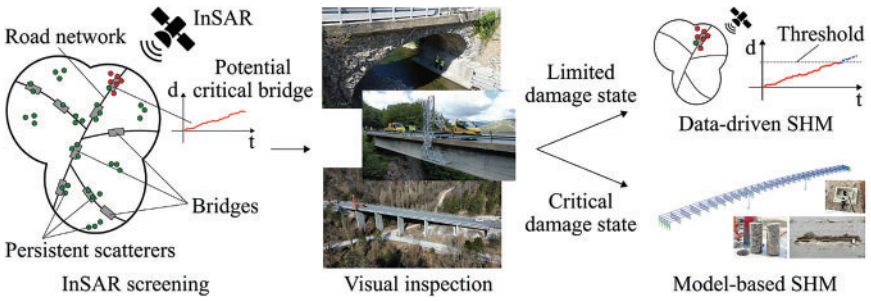

Figure 1. Conceptual flowchart of the proposed methodology for the diagnosis and monitoring of bridges under the effects of slow deformation phenomena

the methodology proposes two different monitoring strategies for the asset under investigation. In the first scenario, a data-driven SHM approach is adopted. Specifically, a bridge can be subjected to continuous InSAR monitoring when the outcomes from visual inspections do not highlight critical structural conditions. In this circumstance, therefore, the remote monitoring of the asset is primarily aimed at detecting potential anomalies in the evolution of the slow deformation phenomenon at an early stage. Alarm thresholds related to the trends of the displacements monitored via InSAR can be set based on engineering judgment, which may consider the typology of the bridge, its static scheme, and the features of the landslide, to name a few. When one or more thresholds are triggered, the authority responsible for the asset under continuous InSAR monitoring is promptly informed, and further inspections may be carried out on the bridge to assess its actual structural condition. Advanced processing of InSAR data can also be carried out to obtain information on the structural performance of the selected bridge. As an example, the evolution of the deformed configuration of the asset can be reconstructed to investigate potential alterations induced over time by the landslide-structure interaction. In the second scenario, namely when visual inspections point out critical structural conditions for the asset remotely identified via InSAR monitoring (e.g., due to the high defectiveness or the initiation/progression of damage mechanisms), a model-based SHM approach is considered. A numerical model of the asset under investigation is constructed and hence used to perform collapse simulations and estimate the residual life of the structure. The outputs from numerical analyses are used to integrate/validate those obtained from the processing of InSAR data and vice versa, thus achieving a comprehensive evaluation of the structural performance of the asset. In this scenario, extensive geometric surveys are carried out to aid the comprehension of the bridge-landslide interaction. Furthermore, field tests, including additional non-destructive techniques, can be performed on the asset to evaluate materials' mechanical properties, as well as potential modifications in the static and dynamic response of the structure with respect to its design configuration. The outcomes from field tests can also contribute significantly to the fine-tuning of the numerical model used to perform structural assessments.

Application Case Study

This section presents the case study bridge and the experimental investigations carried out to characterize its actual defectiveness and structural response.

Bridge description

The case study bridge [see Figs. 2a and 2b] has a planimetric development with a curved shape, with a total length of 66 m, measured along the supports. It has a static scheme of continuous beams on four supports (the right and left abutments plus two piers), with a central span of 36 m and two side spans of 15 m each. The deck of the bridge has a width of 7.50 m, of which 6.50 m is used for the carriageway and 0.50 m on each side for the safety barriers. The superstructure consists of a post-tensioned concrete slab with a rectangular cross-section and dimensions of 4.50 m × 1.10 m, from which two symmetrical cantilevers, each projecting 1.5 m, extend laterally [Fig. 2c]. The slope of the carriageway is constant and equal to 4% and 6% along the transversal and longitudinal directions, respectively. The piers are made of two overlapping elements; the lower element is made of ordinary Reinforced Concrete (RC), while the upper one is a slender rectangle-shaped RC element, which is equipped with a cylindrical hinge bearing support at the base and top and thus has a pendulum function; its rectangular cross-section has dimensions of 4.50 m × 0.90 m, measured between the hinges. The lower portion of the right pier is formed by a parallelepiped-shaped RC structure with a plan view section of 2.00 m × 4.50 m and a height of 4 m, which is made integral with the foundation plinth. The lower portion of the left pier is made of a first parallelepiped-shaped RC structure with a rectangular section of 2.00 m × 6.95 m and a height of 16 m, with an enlargement of 2.50 m in width and a height of about 2.00 m [see Fig. 2d]. Unlike the right pier, the left pier has a direct foundation, given the presence of the underlying rocky layer. The left abutment, connected to the superstructure by movable bearing supports, is made of RC and stands on a direct foundation. The height of the front wall, measured from the top of the foundation to the plane of the bearing supports, is 6.64 m, while the height of the foundation plinth is 1.50 m. The right abutment is the site of a fixed bearing support and is realized through an RC structure of variable height. In the downhill section, the front wall, measured from the top of the foundation to the support plane of the bearing supports, has a height of 3.25 m, while in the uphill section, it has a height of 1.50 m. The bridge is subject to a mountain landslide, inducing the deck to move towards the right abutment. As a result, the structure is characterized by critical defectiveness, as described in the following sections.

InSAR-based monitoring

To derive the temporal evolution of the displacements affecting the case study bridge, two stacks of SAR images acquired over the area of interest by the Italian satellite constellation COSMO-SkyMed were analyzed. The first dataset, acquired in ascending geometry (i.e., when the satellite navigates approximately from the South to North poles), was composed of 51 images covering the period between January 2018 and December 2021; the second set of images, acquired in descending pass (i.e., when the satellite travels from the North to South poles) consisted of 78 acquisitions recorded in the period between January 2018 and January 2022. The direction cosines of the ascending and descending LOS over the area of interest are summarized in Table 1. Processing the two image datasets through the Persistent Scatterer Pair (PSP) technique,[18] it was possible to extrapolate the displacement information for a set of sparse points, called Persistent Scatterers (PSs), located on the monitored structure and the ground in its proximity and corresponding to radiometrically stable targets within the monitoring period.

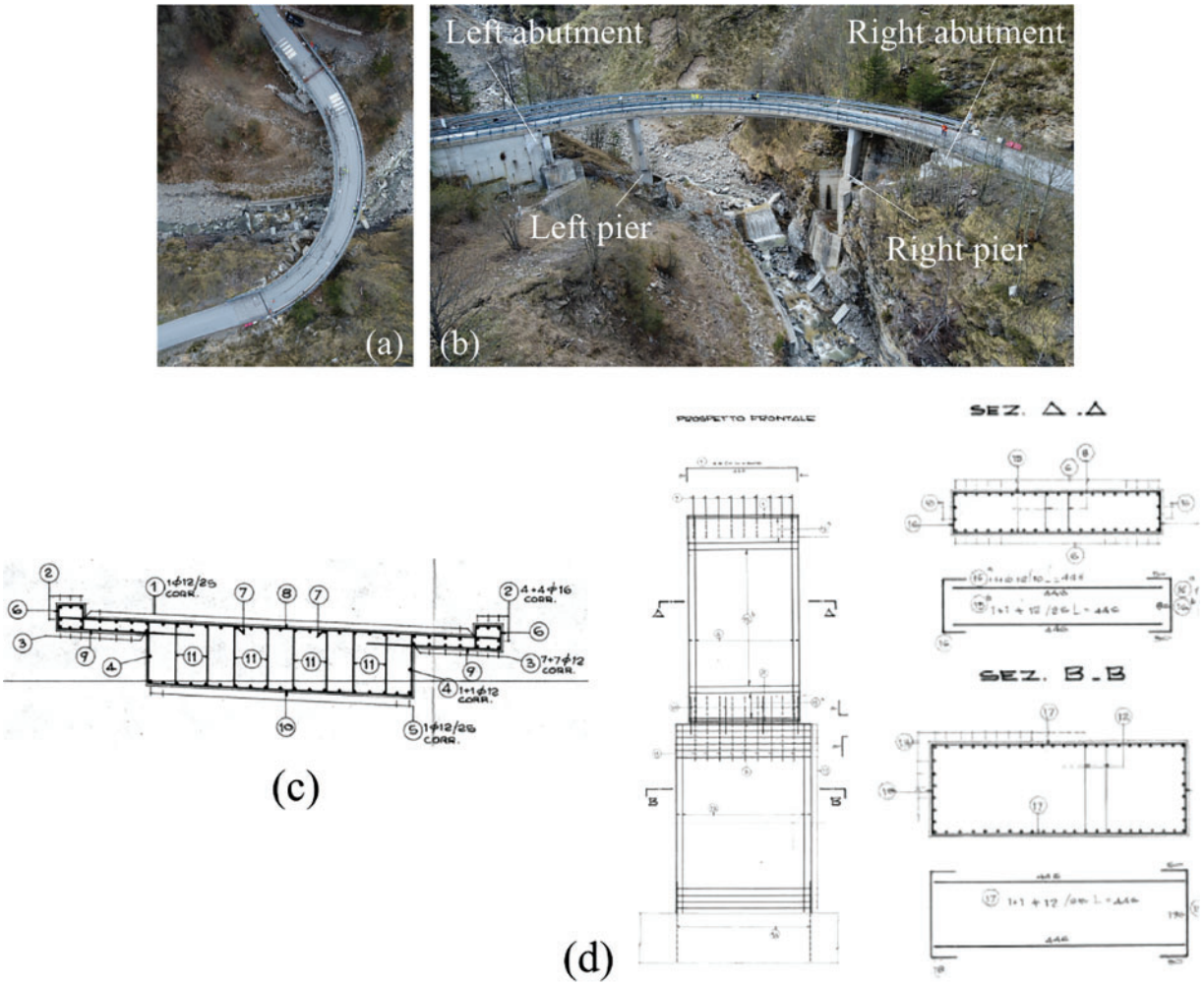

Figure 2. The case study bridge: (a) aerial view; (b) lateral view; (c) cross-section of the deck retrieved from the original technical drawings; (d) construction details of the left pier retrieved from the original technical drawings

Table 1. Direction cosines of the ascending and descending LOS of COSMO-SkyMed satellites over the studied area

	East	North	Vertical
Ascending geometry	−0.441646	−0.082075	0.893427
Descending geometry	0.548311	−0.1120473	0.828734

The position of the detected PSs had a metric precision in the three-dimensional space. In contrast, the associated displacement measurements had a millimeter-scale precision along the LOS direction, which connects the satellite radar antenna with the target on the ground.

Geometric surveys

A photogrammetric survey was conducted on the case study bridge to detect its geometry and structural configuration. Fig. 3 shows the conceptual flowchart describing the main steps of the geometric survey conducted through Unmanned Aerial Vehicle (UAV) photogrammetry. A drone model DJI Mini 2, with a 1/2.3″ CMOS sensor with 12 MP, was employed to scan the bridge by carrying out a total of nine flight missions. Six flights were carried out with the camera tilted zenithally by 60° and 45° to properly scan the deck of the bridge. Furthermore, three detailed flights, with a camera angle of 0° and 30°, were carried out to scan both piers. All the flight routes were carried out manually due to interfering vegetation. The percentage of overlap between the individual frames was equal to 80%. The acquired set of images was processed with a Structure from Motion software, named Metashape from Agisoft, to extract the point cloud of the sampled surfaces. Once obtained the point cloud of the bridge, hence converted to a textured 3D model, orthophotos of the piers were extracted with a Ground Sample Distance value of 7.09 mm/px. These pictures were further analyzed to determine the actual inclination of the piers with respect to the original configuration of their vertical axis.

Ambient vibration tests and modal identification

The dynamic behavior of the case study bridge was investigated by performing Ambient Vibration Tests (AVTs) on

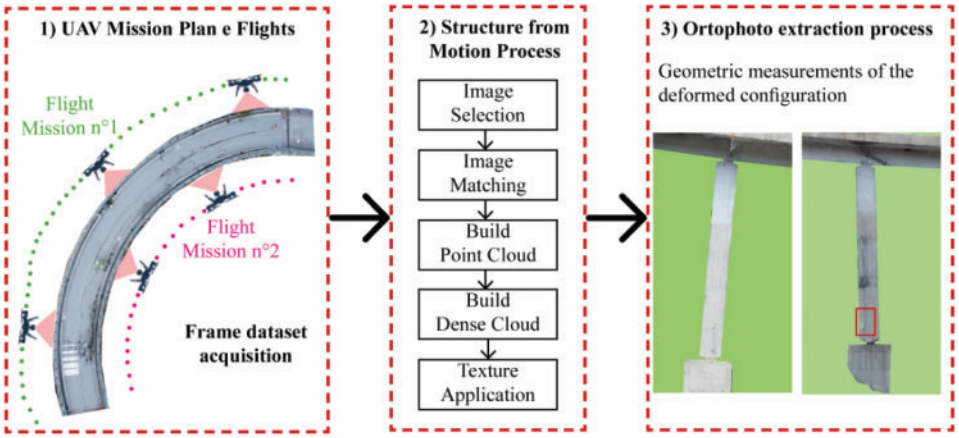

Figure 3. Conceptual flowchart describing the main steps of the geometric survey conducted on the case study bridge through UAV photogrammetry

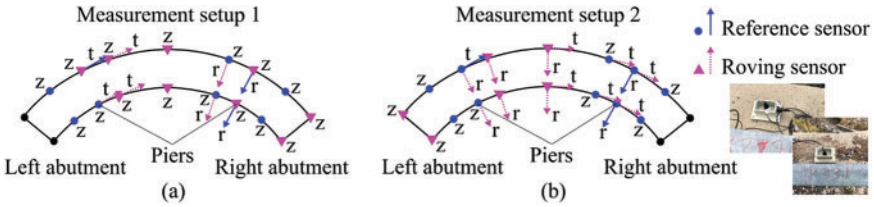

Figure 4. Measurements setups used to perform ambient vibration tests on the case study bridge

April 27th, 2022. Acceleration measurements were carried out according to the setups illustrated in Fig. 4 by using high-sensitivity (10 V/g) uniaxial seismic accelerometers, model PCB393B12, installed on stabilization steel supports positioned on the concrete curbs of the bridge deck.

A data acquisition system (DAQ), model NI cDAQ-9188, embedding four NI 9234 modules and three NI 9230 modules, was used to acquire vibration measurements with a sampling frequency of 1706 Hz. Each measurement record lasted thirty minutes, a time window quite larger than 2000 times the fundamental period of the bridge, which usually ensures an accurate estimation of the modal parameters.

The dynamic identification of the structure was carried out by using MOVA, a software for Operational Modal Analysis (OMA) recently developed by the University of Perugia.[19] The set of accelerations recorded for each measurement setup was detrended and resampled at 40 Hz, hence processed for modal feature extraction (natural frequencies, damping ratios, and mode shapes) with the Enhanced Frequency Domain Decomposition (EFDD) method. The mode shapes of the case study bridge were determined using the least squares approach to merge the shapes identified from the analysis of each measurement setup.[20]

Dynamic traveling load tests

A series of dynamic tests under traveling loads were carried out on the case study bridge to collect information about its response under service loads. The tests exploited the input provided by the passage of a vehicle of known mass and speed, while the response measurements were obtained from longitudinal strain sensors placed at the deck extrados of the bridge. The sensor setup was designed by taking advantage of the symmetry of the system; three measurement points (S1, S2, and S3) were identified at the extrados of the deck in correspondence with the right pier and the midspan sections of spans 2 and 3, as shown in Fig. 5a. The sensor typology used to measure deformations consists of a strain gauge bar installed on the bridge deck, as shown in Fig. 5b, internally equipped with four strain gauges connected according to a complete Wheatstone bridge circuit. The vehicle used to excite the bridge was a van weighing approximately 2000 kg. Given the conditions of the bridge, it was decided not to opt for heavier vehicles. The vehicle traveled at a constant speed of 30 km/h from Span 1 to Span 3 and vice versa; the travel was repeated twice [see Fig. 5c].

Numerical Models of the Case Study Bridge

This section presents the numerical models used to evaluate the actual structural response of the case study bridge and to provide a preliminary estimate of its residual life.

Simulation of the design structural configuration

A first numerical model was defined to simulate the design structural configuration of the case study bridge. The Finite Element (FE) model, shown in Fig. 6a, was built in SAP2000[21] by using eight-node solid elements to discretize the geometry retrieved from the available design reports. Cylindrical hinge restraints were applied on the right-hand side of the model's deck end to simulate the connection with

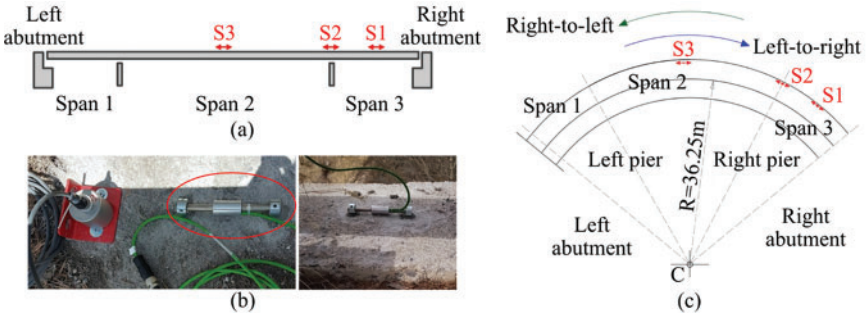

Figure 5. Dynamic traveling load tests: (a) measurements setup; (b) pictures of strain gauge bars installed on the bridge deck; (c) schematic representation of the vehicle travel directions

Figure 6. Numerical model of the case study bridge: (a) global view; (b) details of piers modeling

Table 2. Design mechanical properties assigned to the numerical model of the case study bridge: f_{ck} is the characteristic compressive strength of concrete, E is its elastic modulus, v indicates the Poisson's coefficient, and ρ is the density

Structural element	f_{ck} [MPa]	E [MPa]	v	ρ [kg/m^3]
Deck	32	33346	0.2	2499
Piers	28	32308	0.2	2499

the abutment. In contrast, two multidirectional and two one-directional restraints were placed on the outer and middle ends of the left side of the model, respectively, to replicate the connection with the other deck abutment. To reproduce the pendulum behavior of the piers, cylindrical hinge restraints were applied at the basement of both model's piers, while triangular elements with vertex nodes joined to the deck nodes were modeled at their top section [see Fig. 6b]. This modeling strategy allows relative rotations between the deck and the pillars of the model, yet not relative translations. Table 2 collects the design mechanical properties, taken from the original technical reports, used to specialize the linear elastic response of the numerical model.

Simulation of the actual structural configuration

A second numerical model was defined in SAP2000 to reproduce the actual structural configuration of the case study bridge. The model's geometry was defined by using the outcomes from the UAV photogrammetry campaign, while its mechanical properties were initially set equal to those of the model described in the previous section. The detachment of the bearing supports, observed at the left abutment of the bridge by performing visual inspections and UAV photogrammetry, was simulated by positioning the bearing supports of the model towards the inside of the deck curvature. At the right abutment, the deck of the model was constrained along the three main directions to reproduce the actual deck-abutment interaction. To represent the partial detachment observed at the base and top of the left pier due to its transverse rotation, restraints were removed at the detached part of the base of the left pier, hence triangular solid elements, connecting the top of the pier with the model's deck, were removed at the detached part of the top of the left pier. No modifications were made to the position of the restraint systems on the right-hand pillar of the numerical model. Lastly, all the restraints of the numerical model were replaced with link elements connecting the model to the ground. The stiffness of these connections was appropriately calibrated to replicate the dynamic behavior of the structure observed from field measurements as closely as possible. In this regard, the elastic moduli of the model were also involved in the fine-tuning. The calibration procedure consisted of estimating the modal properties of the numerical model representing the actual structural configuration of the bridge through numerical simulations and comparing them with the experimental modal features. The analysis focused on the first three identified modes of vibration. Experimental and numerical vibration frequencies were tested in terms of relative variations, while the Modal Assurance Criterion (MAC) was adopted to evaluate the consistency between experimental and numerical mode shapes.[22] A comparison in terms of vibration frequencies was also carried out between the numerical model representing the design structural configuration of the bridge and that representing the actual structural configuration. This latter analysis made it possible to assess the changes that occurred in the dynamic response of the structure due to the landslide-structure interaction compared to the initial design.

Simulation of the collapse mechanisms

Numerical simulations were carried out to assess the structural performance of the case study bridge under the evolution of the landslide phenomenon. Considering the direction of the mountain landslide [see Fig. 7a], known from past monitoring activities, increasing displacements simulating the movement of the ground were applied to the left pier and abutment of the numerical model representing

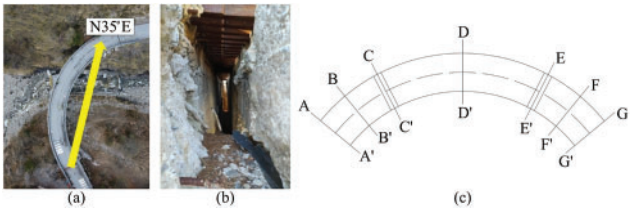

Figure 7. Numerical simulation of the landslide evolution: (a) landslide direction; (b) gap between the back wall of the left abutment and the deck of the case study bridge; (c) bridge sections verified under unsymmetrical bending

the actual structural configuration of the bridge to investigate the potential collapse mechanisms. The growth rate of the landslide was assumed to be constant over time. A first set of increasing displacements, whose maximum entity was equal to 300 mm, was applied to the left pier of the model. This is because the left abutment of the bridge can move towards the deck for about 300 mm before making contact with this structural part; this distance represents the gap between the back wall of the left abutment and the deck, as shown in Fig. 7b. A second set of increasing displacements was then applied to the left abutment of the numerical model, thus simulating the evolution of the landslide with the left abutment in contact with the deck. In this circumstance, the internal stress state of the model's deck increased at every increment in the applied displacements. The structural assessment of the bridge was carried out by considering the fundamental combination of dead and live loads at the Ultimate Limit States (ULS) established by Eurocode 0,[23] hence by assuming a confidence factor equal to 1.35 for materials' strengths according to Eurocode 8[24] (i.e., a limited knowledge level was considered for the structure under investigation to analyze the worst-case scenario). Unsymmetrical bending verifications of the deck at ULS were carried out at the sections illustrated in Fig. 7c. Thus, the maximum admissible displacement of the left abutment, corresponding to the crisis of the first section of the bridge among those tested, was determined.

Results

This section outlines the results obtained from the experimental investigations carried out on the case study bridge and the outcomes from the numerical simulations performed.

InSAR data analysis

The PSP analysis performed on the two image datasets allowed the detection of a certain number of measurement points on the deck of the case study bridge and the neighboring ground. The obtained ascending and descending velocity maps are shown in Fig. 8. In the plots, the PSs are color-coded based on their mean velocity in the monitored period. Focusing on the time histories of the PSs identified on the deck. It is highlighted that the portion of the bridge on the side of the left abutment is affected by an evident accumulation of irreversible deformations in the four-year time window covered by the satellite acquisitions, for both ascending and descending analyses. In particular, in ascending geometry, the PSs exhibit time series with a negative trend, while the PSs identified in descending geometry are characterized by a positive trend. Since the provided measurements are the projections of the real displacement vectors along the LOS in the considered viewing geometry, the opposite sign of the LOS displacement trends in ascending and descending geometries conceivably indicates that the actual movement of the deck has a prevailing horizontal component with respect to the vertical one. The permanent deformations detected through InSAR monitoring on the structure can therefore be related to the effects of the slow progression of the landslide in the period 2018–2021. In addition, the post-processing of SAR data (described in detail in Farneti et al.[25]) highlighted a rate of about 43.8 mm/year, characterizing the deformation phenomenon affecting the left abutment of the bridge.

Given the insights from the InSAR data analysis performed, the case study bridge was classified as a potentially critical asset affected by slow deformation phenomena. According to the methodology proposed in this work, on-site visual inspections were carried out on the structure to evaluate its health state and the entity of the interfering landslide.

Defectiveness of the bridge

On-site visual inspections were carried out on the case study bridge to assess its structural defectiveness once the outcomes from InSAR screening highlighted that the bridge was affected by permanent deformations due to slow deformation phenomena. As a result of the bridge-landslide interaction, the deck of the bridge was found stuck in the right abutment following the failure of the fixed bearing supports, as shown in Fig. 9a. Furthermore, the sliding supports at the left abutment were damaged and detached from the deck of the bridge [Fig. 9b]. The left pier was tilted in both its vertical and transversal plane because of the sliding of its foundation. These rotations caused a partial detachment between the deck and the upper part of the pier. A partial detachment was also noted at the interface between the pier and its foundation, as depicted in Fig. 9c. The right pier was also rotated in both its vertical and transversal plane due to the sliding of the deck towards the right abutment. Based on the described defectiveness, the actual structural configuration of the bridge is far from the design configuration, and therefore classifiable as critical. In compliance with the proposed methodology, the model-based SHM approach was chosen to assess the structural performance of the asset.

Geometrical surveys

The UAV photogrammetry campaign carried out on the case study bridge resulted in a point cloud consisting of about 2.6×10^7 points, created from a dataset of 167 images. Fig. 10a shows the textured 3D model of the bridge obtained from the further processing of the point cloud. In contrast,

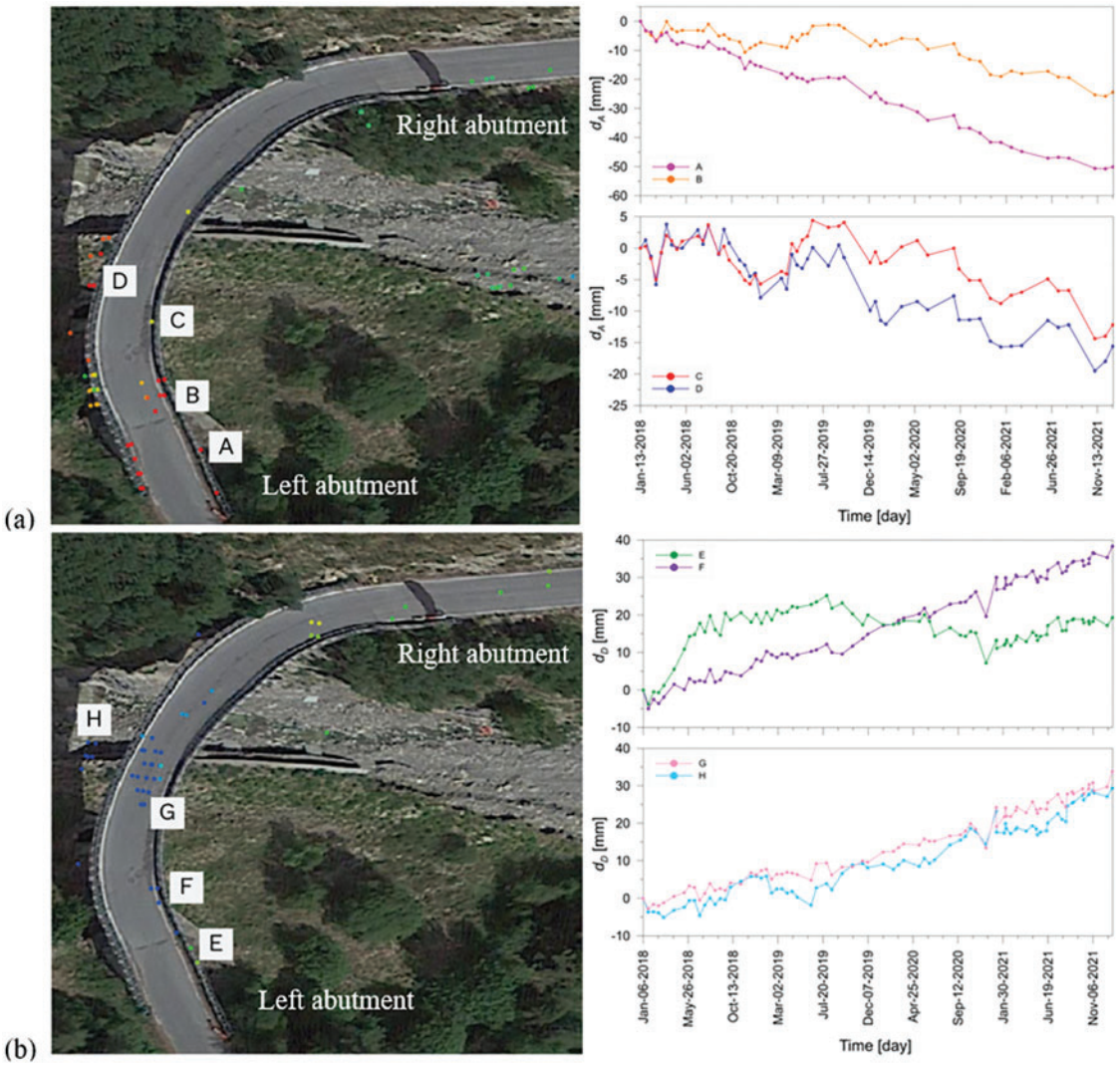

Figure 8. PSs detected in (a) ascending and (b) descending geometry on the bridge deck; the time series of four PSs are shown in both geometries, two identified close to the left abutment and two on a portion of the deck above the left pier (positive values indicate movements towards the satellite's antenna)

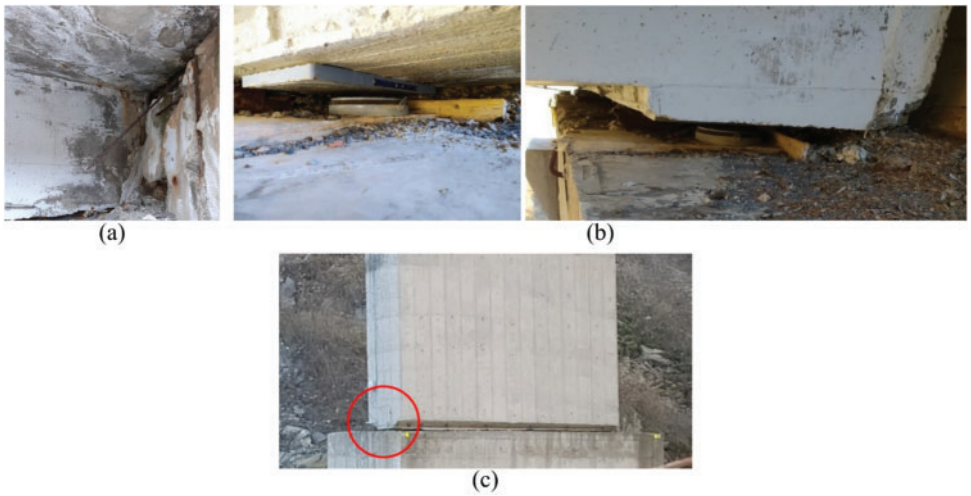

Figure 9. Defectiveness of the case study bridge: (a) detail of the bridge deck-right abutment interlock; (b) pictures of the detachment of the bearing supports at the left abutment; (c) partial detachment at the interface between the left pier and its foundation

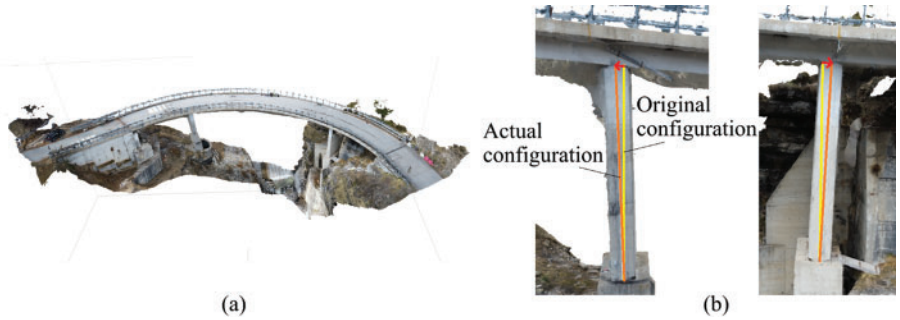

Figure 10. Results from the UAV photogrammetry campaign: (a) textured 3D model of the case study bridge; (b) actual inclination of the piers with respect to their original vertical axis

Fig. 10b details the actual structural configuration of the piers of the bridge. The processing of the orthophotos of the left pier highlighted an inclination of its vertical axis of about 3.6° with respect to its original configuration, with a maximum horizontal displacement at the top of the pier of 37 cm towards the left abutment. Similarly, the vertical axis of the right pier was tilted by about 2.2° with respect to its original configuration, with a maximum horizontal displacement at the top of the pier of 32 cm towards the right abutment.

Table 3. Relative variations between the natural frequencies determined experimentally and those obtained from the numerical models representing the design structural configuration and the actual configuration of the case study bridge

Mode of vibration	f_{exp} [Hz]	$f_{initial\ model}$ [Hz]	Variation [%]	$f_{calibrated\ model}$ [Hz]	Variation [%]
1	2.3732	2.2989	+3.13	2.3246	+2.05
2	5.8600	–	–	5.8674	−0.13
3	6.5049	6.4269	+1.20	6.5159	0.17

Experimental and numerical characterization of the dynamic behavior of the bridge

Natural frequencies and mode shapes characterizing the dynamic behavior of the case study bridge are depicted in Fig. 11. The identified mode shapes point out unexpected torsional movements of the bridge deck at the left abutment and pier. These anomalous movements of the structure indicate the occurrence of modifications at the bearing supports with respect to the initial design, whose origin can be attributed to the effects of the landslide of the mountainside. Table 3 reports the relative variations between the natural frequencies of the bridge and those obtained from the numerical simulation of its design structural configuration and actual structural configuration. It is interesting to note that the numerical model representing the design structural configuration did not simulate the second mode of vibration of the structure. This is because the second mode of vibration characterizes the dynamic response of the bridge following the modifications induced by the landslide to the structural configuration of the left pier. On the other hand, once properly calibrated, the numerical model simulating the actual structural response of the structure was able to replicate the natural frequencies corresponding to the first three modes of vibration observed experimentally. In this last model, to improve the match with the natural frequencies experimentally determined, an elastic modulus equal to 39000 MPa and 37000 MPa was set to specialize the mechanical response of the concrete of the deck and piers, respectively.

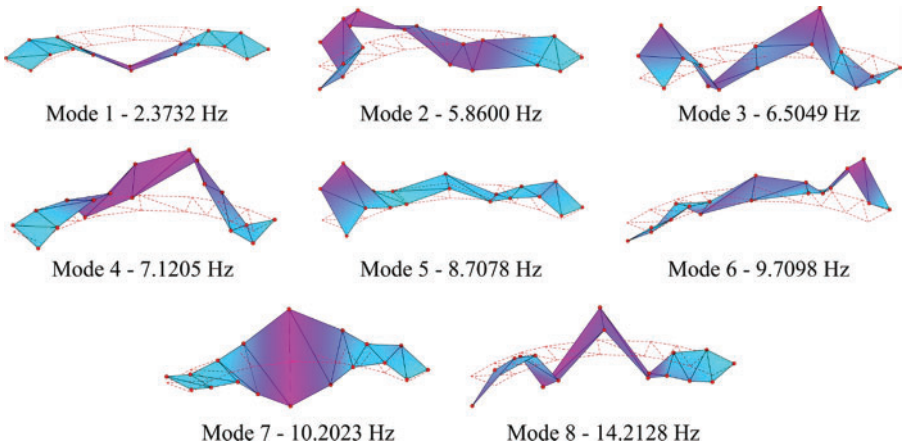

Figure 11. Natural frequencies and mode shapes of the case study bridge

Table 4. MAC matrix expressing the consistency between experimental and numerical mode shapes

Experimental mode of vibration	Numerical mode of vibration		
	1	2	3
1	0.98	1.4E−3	8.2E−4
2	2.4E−6	0.84	0.12
3	1.1E−4	3.3E−4	0.46

Figure 12. Mode shapes and natural frequencies obtained from the numerical model simulating the actual structural response of the bridge

Table 4 reports the values of the MAC computed by comparing the experimental mode shapes of the first three vibration modes with those retrieved from the calibrated numerical model. The values reported in the diagonal of the MAC matrix indicate that the model consistently replicated the shapes of both the first and second modes of vibration of the bridge. Although the model effectively reproduced the frequency of the third mode of vibration, some discrepancies between the experimental and numerical shapes of this mode remained at the end of the calibration procedure, as indicated by the low value of MAC obtained from their comparison. The modal features obtained from the numerical model simulating the actual structural configuration of the bridge are shown in Fig. 12.

Results from dynamic traveling load tests

Results from dynamic traveling load tests are presented in terms of deformation time histories recorded in the traveling time interval. The charts in Fig. 13 compare the responses related to the three sensors S1, S2, and S3 (red Span 3, blue Span 2, orange right pier, respectively). The response of the bridge to the passage of the vehicle from Span 3 to Span 1 is shown in Fig. 13a, and the one from Span 1 to Span 3 in Fig. 13b. The time interval reported in the figures is equal to 12 s, of which the first 0.9 s represents the response of the bridge before the vehicle enters the bridge (i.e., the 0.9 s before the positioning of the front axle of the vehicle on the abutment expansion joint), the next approximately 9.0 s characterize the bridge response when the vehicle is actually traveling on it; the tails of the signals (about 2.0 s long) represent free vibration response of the bridge after the passage of the vehicle. Focusing on the chart in Fig. 13a, it can be seen how the sensor S1 (Span 3—red curve) exhibits its maximum negative deflection after 2.0 s, i.e., in the time instant at which the vehicle is in the middle of Span 3; the maximum positive deflection of Span 3 is observed when the vehicle crosses the middle section of Span 2, i.e., approximately around 5.5 s; finally, when the vehicle approaches the middle section of Span 1, it is again observed a negative deflection of Span 3 (around 8.5 s) but of notably reduced magnitude. The time history of strains from sensor S3 (Span 2—blue curve) attains its maximum (negative) in correspondence of 5.5 s (i.e., when the vehicle crosses the section at which sensor S3 was placed); two symmetric positive deflection peaks can be observed at 2.0 and 8.5 s, corresponding to the passage of the vehicle on the midspan of Span 3 and Span 1, respectively. The interpretation of the time history of strains recorded from sensor S2 (right pier—orange curve), unlike the previous two, is less straightforward, and it is the result of the boundary conditions modification produced by the landslide of the mountainside (e.g., bearing supports with imperfect contact; partial support of the piers due to detachment at the bottom interface with foundation structure). Similar comments can be made for the results shown in Fig. 13b, related to the vehicle motion from the left to the right abutment.

The dynamic response of the bridge subjected to vehicle passages was numerically simulated by exploiting a simplified FE model in which the bridge deck and piers were represented by elastic shell elements, thus significantly reducing the computational cost of the analyses compared to the solid-element models previously described. However, the geometry of the simplified model was based on the performed geometric surveys, ensuring that it reflected the actual structural configuration of the case study bridge, as well as its response, was properly refined by considering the outcomes from modal identification. A comprehensive

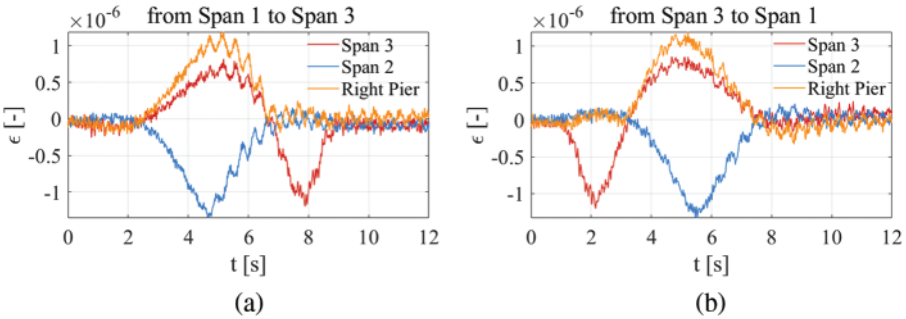

Figure 13. Comparison of the deformation time histories recorded by the sensors (placed at the midspan extrados of Spans 2 and 3 and at the top of the right pier) during the passage of the vehicle: (a) from Span 3 to Span 1; (b) from Span 1 to Span 3

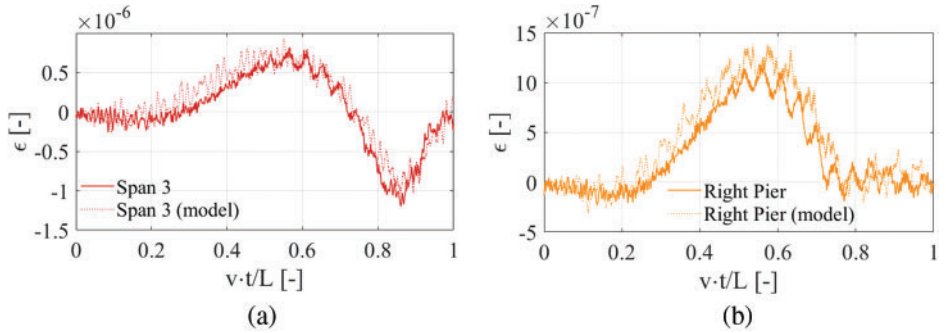

Figure 14. Comparison of the deformation time histories recorded by the sensors and simulated through the calibrated numerical model

description of the simplified FE model and the adopted calibration procedure can be found in Celati et al.[26]. It is worth noting that, despite the model's materials being elastic, a nonlinear dynamic time-history analysis was performed to catch the nonlinearity of the boundary conditions (i.e., gap elements were used to simulate the imperfect contacts between structural parts). In Fig. 14, a comparison is provided between the deformation time histories recorded by the sensors installed on the bridge deck and those numerically simulated through the simplified FE model. In the plots, the abscissa has been normalized to eliminate the influence of the imperfect match between numerical and experimental traveling times. Despite the complexity of the case study and related boundary conditions, the agreement between numerical and experimental results appears satisfactory, thus testifying to a quite high degree of reliability of the model. Furthermore, this is also witness to the fact that the bridge deck, under the investigated dynamic loads, remains in the linear elastic field of behavior.

Overall, the results from the dynamic traveling load tests confirmed the presence of structural critical issues highlighted by both visual inspections and other experimental campaigns (e.g., OMA). Moreover, the present application represents a preliminary test of the capability of damage detection strategies based on strain measures under moving vehicles, which revealed that it is suitable to explore potential anomalous responses of bridges due to multiple causes (landslide in this specific case).

Prediction of the residual life of the structure

Fig. 15 shows the deformed configuration of the numerical model of the case study bridge obtained by simulating the evolution of the mountain landslide over time. The first set of displacements applied to the left pier of the numerical model induced a translation of 300 mm of the base of the left pier along the direction of the mountainside landslide. As the pier was hinged at both ends, the simulated ground movements did not produce any increase in stress within the deck of the structure. The second set of displacements, applied to the left abutment of the model, was increased up to 50 mm when the collapse condition was reached at section E—E′ of the model's deck. The maximum admissible displacement of the left abutment of the bridge, resulting from the numerical simulation of the landslide phenomenon, was therefore equal to 350 mm.

Figure 15. A deformed configuration of the numerical model of the case study bridge, obtained by simulating the evolution of the mountain landslide with the indicated section of the deck triggering the collapse condition

Considering the growth rate of about 43.8 mm/year characterizing the deformation phenomenon affecting the left abutment of the bridge (determined via InSAR-based monitoring as reported in the previous sections of the paper), and assuming this value to be constant over time, the maximum admissible displacement of the left abutment thus determined via numerical simulations can be reached in approximately 8 years, which is the provisional estimate of the residual life of the structure. It is worth mentioning that several assumptions were made in the computations of the residual life of the case study bridge (e.g., this concern, among others, material properties, modeling strategies, and evolution of the landslide). The influence of each of them in the calculations will be carefully evaluated in future studies, so refinement of the estimate of the residual life of the bridge can be expected.

Conclusions

The paper has proposed a new methodology for the diagnosis and monitoring of bridges and viaducts under the effects of slow deformation phenomena, such as those induced by mountain landslides. InSAR observations play a central role in the approach as they are used both for the remote identification and monitoring of bridges affected by this pathology. Landslides can cause various structural diseases to bridges and viaducts, leading them to collapse in the worst-case scenarios. It follows that the early identification of assets experiencing landslides and their continuous monitoring are

tasks of crucial importance to ensure the safety of road networks.

The methodology initially employs SAR screening methods to remotely scan large geographical areas and identify bridges on which satellite-monitored points show irreversible accumulations of deformation in their displacement trends. Visual inspections are carried out on the detected structures to assess the entity of the deformation phenomena, their interaction with the assets, structural defects, and potential collapse mechanisms. The methodology proposes the adoption of a data-driven or model-based SHM approach for the continuous monitoring of the identified bridges based on the results of visual inspections. Bridges evaluated in a sound health state, characterized by a non-critical interaction with the landslide, can be subjected to continuous InSAR monitoring. In this scenario, thresholds can be defined to trigger alarms caused by anomalies in the trends of the displacements monitored via satellites. Moreover, InSAR observations can be further processed to evaluate potential changes in the structural response of the asset induced by the landslide over time. Bridges experiencing critical structural conditions can instead be monitored in a continuous fashion by combining the analysis of InSAR observations with the outcomes from numerical simulations. Numerical models mimicking the actual structural response of the selected bridges can be defined and used to carry out collapse simulations to estimate the residual life of the structures. The insights obtained from the critical analysis of the numerical outcomes can then be employed to validate/integrate the results obtained via InSAR monitoring and vice versa; such an approach aims at achieving comprehensive structural performance evaluations of the bridges under investigation. With this purpose, field tests can also be carried out on the assets to improve the knowledge of their structural behavior and, therefore, the accuracy of the numerical simulations.

The paper has also presented a case study of a curved road bridge affected by a mountain landslide to provide a practical application of the proposed methodology. The approach leading to the remote identification of the bridge and its slow deformation phenomenon based on InSAR observations has been illustrated. Given the outcomes from the visual inspections carried out on the asset, the model-based SHM approach included in the proposed methodology has been selected to monitor the bridge over time. Collapse simulations have been carried out with a numerical model tuned according to the evidence of several field tests performed on the bridge. Then, the synergic use of InSAR observations and outcomes from numerical simulations permitted the obtainment of a provisional estimate of the residual life of the structure.

Overall, the paper addressed the need for systematic methodologies to account for InSAR data in the diagnosis and monitoring of bridges affected by slow deformation phenomena. Given its large-scale applicability, the proposed methodology can suit the needs of managing authorities dealing with inventories of bridges spread over large geographical areas. As the proposed approach is based on the processing of SAR observations for the remote detection/monitoring of bridges under slow deformation phenomena, the reader can easily understand that the main limitations of the methodology lie in the availability of PSs, with reference to their location and numerosity within a specific area and/or relative to a specific bridge asset, as well as in the temporal length of the SAR measurement series, when available.

Recommendations for future work

The influence of the assumptions made in the residual life calculation of the case study bridge should be systematically evaluated in future studies to refine the estimate found in this work and, no less importantly, to consciously drive structural performance assessments and numerical modeling of future assets affected by slow deformation phenomena. The establishment of monitoring thresholds from InSAR data should be also investigated extensively.

Acknowledgments

This work was financially supported by FABRE—Research Consortium for the evaluation and monitoring of bridges, viaducts, and other structures through funds for basic research on "Multi-level safety analysis and monitoring of existing bridges." The authors gratefully acknowledge funding from the Italian Ministry of University and Research through the PRIN Project "TIMING"—Time evolution laws for IMproving the structural reliability evaluation of existING post-tensioned concrete deck bridges" (protocol no. P20223Y947). The authors would also like to acknowledge the contribution of the e-Geos group for providing the SAR data used in this study. The authors from the University of Perugia also acknowledge funding by the European Union—NextGenerationEU under the Italian Ministry of University and Research (MUR) National Innovation Ecosystem grant ECS00000041—VITALITY. Finally, the authors from the University of Camerino acknowledge the cofounding received from the European Union—FSE, Pon Research, and Innovation 519 2014–2020, for what concerns the research activity carried out within the research project "Synergistic use of innovative sensors and new data analysis procedures for the safety of infrastructures."

Disclaimer

The authors declare no conflict of interest.

Supplemental Materials

Data reported and discussed in this work are available upon request.

References

[1] Zanini MA, Faleschini F, Pellegrino C. Bridge residual service-life prediction through Bayesian visual inspection and

data updating. *Struct Infrastruct Eng*. 2017 Jul 3;13(7):906–917. doi:10.1080/15732479.2016.1225311

[2] Nettis A, Saponaro M, Nanna M. RPAS-based framework for simplified seismic risk assessment of Italian RC-bridges. *Buildings*. 2020 Aug 28;10(9):150. doi:10.3390/buildings10090150

[3] Meoni A, García-Macías E, Venanzi I, et al. A procedure for bridge visual inspections prioritisation in the context of preliminary risk assessment with limited information. *Struct Infrastruct Eng*. 2023 May 3;2:1–27. doi:10.1080/15732479.2023.2210547

[4] Casas JR, Cruz PJ. Fiber optic sensors for bridge monitoring. *J Bridge Eng*. 2003 Nov;8(6):362–373. doi:10.1061/(ASCE)1084-0702(2003)8:6(362)

[5] Kim S, Kim T. Machine-learning-based prediction of vortex-induced vibration in long-span bridges using limited information. *Eng Struct*. 2022;266(4):114551. doi:10.1016/j.engstruct.2022.114551

[6] Anastasopoulos D, De Roeck G, Reynders EPB. One-year operational modal analysis of a steel bridge from high-resolution macrostrain monitoring: influence of temperature vs. retrofitting. *Mech Syst Signal Process*. 2021;161(9):107951. doi:10.1016/j.ymssp.2021.107951

[7] Scozzese F, Dall'Asta A. Nonlinear response characterization of post-tensioned RC bridges through Hilbert-Huang transform analysis. *Struct Control Health Monit*. 2024 Feb 23;2024. doi:10.1155/2024/5960162

[8] Milillo P, Giardina G, DeJong MJ, et al. Multi-temporal InSAR structural damage assessment: The London crossrail case study. *Remote Sens*. 2018 Feb 13;10(2):287. doi:10.3390/rs10020287

[9] Zhu M, Wan X, Fei B, et al. Detection of building and infrastructure instabilities by automatic spatiotemporal analysis of satellite SAR interferometry measurements. *Remote Sens*. 2018;10:1816. doi:10.3390/rs10111816

[10] Cavalagli N, Kita A, Falco S, et al. Satellite radar interferometry and in-situ measurements for static monitoring of historical monuments: the case of Gubbio, Italy. *Remote Sens Environ*. 2019;235:111453. doi:10.1016/j.rse.2019.111453

[11] Mele A, Miano A, Di Martire D, et al. Potential of remote sensing data to support the seismic safety assessment of reinforced concrete buildings affected by slow-moving landslides. *Arch Civ Mech Eng*. 2022;22:492. doi:10.1007/s43452-022-00407-7

[12] Giordano PF, Turksezer ZI, Previtali M, et al. Damage detection on a historic iron bridge using satellite DInSAR data. *Struct Heal Monit*. 2022;21:2291–2311. doi:10.1177/14759217211054350

[13] Qin X, Ding X, Liao M, et al. A bridge-tailored multi-temporal DInSAR approach for remote exploration of deformation characteristics and mechanisms of complexly structured bridges. *ISPRS J Photogramm Remote Sens*. 2019;156:27–50. doi:10.1016/j.isprsjprs.2019.08.003

[14] Schlögl M, Widhalm B, Avian M. Comprehensive time-series analysis of bridge deformation using differential satellite radar interferometry based on Sentinel-1. *ISPRS J Photogramm Remote Sens*. 2021;172:132–146. doi:10.1016/j.isprsjprs.2020.12.001

[15] Farneti E, Cavalagli N, Costantini M, et al. A method for structural monitoring of multispan bridges using satellite InSAR data with uncertainty quantification and its pre-collapse application to the Albiano-Magra Bridge in Italy. *Struct Heal Monit*. 2022;0:1–19. doi:10.1177/14759217221083609

[16] Nettis A, Massimi V, Nutricato R, et al. Satellite-based interferometry for monitoring structural deformations of bridge portfolios. *Autom Constr*. 2023 Mar 1;147(46):104707. doi:10.1016/j.autcon.2022.104707

[17] Tonelli D, Caspani VF, Valentini A, et al. Interpretation of bridge health monitoring data from satellite InSAR technology. *Remote Sens*. 2023;15(21):5242. doi:10.3390/rs15215242

[18] Costantini M, Falco S, Malvarosa F, et al. Persistent scatterer pair interferometry: approach and application to COSMO-SkyMed SAR data. *IEEE J Sel Top Appl Earth Obs Remote Sens*. 2014 Jul;7(7):2869–2879. doi:10.1109/JSTARS.2014.2343915

[19] García-Macías E, Ubertini F. MOVA/MOSS: two integrated software solutions for comprehensive structural health monitoring of structures. *Mech Syst Signal Process*. 2020 Sep 1;143:106830. doi:10.1016/j.ymssp.2020.106830

[20] Au SK. Assembling mode shapes by least squares. *Mech Syst Signal Process*. 2011 Jan 1;25(1):163–179. doi:10.1016/j.ymssp.2010.08.002

[21] Wilson EL, Habibullah A. *SAP2000 User's Manual*. Berkeley, Calif: Computers and Structures, Inc.; 2003.

[22] Pastor M, Binda M, Harčarik T. Modal assurance criterion. *Proc Eng*. 2012 Jan 1;48:543–548. doi:10.1016/j.proeng.2012.09.551

[23] Standard B. Eurocode—Basis of structural design. Eurocode 0. 2002 Jul 27.

[24] Pinto PE, Franchin P. Eurocode 8-Part 3: assessment and retrofitting of buildings. *Proc Eurocode*. 2011 Mar 17;8:10–11.

[25] Farneti E, Meoni A, Natali A, et al. Structural health monitoring of curved roadway bridges through satellite radar interferometry and collapse simulation. *ce/papers*. 2023;6:907–916. doi:10.1002/cepa.2201

[26] Celati S, Castellani M, Cavalagli N, et al. Operational modal analysis as a tool for bridge model updating. Application to an unconventional case study. In: *International Conference on Experimental Vibration Analysis for Civil Engineering Structures*; 2023 Aug 2; Cham: Springer Nature Switzerland, pp. 1–10. doi:10.1007/978-3-031-39109-5_1

BER the international journal of bridge engineering management and research

Seismic Resilience Assessment for Steel-Concrete Composite Bridges Including Impacts of Near-Fault Earthquakes

Yang Liu[1]; Da-Gang Lu[2]; Fabrizio Paolacci[3]; Gianluca Quinci[3,*]; and Sourabh Vern[3]

Submitted: 18 January 2024 **Accepted:** 03 June 2024 **Publication date:** 03 September 2024

DOI: 10.70465/ber.v1i1.5

Abstract: This paper proposes a seismic resilience assessment method for steel-concrete composite bridges (SCCB) considering near-fault earthquake hazards. Based on conventional probabilistic seismic hazard disaggregation analysis, a correction factor is defined to represent the proportion of the occurrence probability of the near-fault pulse-like, near-fault non-pulse-like and far-field earthquake conditioned on a given intensity level concerning the total occurrence probability of all earthquakes. The parameters of functionality recovery functions are modified using the factor proposed, and then the restoration processes after each type of earthquake are estimated. Correspondingly, vulnerabilities of a typical SCCB under near-fault and far-field earthquakes are developed as a case study. Based on the seismic hazard and fragility results, the seismic risk for each type of earthquake in a 50-year horizon is estimated. After that, the modified functionality recovery function is derived from the expected functionality. To implement the proposed method, the expected seismic resilience indices of a typical SCCB involved in the SEQBRI project are estimated, and the seismic resilience assessment is conducted. The seismic resilience assessment without considering earthquake type is also conducted for comparison analysis using the same bridge. The result shows that the seismic resilience of bridges in near-fault earthquake scenarios can be analyzed by the method proposed, and reducing the structural vulnerability under low-intensity level earthquakes and improving the structural recovery efficiency for slight and moderate damage states are more meaningful to enhance the seismic resilience of bridges.

Author keywords: Seismic resilience; occurrence probability; steel-concrete composite bridges; near-fault earthquakes assessment

Introduction

The concept of seismic resilience has been recently employed to explore the post-earthquake behavior of civil and industrial infrastructure conditions in terms of recovery cost and time.[1,2] In general, seismic resilience is defined as the ability of a system to mitigate hazards, contain the effects of natural disasters, and carry out recovery activities in such a way as to minimize social disruption and reduce the impact of future earthquakes.[3] While seismic risk is strictly related to the capacity and robustness of a construction against earthquake, seismic resilience is instead associated with post-earthquake recovery conditions that typically include direct and indirect economic losses.[3,4] In this respect, the uncertainties related to the seismic vulnerability and the recovery phase suggest the use of a probabilistic approach for the resilience estimation.[1,3,5,6]

The fundamental framework of probabilistic resilience assessment proposed by several authors is illustrated in Fig. 1.[3, 7] In particular, the conventional seismic risk analysis under the framework of Performance-based Earthquake Engineering (PBEE) is the basis of the risk assessment methodology. It includes a) probabilistic seismic hazard analysis, b) seismic fragility analysis, and c) loss and robustness estimation. The formulation of a Probabilistic Seismic Resilience Analysis (PSRA) methodology required the introduction of concepts like recovery estimation and resilience assessment.[2,8,9]

This approach has been largely applied in the literature for the quantitative resilience assessment of bridges under seismic loading. Most of these works were mainly focused on the effects of the seismic vulnerability of structural components[10,11] or the recovery functions[12,13] on the bridge resilience.es Moreover, several novel methodologies were proposed to quantify the seismic resilience of a bridge by using reliability concepts and fuzzy mathematics.[14,15] Furthermore, the assessment of time-dependent resilience of a

*Corresponding Author. Gianluca Quinci.
Email: gianluca.quinci@uniroma3.it
[1]College of Civil Engineering & Architecture, Wenzhou University, Wenzhou 325035, P.R. China
[2]School of Civil Engineering, Harbin Institute of Technology, Harbin 150090, P.R. China
[3]Department of Civil, Computer Science and Aeronautical Technologies Engineering, Roma Tre University, Rome 00146, Italy

Discussion period open till six months from the publication date. Please submit separate discussion for each individual paper. This paper is a part of the Vol. 1 of the International Journal of Bridge Engineering, Management and Research (© BER), ISSN 3065-0569.

bridge[16,17] and the resilience assessment of transportation have also been developed by Reed et al.[18] and Ouyang et al.,[19] which was also supported by monitoring of the resilience framework by Quinci et al.[20].

Nonetheless, the seismic resilience of bridges located in the near-fault region has not been sufficiently investigated, even though near-fault earthquakes can generate severe damages,[21,22] (Alavi et al. (2001), Billah et al. (2013)). Consequently, in the present paper, a refined approach for assessing the seismic resilience of bridges in near-fault regions is proposed, which is strongly based on a PSRA approach. The following issues have been analyzed: 1) Probabilistic seismic hazard disaggregation analysis considers the difference between near-fault and far-field earthquake hazards. Besides, the respective hazard of near-fault pulse-like and non-pulse-like earthquakes is computed using a proportionality coefficient derived from the PSHA analysis through the velocity pulse method,[23] (Baker (2007)), 2) the pulse-like and non-pulse-like ground motions records are identified for the fragility analysis, 3) the empirical functionality recovery functions are modified to include the impact of near-fault earthquakes. 4) Based on these steps, a revised formula of expected seismic functionality is provided for the probabilistic seismic resilience assessment.

Thus, the purpose of this study is twofold: 1) to introduce a refined assessment method of seismic resilience of bridges in near-fault regions, and 2) to evaluate the importance of considering near-fault earthquakes in resilience assessment. To this end, firstly, a brief review of the current approach for the resilience assessment of bridges that do not include near-fault effects is offered in Section 2, whereas the proposed method is described in Section 3. Then, as an illustrative example, the seismic resilience of a new type of steel-concrete bridge is investigated in Section 4 using the proposed method. Furthermore, the same example is used to compare near-fault and far-field conditions in the resilience assessment.

Probabilistic seismic resilience assessment methods

Classical approach

The general definition of resilience is the following[3,5,7,18,24]:

$$R = \frac{\int_{t_0}^{t_0+T_T} Q(t)dt}{T_T} \tag{1}$$

where R is the resilience; $Q(t)$ is the functionality recovery function depending on time t; t_0 is the occurrence time of the earthquake; T_T is the full functionality recovery time interval, which is derived as the summation of the idle time interval T_I and the recovery time interval T_R. T_I and T_R are two recovery parameters that directly affect resilience. The residual functionality Q_r at time t_0 and the target functionality Q_t are other important recovery parameters. An illustration of resilience and recovery parameters is offered in Fig. 2.

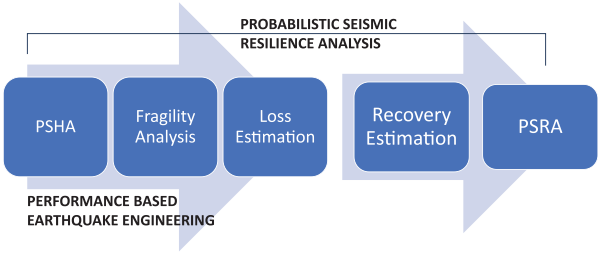

Figure 1. The fundamental framework of seismic resilience assessment

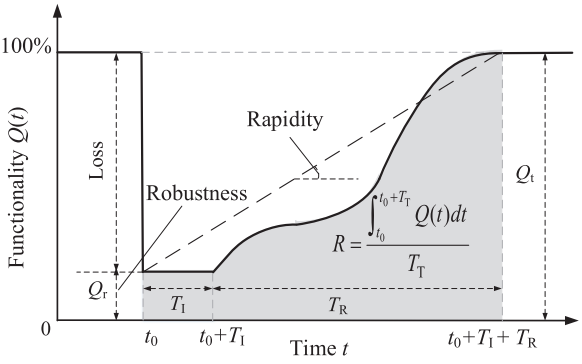

Figure 2. Fundamental concepts of seismic resilience

Rapidity and robustness are the two key properties of resilience.[5] Rapidity is defined as the slope of the functionality curve during the recovery time t. Given its time-varying nature, an average recovery rate is preferred, which is denoted as RA, as shown in Fig. 2, whose definition is the following[7]:

$$RA = \frac{Q_t - Q_r}{T_T} \tag{2}$$

Robustness, here denoted as RO, is the ratio between the residual functionality at the time t_0 and the full functionality (shown in Fig. 2).

The fundamental framework for predicting the seismic resilience of a bridge, as shown in Fig. 1, comprises five main stages.[25] The loss estimation is beyond the scope of this paper and will not be treated. The other four stages, probabilistic seismic hazard analysis (PSHA), seismic fragility analysis (SFA), recovery estimation, and probabilistic seismic resilience analysis (PSRA), are herein briefly introduced. The outcome of the PSHA is the probability of occurrence of a seismic event with intensity IM=i at the site where the bridge is located.[26] It is herein denoted as P_H (IM = i).

In the fragility analysis of the bridge, the damage is classified into different states (i.e., slight, moderate, extensive, and complete), and the vulnerability is represented by the probability of the bridge being in the specific damage states (DSs) at each level of IM is quantified. Using the index j to distinguish the different DSs, the vulnerability can be expressed as P_V(DS = j | IM = i) .

The recovery function estimation can be carried out according to the statistics on specific bridge rehabilitation procedures after earthquakes. The functionality associated with the serviceability condition is usually expressed as a

normalized value (*e.g.*, 100% of the traffic capacity with no earthquake occurrence or the goal for a completed recovery). The mostly used functionality recover function has been proposed in Cimellaro et al.,[7] and it is expressed by Eq. (3):

$$Q(t) = 1 - L(t) = Q_{\mathrm{r}} + H(t) \cdot f_{\mathrm{r}}(t) \tag{3}$$

where $L(t)$ measures the loss of functionality at time t; Q_{r} is the residual functionality at time t_0; $H(t)$ is the Heaviside step function; $f_{\mathrm{r}}\ (t)$ is the recovery function at time t. In recent contributions, several typical simplified recovery functions have been proposed, such as the trigonometric model in Chang and Shinozuka,[27] the exponential model in Kafali and Grigoriu,[28] the linear model in Bruneau and Reinhorn,[6] Cimellaro et al.[5] and Ouyang et al.[19]. Bocchini et al.[24] proposed a comprehensive recovery function containing the four recovery parameters presented in Fig. 2. This function will be adopted here by synthesizing these three recovery functions.

The recovery procedure is usually divided into several phases, which can be expressed by the Heaviside step function, $H(t)$.[7] The main parameters of the $H(t)$, the idle and the recovery time interval, can be obtained through the statistical analysis approach based on functionality evaluation data.[1] The residual functionality Q_r can be assessed by a complete damage investigation and the corresponding loss analysis. For the end condition of the recovery procedure, the target functionality Q_t can be decided by administrators or be equal to 100% for a convenient assumption.

In this study, the functionality recovery function for different *DS*s is denoted as $Q_j(t)$, where j refers to the j-th damage state. Note that, for each $Q_j(t)$, there is a corresponding idle time interval T_{I}, recovery time interval T_{R}, residual functionality Q_{r}, and target functionality Q_{t}.

To quantify the seismic resilience in the last PSRA stage of the method, the expected functionality $\bar{Q}(t)$ can be obtained by using the following expression[11]:

$$\bar{Q}(t) = \sum_{i=1}^{n_{IM}} P_H(IM = i) \sum_{j=1}^{n_{DS}} P_V(DS = j \,|IM = i\,) Q_j(t) \tag{4}$$

where $P_H(IM = i)$, $P_F(DS = j|IM = i)$ and $Q_j(t)$ are the hazard, fragility curve and functionality recovery function, respectively. By substituting Eq. (4) in Eq. (1), the seismic resilience of the bridge can be quantified.

Proposal of a method for the resilience assessment of bridges in near-fault conditions

For bridges in near-fault regions, which may suffer more serious seismic damages,[22] an improved approach to assess the probabilistic seismic resilience is herein presented. This approach allows us to distinguish the effects of near-fault and far-field earthquakes based on their probability of occurrence. Moreover, two types of the near-fault ground motions (pulse-like and non-pulse-like ground motions) are further distinguished. Accordingly, the fundamental framework of Fig. 1 can be re-thought as illustrated in Fig. 3.

(1) Probabilistic Seismic Hazard Analysis (PSHA). The aim of this part is to acquire the occurrence probability of the near-fault pulse-like (NFPL), near-fault non-pulse-like (NFNP), and far-field (FF) earthquakes for each level of IM. A convenient method to obtain the probability of occurrence of specific seismic events using the existing data of probabilistic seismic hazard disaggregation (PSHD) is proposed. Firstly, the P_{H} $(IM{=}i)$ can be calculated using the classic seismic hazard curves. Then, the occurrence probability of the three types of earthquakes for each level of IM can be evaluated by using the following equation in which the parameter s is a proportion factor.

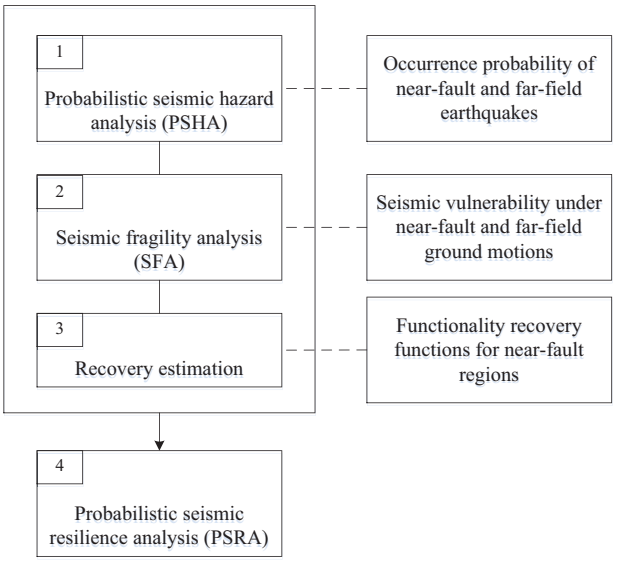

Figure 3. Flowchart of the PSRA in near-fault regions

$$P_{\mathrm{S}}\,(ST = k\,|IM = i\,) = s\,(ST = k\,|IM = i\,) \cdot P_H\,(IM = i) \tag{5}$$

where ST is the abbreviation for seismic event type; k can assume the values 1,2 or 3 if the seismic event is of type NFPL, NFNP, and FF, respectively; $s(ST{=}k|IM{=}i)$ is a factor obtained by PSHD, which indicates the proportion of the occurrence probability of the specific type of earthquake conditioned on the intensity i with respect to the total occurrence probability of all earthquakes $P_{\mathrm{H}}(IM{=}i)$.

The conventional PSHD provides the contribution of all possible sources to the probability of exceeding each intensity measure IM,[29,30] as shown in Fig. 4, where the classical deaggreation plot is illustrated.[30] The total contribution of near-fault sources to the seismic hazard can be calculated by summing the contributions satisfying the condition that the closest distance of the site from the fault (Rcd) is lower than or equal to 20 km.[22,31]

Similarly, the contribution of far-field sources can be obtained. With this approach, the ratio of specific seismic hazard (NF or FF) to the total one is obtained. By transforming the probability of exceedance to the occurrence probability, the percentage of NF and FF seismic events for the selected intensity IM$=i$ can be calculated, which are herein indicated as $s_{\mathrm{N}}(IM{=}i)$ and $s_{\mathrm{F}}(IM{=}i)$, respectively. For example, s_{F} means $s(ST{=}3|IM{=}i)$.

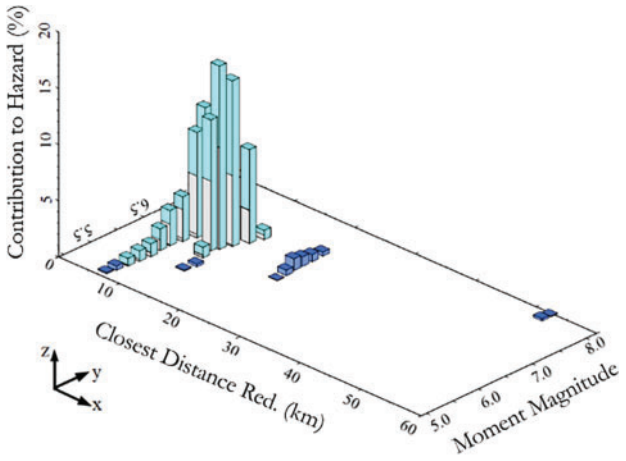

Figure 4. Example of the probabilistic seismic hazard disaggregation[32]

The proportion factor $s(ST{=}k|IM{=}i)$ for NFPL and NFNP is calculated as,

$$s\left(ST=k\,|IM=i\right)=\alpha_k\left(IM=i\right)\cdot s_{\mathrm{N}}\left(IM=i\right)\quad k=1,2 \tag{6}$$

where $\alpha_k(IM{=}i)$ indicates the percentage of the total probability that a near-fault source generates pulse-like ($k{=}1$) or non-pulse-like ($k{=}2$) seismic events conditioned to $IM{=}i$. Referring to the PSHD approach presented in Shahi et al.,[31] the values of the $\alpha_k(IM{=}i)$ could be determined by statistics to historical seismic records at a specific source.

(2) Seismic Fragility Analysis (SFA). In this step, the vulnerability function, here denoted as $\mathrm{P_V(DS = j \mid IM = i)}$, need to be refined accounting for the specific type of ground motion ($ST{=}1,2,3$) earthquakes, that is $P_{\mathrm{V},\ ST=k}\left(DS=j\,|IM=i\right)$. To separate the pulse-like and non-pulse-like ground motions, the quantitative identification method for velocity pulse is here adopted.[23,33] This latter is based on the idea of adopting a simplified numerical model of the real ground motion calibrated through the least-square fitting (LSF) technique. Subsequently, an energy index (Ep) is defined and calculated to identify the pulse-like ones among the selected natural earthquake records. According to Zhai et al.,[33] the ground motions can be considered pulse-like when the value of Ep is greater than 0.3.

(3) Recovery estimation. In this stage, the functionality recovery function for each damage state $Q_j(t)$ is differentiated by near-fault and far-field earthquakes. Even though the probability distribution of the parameters in $Q_j(t)$ is generally unknown, the data of the real procedure of bridge functionality restoration can be gathered and used to provide empirical values of the recovery parameters, including minimum, moderate, and maximum values.[1] Given that, for a given IM, the seismic damage states of the bridge under near-fault ground motions usually differ from those caused by far-field ground motions,[22] the recovery curves corresponding to different damage states are different. So, it is reasonable to assume that the recovery function parameters' values correlate to the hazard of NF and FF earthquakes. To be more specific, the smaller residual functionality (Q_{r}), the longer idle time (T_{I}), and the recovery time (T_{R}) should be used to account for the impact of NF ground motions. Hence, by using the percentage of the NF and FF earthquakes, the modified moderate values of the parameter in $Q_j(t)$ for each damage state and for each IM are assumed as follows:

$$V_{\mathrm{r,m}}\left(DS=j\,|IM=i\right)=\frac{s_{\mathrm{N}}\left(IM=i\right)\cdot V_{\mathrm{r,max}}\left(DS=j\right)+s_{\mathrm{F}}\left(IM=i\right)\cdot V_{\mathrm{r,min}}\left(DS=j\right)}{s_{\mathrm{N}}\left(IM=i\right)+s_{\mathrm{F}}\left(IM=i\right)} \tag{7}$$

where $V_{\mathrm{r,m}}(DS=j|IM=i)$ represents the modified moderate values of recovery parameters for $DS{=}j$ conditioned on $IM{=}i$, $V_{\mathrm{r,max}}(DS{=}j)$ and $V_{\mathrm{r,min}}(DS{=}j)$ represent the maximum and minimum values of the recovery parameters. The weight of the maximal and minimal values to the modified values are the percentage of NF and FF earthquakes, $s_{\mathrm{N}}(IM{=}i)$ and $s_{\mathrm{F}}(IM=i)$.

It is worth noting that the most severe damage to bridges may be induced by the NF earthquake event rather than the FF earthquake; hence, the most adverse values of recovery parameters (for example, the longest recovery time and the minimal residual functionality) in the functionality recovery function should result from the NF condition.[22,33] Consequently, for the parameter Q_{r}, $V_{\mathrm{r,max}}(DS{=}j)$ should be assumed as the minimal absolute value, whereas $V_{\mathrm{r,min}}(DS{=}j)$ is the maximum absolute one. On the contrary, for the parameters T_{I} and T_{R}, $V_{\mathrm{r,max}}(DS{=}j)$ should assume the maximum absolute value and the $V_{\mathrm{r,min}}$ as the absolute minimum one.

(4) Probabilistic Seismic Resilience Analysis (PSRA). After the three previous stages, the expected functionality level $\bar{Q}(t)$ in Eq. (5) can be rewritten as:

$$\bar{Q}_{RE}(t)=\sum_{i=1}^{n_{IM}}\sum_{k=1}^{n_{ST}}P_S(\ ST=k|\ IM=i)\ \sum_{j=1}^{n_{DS}}P_{V,ST=k}(DS=j\,|IM=i\,)Q_{DS=j||IM=i}\,(\mathrm{t}) \tag{8}$$

where $P_{\mathrm{S}}(ST=k|\,IM=i)$, $P_{\mathrm{V},ST=k}(DS=j\,|IM=i)$, and $Q_{DS=j|ST=k}\,(t)$ are those obtained from the previous stages. Then, the assessment of the bridge resilience in a near-fault region is completed by substituting $\bar{Q}_{\mathrm{RE}}(t)$ into Eq. (1). In addition, the robustness and rapidity of the refined expected resilience can be calculated following the method presented in section 2.1.

Illustrative example

Description of the numerical model

Short-medium span steel-concrete composite bridges made of hot-rolled beams and concrete cross beams are very common in non-seismic areas due to the economic benefits of limiting manufacturing and short construction time. To extend this favorable structural solution to high seismic-prone areas, and therefore, cover the relevant lack of

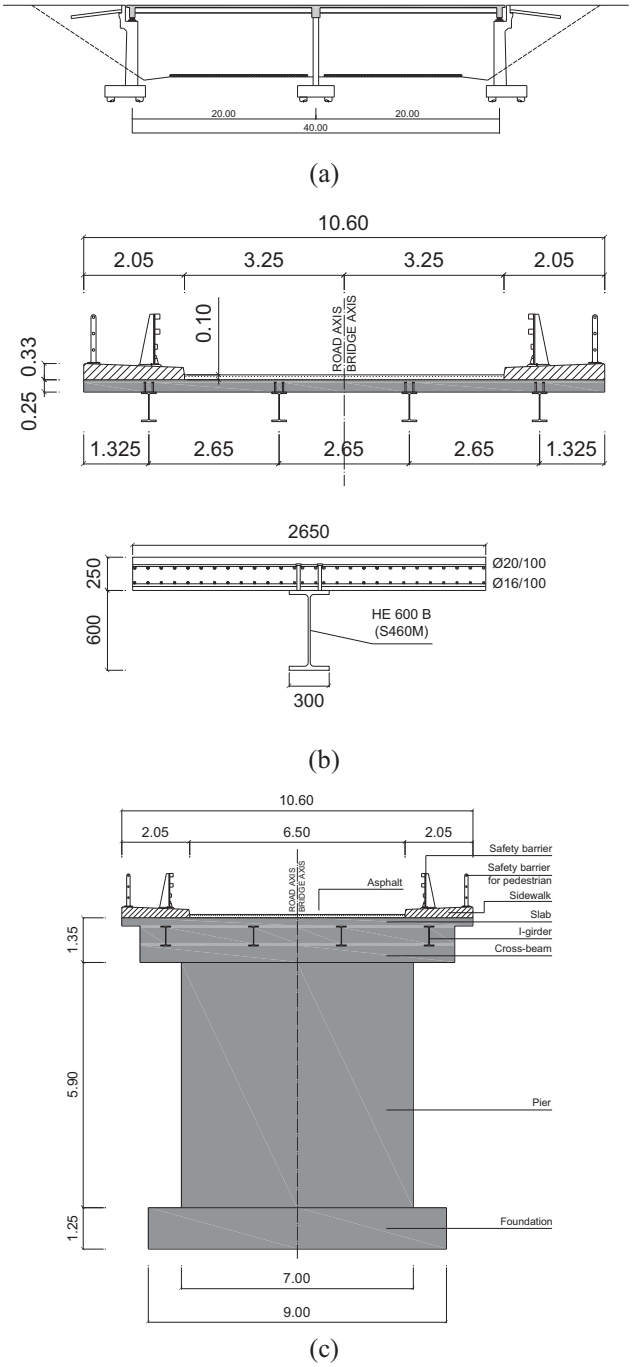

Figure 5. Illustrative example: (a) frontal view bridge; (b) Deck composite concrete-steel girder, (c) Wall Pier

knowledge on the seismic response of these types of bridges, a wide research activity has been carried out within the European Project SEQBRI.[34] In this respect, a two-span concrete-steel composite road overpass can be applied, or the proposed resilience assessment methodology can be applied.

The analyzed bridge is a typical highway overpass designed according to Eurocodes.[35] It is characterized by two spans of 20.00 m, a total width of the road cross-section equal to 10.60 m, with a carriageway 6.50 m wide and two sidewalks 2.05 m wide, as shown in Fig. 5. The concrete slab is 0.25 m thick, and it is supported by four main I-girders HLB 600 sections made with hot-rolled S460 steel, with 2.65 m in-between distance. The deck-to-pier connection is of monolithic type because of the presence of Concrete Cross Beams (CCB) with sections 60 ×90, as shown in Fig. 5. The CCBs are designed according to Chabrolin et al.[36]. At the abutments, the steel girders are connected to the CCB, which is 0.60 m wide, and the deck is simply supported on normal damping rubber bearings. At the intermediate pier, a monolithic pier-to-deck connection is adopted in which the pier is fixed to a reinforced CCB 0.90 m wide (Fig. 4). The connection between steel girders and abutments and between steel girders and intermediate pier is guaranteed by 0.60 m and 0.90 m wide reinforced CCB, respectively. The pier height is 7.00 m, with a 0.60x7.00 m transversal section, and a deep foundation for the piers is chosen. To minimize the construction phases of the steel-concrete composite deck, a procedure based on one-step pouring has been adopted. The foundation soil is assumed to be categorized as type B according to CEN[37] and the soil structure interaction effect is neglected.

The 3D finite element (FE) model has been developed using the collaborative framework OpenSees.[38] This model uses force-based nonlinear beam elements with fiber cross-sections to model the single steel girder and the tributary concrete slab. The Menegotto–Pinto model[39] is adopted to simulate the mechanical behavior of steel girders and slab reinforcement, while the Kent-Park[40] model is used to reproduce the mechanical behavior of concrete. Nonlinear links with elastoplastic behavior are used to model the shear studs connecting the steel girders to the slab, within the CCB, and along the deck.

Fig. 6 shows the details of the 2-D FE model for the concrete crossbeam. Rigid links are used to model the vertical head plate, which is welded on the steel girders and directly in contact with the transverse concrete beam. Different nonlinear links modeling the behavior of the horizontal shear-headed studs within the joint are connected to these rigid links according to the CCB configuration.

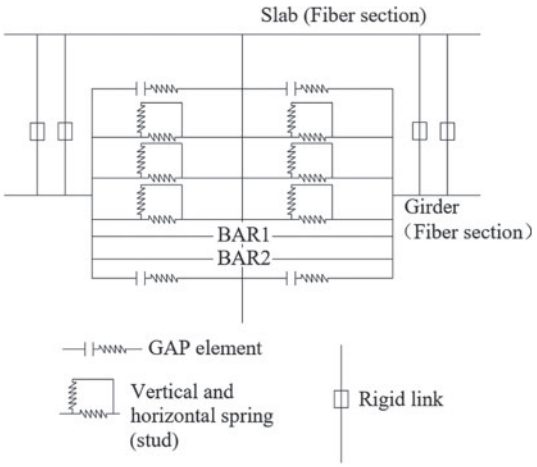

Figure 6. 2-D FE model of the beam-to-pier connections

To simulate the constraint in compression due to the presence of the CCB, gap elements are adopted at both the left and right sides of the CCB joint at two different heights,

as shown in Fig. 6. A simplified procedure for evaluating the stiffness of the gap elements is performed, if the compression force transferred by the girder will exert uniformly on the contact area of the vertical head plate. Two groups of the prestressing bars at the bottom area of the CCB are modeled by two elastic truss elements. More details can be found in Liu et al.[41].

The strength of the shear studs has been evaluated in accordance with CEN,[42] while the stiffness has been evaluated using the load-slip curves experimentally defined by Gattesco and Giuriani.[43] The behavior of the CCB joint is difficult to reproduce. A component-based model proposed by Paolacci et al.[34] has been adopted to represent the behavior of the CCB. Details of the novel type of pier-to-deck connections can be found in Abbiati et al.,[44] which is beyond the scope of this study.

Probability of occurrence of earthquakes in near-fault regions

According to the performance-based earthquake engineering approach, the use of Intensity Measures (IMs) that enable consistent hazard conditions and exhibit a strong correlation with the selected quantity of interest has been extensively debated in the literature. The most accepted procedure is based on selecting a global IM that can be used to scale the selected records to exceed difference limit states. The suitability of a selected IM depends on the nature of the dynamic problem.[45,46] Frequently used IMs are generally scalar and often identified with the peak ground acceleration (PGA) or the spectral acceleration at a given vibration period ($S(T)$) of the structure. This latter has often been demonstrated to be superior with respect to PGA,[47,48] and hence will be employed in this paper for the seismic resilience assessment. In the following, it will be simply indicated as S_a.

For the probabilistic seismic hazard disaggregation analysis, the Interactive disaggregation tool[30] has been adopted to achieve the factors ($ST = k$) at the given location of bridges and the site condition. The bridge is assumed to be ideally located in the city of Livermore in California (USA), with a northern latitude of 37.682° a western longitude of 121.768°, which is a recognized near-fault seismic region according to the Interactive Fault Map available in the U.S. Geological Hazard Science Center.[49] The seismic design conditions belong to the NEHRP site class B/C boundary, with an average shear–wave velocity in the top 30 meters m/s.[50] ($V_s{}^{30}$) of 760 m/s.[50]

The contributions of seismic hazard associated with the exceedance probability of 1%, 2%, 5%, 10%, 20%, and 50% in 50 years have been calculated, and the corresponding Sa are respectively equal to 0.94g, 0.78g, 0.58g, 0.45g, 0.33g, and 0.19g. Subsequently, the ratios $S_N(IM{=}i)$ and $S_F(IM{=}i)$ can be obtained by using the site-to-source distance of 20 km to categorize the source type into far-field (FF) and near-fault (NF).

As described in Section 2, a near-fault pulse-like (NFPL) source is characterized by the presence of velocity pulses in the velocity time history of ground motions. The recommended values of $\alpha_k(IM{=}i)$ in Eq. (6), i.e., the proportion factor for NFPL, are respectively 65%, 70%, 75%, 80%, 85%, and 90%, which corresponds to the level of IM from small to large.[51,52] Fig. 7 shows the proportion of FF, NFNP, and NFPL sources with respect to the total source contributions.

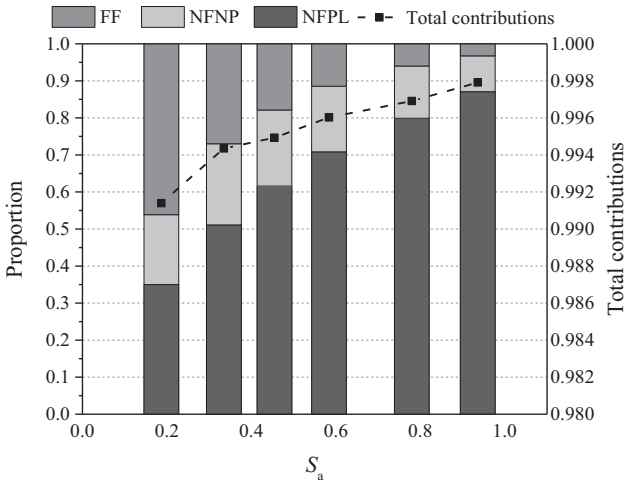

Figure 7. Proportion of FF, NFPL, and NFNP ground motions[53]

It can be noted that the proportion of NF sources increases from 55% to 97% as the IM level increases. This is why separately considering the occurrence probability of near-fault earthquakes can reduce the errors for resilience assessment. Because the mean hazard for several ground-motion prediction equations is adopted in the PSHD, the total contribution at each level of IM is not 100%, as shown in Fig.7. The value of the total contribution is always greater than 99%, which basically satisfies the analysis needs in this study.

The hazard curves of the site, for a reference life of 50 years, have been provided by the United States Geological Survey (2017). The probability of occurrence of seismic events with a given intensity IM, $P_H(IM{=}i)$, are determined and used in Eq. (5) along with the value of $s(ST{=}k|IM{=}i)$ shown in Fig. 7. Finally, the probability of occurrence $P_S\,(ST = k\,|IM = i)$ of NFPL, NFNP, and FF earthquakes is computed.

Selection of ground motions

For the fragility analysis of the bridge, a suite of ground motions representative of NF and FF ground motions have been selected using the PEER strong ground motion database of NGA-West2.[54] When selecting NF ground motions, the following hazard conditions are considered: moment magnitudes (MW) greater than 6.0 and site-to-source distances (R) less than 20 km., and the NF earthquakes with the ratio of peak ground velocity (PGV) and peak ground acceleration (PGA) being greater than 0.2.[55,56,33,57] The FF ground motion records were selected to match the PGA and M_W of the NF records but with R > 20 km. To satisfy the assumption of NEHRP site class B/C and the assumption of $V_s{}^{30}$ value in the 537-1150 m/s range for more optional ground motion records.

Due to the limited number of NFNP ground motion records, only eight ground motion records were selected. Hence, the number of the ground motion records for NFPL and FF is eight, considering the record-to-record variability.[26,58] All selected ground motions were recorded during the following eight strong earthquake events: San Fernando earthquake (USA, 1971), Nahanni earthquake (Canada, 1985), Loma Prieta Earthquake (America, 1989), Manjil Earthquake (Iran, 1990), Northridge Earthquake (America, 1994), Chi-Chi Earthquake (Taiwan, 1999), Kocaeli Earthquake (Turkey, 1999), Lwate Earthquake (Japan, 2008).

It has been recognized that the velocity pulse included in the velocity time history of the ground motion is the most important feature of the NFPL ground motion.[31] For a certain pulse-like ground motion, its biggest velocity pulse is generated along the strike parallel direction and the strike normal direction. Therefore, the strike parallel and normal components of the selected pulse-like ground motion are used for fragility analysis. Using the wavelet method,[23,51,59] identified the pulse-like ground motions and calculated the two components of these pulse-like ground motions, which are provided in the PEER database.

The ground motions selected for this study are listed in Table 1, where R represents the site-to-source distance, M_{W} represents the moment magnitude, PGA represents the peak ground acceleration, and S_a (T_1,5%) represents the spectral acceleration at the first period with a 5% damping ratio.

Seismic fragility analysis

If the seismic demand (D) and capacity (C) follow a log-normal distribution, the fragility represented by the failure probability can be expressed in the following form Cornell et al.[26]:

$$P(D \geq C \,|IM) = \Phi\left[\frac{\ln(m_{D|IM}) - \ln(m_C)}{\sqrt{\beta_{D|IM}^2 + \beta_C^2}}\right] \tag{9}$$

where $m_{D|IM}$ and $\beta_{D|IM}$ are, respectively, the median and dispersion of the demand obtained numerically through time-history analysis; m_C and β_C are the median and the dispersion of the capacity obtainable through numerical

Table 1. The selection of ground motion records

Ground motion	Event No.	NGA No.	Station, component	R (km)	M_{W}	PGA (g)	S_a (T_1,5%) (g)
NFPL	1	763	Gilroy - Gavilan Coll, strike parallel	9.96	6.93	0.35	0.21
	2		Gilroy - Gavilan Coll, strike normal			0.33	0.32
	3	1161	Gebze, strike parallel	10.92	7.51	0.26	0.17
	4		Gebze, strike normal			0.14	0.24
	5	1511	TCU076, strike parallel	2.74	7.62	0.34	0.72
	6		TCU076, strike normal			0.43	0.37
	7	1529	TCU102, strike parallel	1.49	7.62	0.30	0.45
	8		TCU102, strike normal			0.17	0.84
NFNP	9	495	Site 1, 010	9.6	6.76	1.10	0.46
	10		Site 1, 280			1.19	0.73
	11	496	Site 2, 240	4.93	6.76	0.51	0.29
	12		Site 2, 330			0.36	0.50
	13	1517	TCU084, EW	11.48	7.62	1.01	2.30
	14		TCU084, NS			0.43	1.14
	15	1521	TCU089, EW	9	7.62	0.35	0.49
	16		TCU089, NS			0.23	0.37
FF	17	72	Lake Hughes #4	25.07	6.61	0.18	0.36
	18	989	LA - Chalon Rd	20.45	6.69	0.20	0.70
	19	1234	CHY086	28.42	7.62	0.17	0.40
	20	1485	TCU045	26	7.62	0.49	0.31
	21	87	Santa Anita Dam	30.7	6.61	0.19	0.14
	22	1633	Abbar	40.4	7.37	0.52	1.00
	23	5659	IWTH27	43.59	6.9	0.27	0.12
	24	5680	MYGH04	40.43	6.9	0.20	0.08

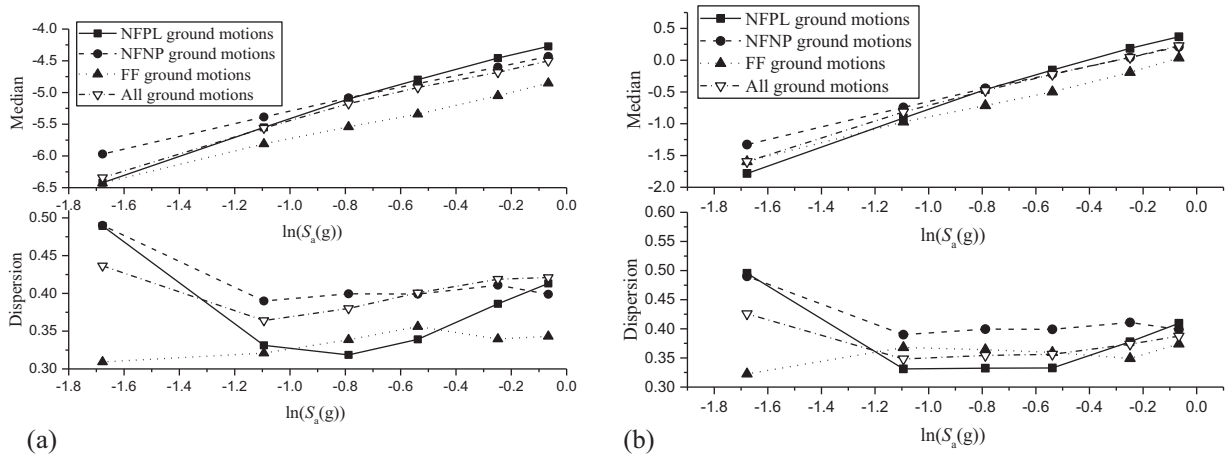

Figure 8. Medians and dispersions of demand: (a) pier drift ratio, (b) pier curvature ductility

analysis (i.e., push-over analysis) or experimental investigations; $\Phi(\bullet)$ is the standard normal cumulative distribution function. This study considers the record-to-record variability associated with the seismic action in the probabilistic seismic demand analysis (PSDA). Moreover, the uncertainties associated with the structural response and the capacity are considered in the probabilistic seismic capacity analysis (PSCA).

Accordingly, the PSDA of the bridge is performed through Multiple Stripe Analysis (MSA) by Tothong et al.[60]. The levels of IM are selected based on PSHD results presented in Section 3.2. The ground motions are then modified by scaling the values of S_a to match the selected IM. Consequently, a total of 144 nonlinear time-history analyses have been performed. The pier drift ratio (ratio of the maximum displacement of the pier top and the total height of the pier, DR) and the pier displacement ductility (ratio of the maximum displacement and the yielding displacement of the pier, δ_p) have been used as Engineering Demand Parameters (EDP). This choice derives from the preliminary analysis, which indicated that significant damage in the CCB appears only for high seismic intensity values, whereas the most significant one is located on the pier.[61] In addition, given that the selected bridge's transversal response is smaller than the longitudinal one, only this latter has been analyzed.[61]

A log-log representation of the probabilistic seismic demand model has been assumed here, as suggested by Conell et al.[26]. Accordingly, the natural logarithm of EDP depends linearly on the Ln(IM). As stated before, to reduce the dispersion $\beta_{D|IM}$,[62,63] the demand parameters ($m_{D|IM}$ and $\beta_{D|IM}$) have been obtained separately for NFPL, NFNP, and FF ground motions and only for comparison, also for the entire set of ground motions.

Fig. 8 shows the median and dispersion of demand in terms of pier drift ratio and pier curvature ductility at each level of IM. It can be easily noted that they are higher for NFPL and NFNP ground motions with respect to FF signals. It can be noticed that both mean values of pier drift and curvature at the base section are higher when near fault condition is considered, and more in particular for NFPL condition, when S_a>0.45 g (ln S_a>0.8). For lower values of S_a the NFNP condition prevails. In any case, the differences are limited.

As stated before, the pier is the most vulnerable element of the bridge, with potentially catastrophic consequences. Usually, piers experience different degrees of damage, from the cover spalling and fracture to the buckling of longitudinal reinforcement and, finally, bars fracture. These four damage levels are selected as Damage Measures (DMs) and will be associated with slight, moderate, extensive, and complete damage conditions. Damage state thresholds (limit states) for typical bridges with wall-type piers have been defined in the literature using damage analysis combined with experimental tests and numerical simulations.[64] Table 2 summarizes the mean values and the dispersions of the different limit states. Using these values, the fragility curves for slight, moderate, extensive, and complete damage have been obtained by Eq. 9, illustrated in Fig. 11, for example, in terms of pier drift ratio and displacement ductility and for slight damage and moderate damage conditions.

The graph shown in Fig. 11 represents the probability of exceedance at each level of IM for NFPL, NFNP, FF, and all ground motions. These data points are linked by straight lines for the lack of reliable data at the other seismic intensities. Note that the results of the seismic fragility for both two EDPs are too obviously different to present the

Table 2. Damage states for pier of wall type and dispersions of capacity.

	Slight damage	Moderate damage	Extensive damage	Complete damage
Drift ratio (DR)	0.36%	0.72%	1.87%	3.30%
Displacement ductility (μ_D)	1.029	2.177	4.187	8.373
Dispersion of capacity (β_C)	0.488	0.542	0.538	0.605

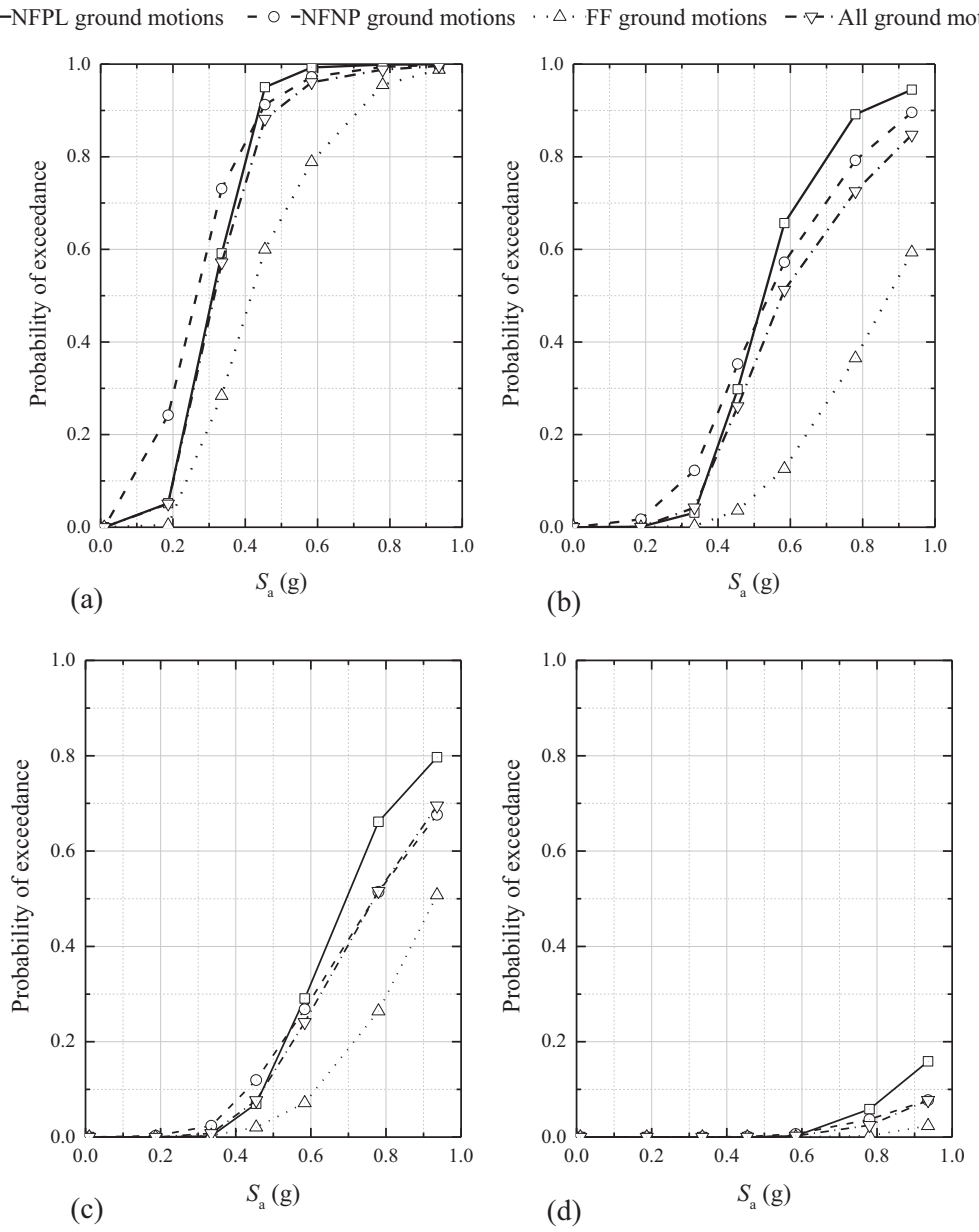

Figure 11. Component fragility curves for pier drift ratio of (a) slight damage, (b) moderate damage, and for displacement ductility of (c) slight damage, (d) moderate damage

fragility of the whole bridge; the system fragility curves combined with all components are adopted here. Based on the conservative assumption of the tandem connection between components,[63] the system fragility can be expressed as:

$$Fragility_{\text{system}} = 1 - \prod_{c=1}^{n_{\text{component}}} [1 - Fragility_c] \quad (10)$$

in which the $n_{\text{component}}$ is the number of components considered in the analysis, and c is the specific component. By applying Eq. (10), the system fragility is obtained. To be more effective in the representation of the probability, Table 3 reports the probability to be exactly in a specific damage state DS, defined as the difference between the fragilities of two sequential damage states:

$$\mathrm{P}\left(D = D_{slight}\right) = \mathrm{P}\left(D \geq D_{moderate}\right) - \mathrm{P}\left(D \geq D_{slight}\right) \quad (11)$$

For example, in Table 3 for the NFPL ground motions, when S_a=0.19g, there is only a 0.1% probability of moderate damage occurring, while there is a 5.1% probability of slight damage, and the level of damage does not continue to get larger. When S_a=0.94g, there is only a 4.6% probability that slight damage will occur and will not continue to develop. In contrast, there is a 71.2% probability that the slight damage will develop to the moderate damage state, a 22.3% probability that it will develop to a severe state, and a 1.8% probability that it will develop to a complete state. Thus, it can be understood that the total probability of damage, or the probability of all having slight damage, is about 99.9%.

In this way, it is easy to identify the conditions where a damaged state prevails. For example, the higher the Sa, the lower the probability of being exactly in a slightly damaged

Table 3. System vulnerability in different damage states.

Type of ground motions	S_a(g)	Slight damage	Moderate damage	Extensive damage	Complete damage
NFPL	0.19	0.051	0.001	0.000	0.000
	0.45	0.656	0.298	0.000	0.000
	0.94	0.046	0.712	0.223	0.018
NFNP	0.19	0.227	0.017	0.000	0.000
	0.45	0.570	0.351	0.003	0.000
	0.94	0.096	0.775	0.124	0.005
FF	0.19	0.005	0.000	0.000	0.000
	0.45	0.572	0.036	0.000	0.000
	0.94	0.391	0.598	0.006	0.000
All	0.19	0.050	0.001	0.000	0.000
	0.45	0.630	0.260	0.001	0.000
	0.94	0.140	0.751	0.103	0.005

Table 4. Empirical values of recovery parameters according to the literature[65,66,67]

Damage state	Residual functionality (%)			Idle time (months)			Recovery time (months)			A	s
	Moderate	Max	Min	Moderate	Max	Min	Moderate	Max	Min		
Light	75	100	50	1.5	2	1	2.667	5	0.333	0.0	0.5
Moderate	25	50	0	1.5	2	1	3.667	6.667	0.667	−0.1	0.5
Extensive	10	20	0	1.5	2	1	5.167	8.333	2	0.1	0.5
Complete	0	0	0	1.5	2	1	6.25	10	2.5	0.1	0.5

state condition. This probability is the highest for Sa<0.45g, but it decreases for higher Sa.

For the sake of brevity, only three seismic intensities are shown in Table 3.

Functionality recovery model

In this section, the parameters of the functionality recovery functions for the four damage states are estimated by the method presented in Section 2.2. Empirical values for the three recovery parameters of the residual functionality, idle time, and recovery time can be determined based on the evaluation of data from the real functionality recovery of bridges in California as listed in Table 4,[65,66] referred to as the same damage parameters of Table 2. The values of the shape parameters (defined as A and s) recommended by Dong et al.[17] for the recovery functions based on engineering experience are also reported in Table 4. Parameter A governs the amplitude of the sinusoidal function, and parameter s defines the flex position of the sinusoid, as defined by Bocchini et al.[24].

In addition, the target functionality is assumed to be constant and equal to 100% for each damage state. Fig. 9 shows the recovery empirical functions for the four damage states according to the values of Table 4. The curves of Fig. 9 have been obtained by applying Eq. (7). The parameters of the functionality recovery empirical functions are reported in Table 5.

Resilience estimation and discussion

According to the refined method (RM) presented in Section 2.2, the expected functionality of the bridge in 50 years can be calculated by applying Eq. (8), which includes the effects of NF earthquakes. A simplified method (SM) also estimates the functionality without distinguishing NF from FF conditions.

Fig. 10 illustrates the expected functionality of the bridge for each damage state, estimated by considering both conditions (RM and SM). It can be noted that the corresponding

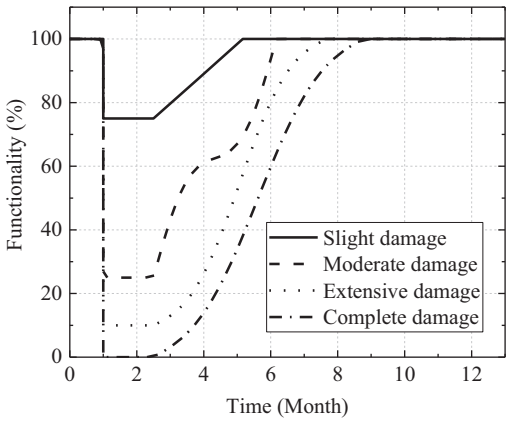

Figure 9. Empirical functionality recovery profiles

Table 5. Values of refined recovery parameters for functionality recovery empirical functions

	Damage state	S_a (g)					
		0.19	0.33	0.45	0.58	0.78	0.94
Residual functionality (%)	Slight	73	63	59	56	53	52
	Moderate	23	13	9	6	3	2
	Extensive	9	5	4	2	1	1
	Complete	0	0	0	0	0	0
Idle time (months)	–	1.5	1.7	1.8	1.9	1.9	2.0
Recovery time (months)	Slight	2.8	3.7	4.2	4.5	4.7	4.8
	Moderate	3.9	5.0	5.6	6.0	6.3	6.5
	Extensive	5.4	6.6	7.2	7.6	8.0	8.1
	Complete	6.5	8.0	8.7	9.1	9.6	9.8

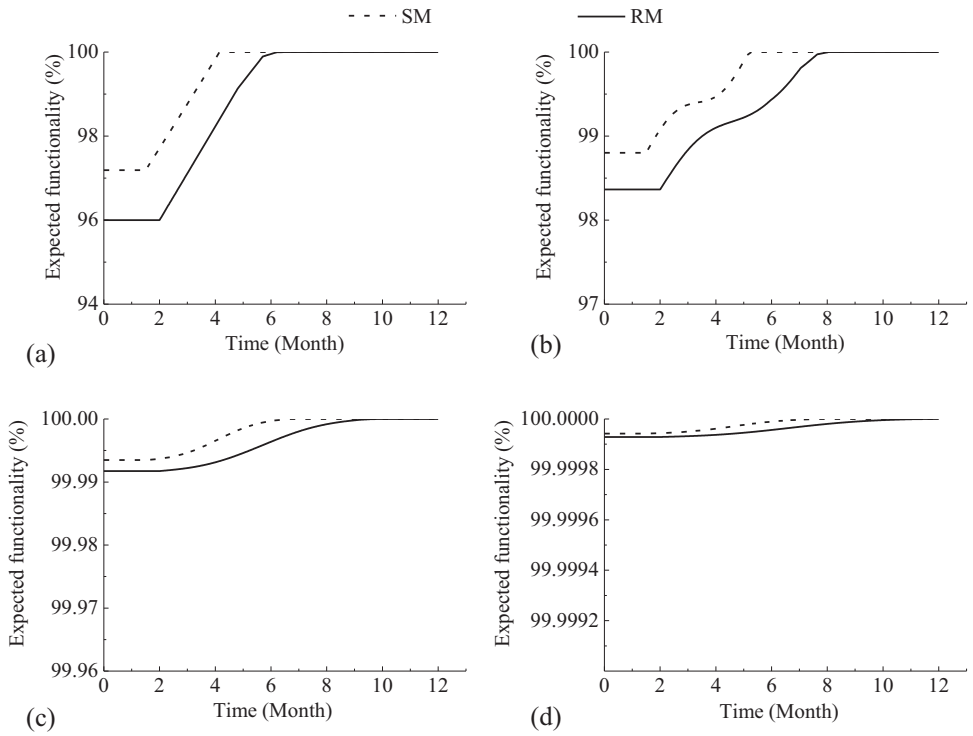

Figure 10. Expected functionality in 50 years of (a) slight damage, (b) moderate damage, (c) extensive damage, and (d) complete damage

recovery paths are different. For each damage state, the RM condition is related to a lower residual functionality and a longer recovery time. The difference is reduced in extensive and complete damage conditions, as shown in Fig. 10 (c) and (d). This results from the low probabilities associated with strong events and severe damage. For the quantitative assessment of the seismic resilience in near-fault conditions, the expected resilience index, R, is adopted here to assess seismic resilience in near-fault conditions quantitatively. Using Eq. (1), the R for each IM and damage state level is calculated using RM and SM conditions, respectively. Because, as already observed, the differences between NFPL and NFNP are limited, we omitted these two cases for brevity to distinguish in Fig. 10.

The results are listed in Table 6, in which the relative errors are also presented in brackets. Although strong earthquakes and serious damage could reduce the resilience of the bridge, in engineering practice, the low probability of a strong seismic event and the reduced vulnerabilities of extensive or complete damage states more strongly affect seismic resilience. Therefore, the expected resilience index of complete damage and that for the seismic event of 0.94g are close to 100%. Comparison analysis results of RM and SM show that the values of the estimated seismic resilience of RM are smaller than that of SM. The relative errors, computed as the difference between methods of non-distinguishing and distinguishing NF and FF events, are in the range of 0 to

Table 6. Expected resilience matrix of the bridge and relative errors for two methods.

	Expected resilience (%)							
	Slight damage		Moderate damage		Extensive damage		Complete damage	
S_a (g)	RM	SM	RM	SM	RM	SM	RM	SM
0.19	98.98	99.78(0.81)	99.66	100.00(0.41)	100	100.00(0.00)	100	100.00(0.00)
0.33	96.92	99.34(2.50)	99.42	99.82(0.40)	100	100.00(0.00)	100	100.00(0.00)
0.45	98.85	99.89(1.06)	99.26	99.71(0.46)	99.89	99.99(0.10)	100	100.00(0.00)
0.58	99.89	99.89(0.10)	99.71	99.94(0.23)	99.97	100.00(0.03)	100	100.00(0.00)
0.78	100	100.00(0.00)	99.98	100.00(0.02)	100	100.00(0.00)	100	100.00(0.00)
0.94	100	100.00(0.00)	100	100.00(0.00)	100	100.00(0.00)	100	100.00(0.00)

Table 7. Expected Resilience of the bridge and the relative errors of rapidity and robustness

*S*a (g)	Resilience (%)		Relative error of rapidity (%)	Relative error of robustness (%)
	RM	SM		
0.19	98.70	99.62(0.94)	−16.82	0.33
0.33	95.42	98.89(3.63)	−5.31	0.85
0.45	97.49	99.40(1.97)	2.17	0.46
0.58	99.43	99.87(0.44)	7.77	0.10
0.78	99.97	99.99(0.03)	4.28	0.00
0.94	100.00	100.00(0.00)	−1.76	0.00
Aggregate result (Combined all intensities)	94.01	97.77(4.00)	8.95	2.12

3%. The maximum relative error of 2.5% appears when the bridge is slightly damaged at the level of IM 0.33g.

Though the difference between the two methods presented in Table 6 is limited, the aggregated seismic resilience of all investigated damage states and all levels of IM may lead to higher relative errors. The aggregated expected resilience at each level of IM for both MR and SR conditions is listed in the second and third columns of Table 7, along with the relative error in terms of rapidity and robustness. The maximal relative error in the expected resilience is found at IM = 0.33g, equal to 3.63%. In any case, the relative errors are limited when the intensity of seismic events is larger than 0.5g. By aggregating all the levels of IM, the resilience of the bridge calculated in MR condition becomes 94.01% with an error of 4.00% with respect to SM. In terms of robustness, RM provides lower values, which indicates that the results of RM are more conservative. The relative error in rapidity is large, especially for lower IM (16,82%), even though non-regular behavior can be noticed when IM varies.

To better understand the effects of NF and FF conditions on the expected resilience, the proportion of the NF earthquakes is changed in the range -50% - +50%. This way, it is intended to locate the bridge in different NF regions. The reason for selecting variations in percentage and not in absolute values of NF and FF proportions is to investigate in a clear manner the sensitivity of the bridge resilience with respect to initial conditions derived by predefined seismic hazard conditions.

The expected resilience, rapidity, and robustness results are illustrated in Fig. 12 for the case RM. Relative errors of the results calculated from the new proportions. It is found that the maximum relative error of the expected resilience is 1.8%, while that of the rapidity and robustness are almost 15% and 2%, respectively. In the investigated range of this study, the variation tendency of the resilience decreases along with the increasing occurrence proportion of NF earthquakes. Combining the results shown in Table 7 and Fig. 12, it can be concluded that the maximum relative error for the expected resilience of RM to SM is nearly 10%, at least for the selected case study.

It should be emphasized that the recovery parameters are random variables, though the refined moderate values are used in this study. With this respect, the maximum relative errors of the expected resilience, including the uncertainties of recovery parameters, can be magnified to more than 20% based on the engineering experience and analysis result. Consequently, a larger relative error can occur in SM condition in comparison with RM, reaching the value for the case study of about 15%.

Conclusions

A refined approach for probabilistic seismic resilience assessment has been presented for bridges in near-fault regions. The impact of near-fault ground motions is considered using probabilistic seismic hazard disaggregation results. According to the selected case study, a steel-concrete composite

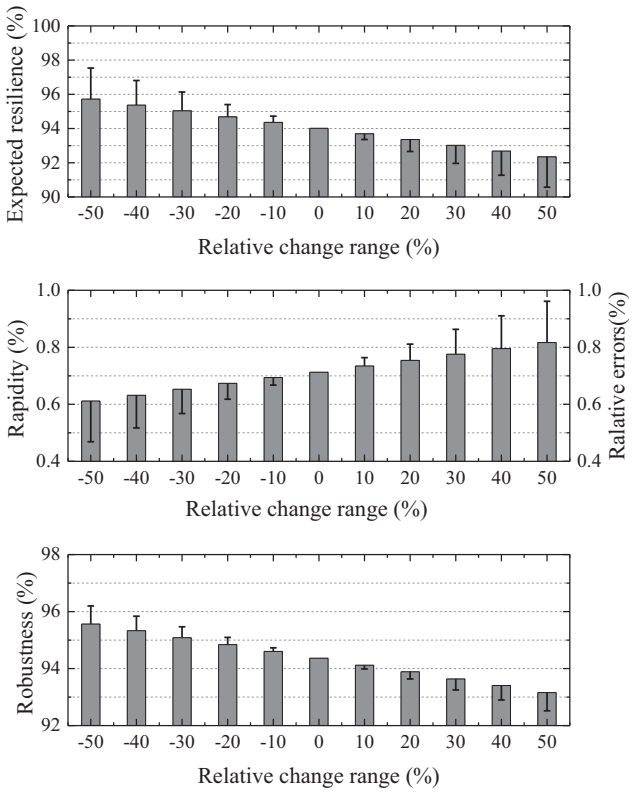

Figure 12. Moderate values and relative errors in 50 years of (a) expected resilience, (b) rapidity, and (c) robustness (RM)

bridge located in California, the following conclusions are drawn:

1. The occurrence proportions of NF and FF earthquakes have significant effects on the seismic hazard, seismic fragility, and functionality recovery function. Using the RM approach to integrate these three stages in the analysis procedure, the expected seismic resilience of bridges, including the impact of near-fault earthquakes, can be assessed.
2. The seismic resilience of the bridge in MR and SR conditions has been compared, and the relative error is about 4%, with more conservative results for MR.
3. Additional cases assuming the bridge is located in other near-fault regions are analyzed, changing the original occurrence proportion of NF and FF earthquakes to -50%—+ 50%. The maximum relative error for the expected resilience is nearly 2%, resulting in relative errors of about 10%.
4. The uncertainties of the parameters in the functionality recovery functions may affect the relative errors in using the SM conditions, reaching 15%. This indicates that the proposed method (RM) may significantly improve the accuracy of the seismic resilience assessment.

In conclusion, the proposed method is recommended for assessing the seismic resilience of bridges in near-fault regions. These results refer to a specific illustrative example of a steel-concrete composite bridge and should be extended to other bridge typologies, even though they could represent a good starting point for investigation.

In fact, the calculation process and methodology presented in the paper can be used as a reference for exploring the effects on different types of bridges at the regional level, where an additional component vulnerability database is required. This certainly represents an interesting future extension of the present investigation.

Acknowledgments

The authors would like to thank the editor and the anonymous reviewers for their constructive comments and valuable suggestions for improving the quality of the article. The financial support received from the National Science Foundation of China (Grant No. 52078176), the National Key Research and Development Program of China (Grant No. 2021YFB2600500), Wenzhou Basic Social Development Science and Technology Project (Grant No. S20220006), and Scientific Research Fund of Institute of Engineering Mechanics, China Earthquake Administration (Grant No. 2019D18) are gratefully appreciated. This study was also supported by FABRE – "Research Consortium for the Evaluation and Monitoring of Bridges, viaducts and other structures" (www.consorziofabre.it/en).
This work was also carried out with a financial grant from the Research Fund for Coal and Steel of the European Community, within the SEQBRI project "Performance-Based Earthquake Engineering Analysis of Short–Medium Span Steel-Concrete Composite Bridges," Grant RFSR-CT-2012-00032. Any opinion expressed in the paper does not necessarily reflect the view of the funder.

References

[1] Decò A, Bocchini P, Frangopol DM. A probabilistic approach for the prediction of seismic resilience of bridges. *Earthq Eng Struct Dyn*. 2013;42(10):1469–1487.
[2] Kalemi B, Caputo AC, Paolacci F, et al. A probabilistic framework for the estimation of resilience of process plants under Na-Tech seismic events. *Bull Earthq Eng*. 2024;22(1): 75–106. doi:10.1007/s10518-023-01685-z.
[3] Bruneau M, Chang SE, Eguchi RT, et al. A framework to quantitatively assess and enhance the seismic resilience of communities. *Earthq Spectra*. 2003;19(4):733–752.
[4] Bankoff G, Frerks G, Hilhorst D. *Mapping Vulnerability: Disasters, Development and People*. London: Earthscan; 2004.
[5] Cimellaro GP, Reinhorn AM, Bruneau M. Seismic resilience of a hospital system. *Struct Infrastruct Eng*. 2010a;6(1–2):127–144.
[6] Bruneau M, Reinhorn A. Exploring the concept of seismic resilience for acute care facilities. *Earthq Spectra*. 2007;23(1): 41–62.
[7] Cimellaro GP, Reinhorn AM, Bruneau M. Framework for analytical quantification of disaster resilience. *Eng Struct*. 2010b;32(11):3639–3649.
[8] Porter KA. An overview of PEER's performance-based earthquake engineering methodology. In: *Proceedings of Ninth International Conference on Applications of Statistics and*

Probability in Civil Engineering; July 6–9, 2003; San Francisco, California, USA.
[9] Federal Emergency Management Agency (FEMA). *Seismic Performance Assessment of Buildings Volume 1— Methodology, Technical Report FEMA-P58*. Washington, DC; 2012b.
[10] Echevarria A, Zaghi AE, Christenson R, et al. CFFT bridge columns for multihazard resilience. *J Struct Eng*. 2015;142(8): C4015002. doi:10.1061/(ASCE)ST.1943-541X.0001292.
[11] Karamlou A, Bocchini P. Computation of bridge seismic fragility by large-scale simulation for probabilistic resilience analysis. *Earthq Eng Struct Dyn*. 2015;44(12):1959–1978. doi:10.1002/eqe.2567.
[12] Xu N, Guikema SD, Davidson RA, et al. Optimizing scheduling of post-earthquake electric power restoration tasks. *Earthq Eng Struct Dyn*. 2007;36(2):265–284. doi:10.1002/eqe.623.
[13] Cimellaro GP, Malavisi M, Mahin S. Using discrete event simulation models to evaluate resilience of an emergency department. *J Earthq Eng*. 2016;21(2):203–226. doi:10.1080/13632469.2016.1172373.
[14] Bonstrom H, Corotis RB. First-order reliability approach to quantify and improve building portfolio resilience. *J Struct Eng*. 2014;142(8):C4014001. doi:10.1061/(ASCE)ST.1943-541X.0001213.
[15] Andrić JM, Lu D-G. Fuzzy methods for prediction of seismic resilience of bridges.. *Int J Disaster Risk Reduct*. 2017;22:458–468, ISSN 2212–4209. doi:10.1016/j.ijdrr.2017.01.001.
[16] Paredes R. A time-dependent seismic resilience analysis approach for networked lifelines; 2015.
[17] Dong Y, Frangopol DM, Saydam D. Time-variant sustainability assessment of seismically vulnerable bridges subjected to multiple hazards. *Earthq Eng Struct Dyn*. 2013;42(10): 1451–1467.
[18] Reed DA, Kapur KC, Christie RD. Methodology for assessing the resilience of networked infrastructure. *IEEE Syst J*. 2009;3(2):174–180.
[19] Ouyang M, Dueñas-Osorio L. Time-dependent resilience assessment and improvement of urban infrastructure systems. *Chaos*. 2012;22(3):033122.
[20] Quinci G, Gagliardi V, Pallante L, et al. A novel bridge monitoring system implementing ground-based, structural and remote sensing information into a GIS-based catalogue. In: *Proceedings of SPIE— The International Society for Optical Engineering*, 2022; Berlin, 5–7 Sept 20. doi:10.1117/12.2637913.
[21] Alavi B, Krawinkler H. *Effects of Near-Fault Ground Motions on Frame Structures. Technical Report, Blume Center Report 138*. California: Stanford; 2001.
[22] Billah AM, Alam S, Bhuiyan MAR. Fragility analysis of retrofitted multi-column bridge bent subjected to near fault and far field ground motion. *J Bridge Eng*. 2013;18(10):992–1004.
[23] Baker JW. Quantitative classification of near-fault ground motions with wavelet analysis. *Bull Seismol Soc Am*. 2007;97(5):1486–1501.
[24] Bocchini P, Dan MF. Probabilistic Functionality Recovery Model for Resilience Analysis. In: *Bridge Maintenance, Safety, Management, Resilience and Sustainability*. 2012. p. 1920–1927. doi:10.1201/BMSM.
[25] Liu Y, Lu DG, Paolacci F. Probabilistic seismic resilience analysis for bridges shocked by near-fault pulse-like ground motions. In: *Maintenance, Monitoring, Safety, Risk and Resilience of Bridges and Bridge Networks*. CRC Press; 2016:230–231.
[26] Cornell CA, Jalayer F, Hamburger RO, et al. Probabilistic basis for 2000 SAC federal emergency management agency steel moment frame guidelines. *J Struct Eng*. 2002;128(4):526–533.
[27] Chang SE, Shinozuka M. Measuring improvements in the disaster resilience of communities. *Earthq Spectra*. 2004;20(3):739–755.
[28] Kafali C, Grigoriu M. 20Rehabilitation decision analysis. In: *ICOSSAR'05, Proceedings of the 9th International Conference on Structural Safety and Reliability, 19–23 June*, 2005; Rome, Italy.
[29] Mcguire RK. Probabilistic seismic hazard analysis and design earthquakes: closing the loop. *Int J Rock Mech Min Sci Geomech Abstr*. 1996;33(7):294A.
[30] Lin T, Baker JW. Probabilistic seismic hazard deaggregation of ground motion prediction models; 2011.
[31] Shahi SK. A probabilistic framework to include the effects of near-fault directivity in seismic hazard assessment (Doctoral dissertation, Stanford University); 2013.
[32] U.S. Geological Hazard Science Center. Accessed February 01, 2017. https://geohazards.usgs.gov/deaggint/2008/.
[33] Zhai C, Chang Z, Li S, et al. Quantitative identification of near-fault pulse-like ground motions based on energy. *Bull Seismol Soc Am*. 2013;103(5):2591–2603.
[34] Paolacci F, Corritore D. Performance-based earthquake engineering analysis of short-medium span steel-concrete composite bridges. In: *Italian Concrete Conference* (pp. 682–696); April 2021; Cham: Springer Nature Switzerland.
[35] Yang L, Paolacci F, Da-Gang L. Seismic fragility of a typical bridge using extrapolated experimental damage limit states. *Earthq Struct*. 2017;13(6):599–611. doi:10.12989/eas.2017.13.6.599.
[36] Chabrolin B, Kretz T, Laravoire J. *Steel-Concrete Bridges. A Guide for Novel Structures*. Paris: French National Project MIKTI; 2008.
[37] CEN. *Eurocode 8: Design of Structures for Earthquake Resistance, Part 1: General Rules, Seismic Actions and Rules for Buildings*. Brussels: European Committee for Standardization; 2005.
[38] McKenna F, Mazzoni S, Scott MH, et al. *OpenSees Command Language Manual*. Berkeley, July: Pacific Earthquake Engineering Research Center, University of California; 2007.
[39] Menegotto M, Pinto PE. Method of analysis for cyclically loaded RC plane frames including changes in geometry and non-elastic behavior of elements under combined normal force and bending. In: *Proceedings of IABSE Symposium on Resistance and Ultimate Deformability of Structures Acted on by Well Defined Repeated Loads*; 1973; Lisboa.
[40] Kent DC, Park R. Flexural members with confined concrete. *J Struct Div*. 1971;97(7):1969–1990.
[41] Liu Y, Paolacci F, Lu D. Seismic fragility of a typical bridge using extrapolated experimental damage limit states. *Earthq Struct*. 2017;13(6):599–611.
[42] CEN. *Eurocode 4: Design of Composite Steel and Concrete Structures*. Brussels: European Committee for Standardization; 2006.
[43] Gattesco N, Giuriani E. Experimental study on stud shear connectors subjected to cyclic loading. *J Constr Steel Res*. 1996;38(1):1–21.
[44] Abbiati G, Cazzador E, Alessandri S, et al. Experimental characterization and component-based modeling of deck-to-pier connections for composite bridges. *J Constr Steel Res*. 2018;50(1):31–50. doi:10.1016/j.jcsr.2018.08.005.

[45] Bradley B. The seismic demand hazard and importance of the conditioning intensity measure. *Earthq Eng Struct Dyn*. 2012;41:1417. doi:10.1002/eqe.2221.
[46] De Biasio M, Grange S, Dufour F, et al. Intensity measures for probabilistic assessment of non-structural components acceleration demand. *Earthq Eng Struct Dyn*. 2015;44(13):2261–2280. doi:10.1002/eqe.2582.
[47] Shome N, Cornell CA, Bazzurro P, et al. Earthquakes, records, and nonlinear responses. *Earthq Spectra*. 1998;14(3):469–500.
[48] Giovenale P, Cornell C, Esteva L. Comparing the adequacy of alternative ground motion intensity measures for the estimation of structural responses. *Earthq Eng Struct Dyn*. 2004;33(8):951–979.
[49] U.S. geological hazard science center. 2017b. Accessed 15 January 2017. https://earthquake.usgs.gov/hazards/qfaults/map/#qfaults.
[50] Yong A, Thompson EM, Wald D, et al. Compilation of Vs30 data for the United States: U.S. Geological Survey Data Series 978, 8 p.
[51] Shahi SK, Baker JW. An empirically calibrated framework for including the effects of near-fault directivity in probabilistic seismic hazard analysis. *Bull Seismol Soc Am*. 2011;101(2): 742–755.
[52] Chioccarelli E, Iervolino I. Near-source seismic hazard and design scenarios. *Earthq Eng Struct Dyn*. 2013;42(4):603–622.
[53] U.S. Geological Hazard Science Center. 2017c. Accessed February 01, 2017. http://geohazards.usgs.gov/hazardtool/application.php.
[54] Ancheta TD, Darragh RB, Stewart JP et al. *PEER NGA-West2 Database, PEER Report 2013/03*. Berkeley: Pacific Earthquake Engineering Research Center. University of California; 2013.
[55] Stewart JP, Chiou SJ, Bray JD, et al. Ground motion evaluation procedures for performance-based design. *Soil Dyn Earthq Eng*. 2002;22(9):765–772.
[56] Bray JD, Rodriguez-Marek A. Characterization of forward-directivity ground motions in the near-fault region. *Soil Dyn Earthq Eng*. 2004;24(11):815–828.
[57] Padgett JE. Selection of optimal intensity measures in probabilistic seismic demand models of highway bridge portfolios. *Earthq Eng Struct Dyn*. 2008;37(5):711–725.
[58] Wen YK, Ellingwood BR, Veneziano D, et al. Uncertainty modeling in earthquake engineering. MAE center project FD-2 report; 2003.
[59] Baker JW, Lin T, Shahi SK, Jayaram N. New ground motion selection procedures and selected motions for the PEER transportation research program. *Peer Rep*. 2011; 2011:3.
[60] Tothong P, Cornell CA. Structural performance assessment under near-source pulse-like ground motions using advanced ground motion intensity measures. *Earthq Eng Struct Dyn*. 2008;37(37):1013–1037.
[61] Paolacci F, Corritore D. Performance-based earthquake engineering analysis of short-medium span steel-concrete composite bridges. In: *Lecture Notes in Civil Engineering, Volume 351, Pages 682–696, 2023 Italian Concrete Conference, ICC 2021, Virtual, Online 14 April 2021 through 17 April 2021*; 2023. doi:10.1007/978-3-031-37955-0_49.
[62] Muntasir Billah AHM, Shahria Alam M. Seismic fragility assessment of highway bridges: a state-of-the-art review. *Struct Infrastruct Eng*. 2015;11(6):804–832.
[63] Stefanidou SP, Kappos AJ. Methodology for the development of bridge-specific fragility curves. *Earthq Eng Struct Dyn*. 2017;46(1):73–93.
[64] Tirca L, Serban O, Lin L, et al. Improving the seismic resilience of existing braced-frame office buildings. *J Struct Eng*. 2015;142(8):C4015003.
[65] Shinozuka M, Zhou Y, Kim SH, et al. Socio-economic effect of seismic retrofit implemented on bridges in the Los Angeles highway network. Final Report to the California Department of Transportation; 2005.
[66] HAZUS. *MR4 Earthquake Model Technical Manual*. Washington (DC): Department of Homeland Security, Federal Emergency Management Agency, Mitigation Division; 2009.
[67] ATC. *Earthquake Damage Evaluation Data for California. Technical Report ATC-13*. Redwood City, CA: Applied Technology Council (ATC); 1985.

BER the international journal of bridge engineering management and research

Demand Model for Concrete Barriers Subject to Tractor Tanker-Trailer Impact

Ran Cao[1,*]; Sherif El-Tawil[2]; Anil Kumar Agrawal[3]; and Waider Wong[4]

Submitted: 22 January 2024 **Accepted:** 11 July 2024 **Publication date:** 03 September 2024

DOI: 10.70465/ber.v1i1.3

Abstract: Test-level-6 (TL-6) barriers are specified for situations that involve a high percentage of truck traffic or unfavorable site conditions, where truck rollover or penetration beyond the railing could result in severe traffic consequences. Previous studies of TL-6 barriers impacted by tractor tanker-trailers (the truck category that creates the highest impact demands) assumed that the barriers behave rigidly. The rigid barrier assumption is investigated in this paper through simulation studies in which validated nonlinear models of the truck and barrier are employed. Parametric simulations are carried out to evaluate the effects of truck velocities, weights, and barrier heights on the impact force demands. The demand model in the current design guideline is critiqued based on the simulation results, and a discrepancy was found between the predicted barrier performance by AASHTO-LRFD loading and the truck impact. A revised demand model is proposed based on the simulation results.

Author keywords: Heavy truck impact; Concrete barriers; Impact design load

Introduction

In the current AASHTO-LRFD's Section 13,[1] TL-6 barriers are specified for situations that involve a high percentage of truck traffic or unfavorable site conditions, where truck rollover or penetration beyond the railing could result in severe traffic consequences. Many state DOTs, such as New York, New Jersey, and Pennsylvania, are currently considering the implementation of TL-6 barriers.[2] According to the,[3] the general impact conditions, truck speed, and weight associated with MASH TL-6 heavy trucks are based on a 360-kN tank-type tractor-trailer traveling at 80 kph. The current AASHTO-LRFD Section 13 specifies a lateral static design force of 778 kN to represent a TL-6 truck impact. This provision stems from limited crash tests and engineering experience.

More recently, numerical simulations using validated finite element (FE) models of heavy trucks were used to assess the impact force demands. Bligh et al.[4] conducted a simulation study on the impact load demands for TL-5 barriers with different heights using the 360-kN MASH van-type tractor-trailer model. Based on their parametric studies, a dynamic demand model for TL-5 barriers was proposed as a function of truck speeds and weights. Compared with the TL-5 barrier, studies on the TL-6 demand model have been rather limited, primarily due to the lack of a well-calibrated tank-type tractor-trailer model.

Whitfield et al. [5] used computational modeling to propose a new MASH TL-6 barrier. In their study, a preliminary TL-6 tank-type tractor-trailer model was developed by modifying an existing TL-5 van-type tractor-trailer. The developed TL-6 truck model was validated against an instrumented wall test by Beason et al.[6]. They noted that the general impact behavior of the modified TL-6 truck model was found to be similar to the test results. However, the forces imparted to the simulated wall, which was assumed to be rigid, as done by Bligh et al.,[4] were much lower than those from the tests. In subsequent phases of their study, the truck model was further refined by Rasmussen et al.,[7] incorporating more detailed chassis components and ballast modeling. Although better simulation results were achieved than that in phase 1,[5] the simulation results still underestimated the peak impact force from the testing by 26%.[7]

A key limitation of previous simulation studies is that the barriers were assumed to behave in a rigid manner. Since the influences of this key assumption are not known, realistic inelastic modeling of the barrier is needed to simulate the impact demand and failure pattern of the barrier more accurately. The simulated barrier behaviors from nonlinear modeling can be used to further validate the static design load specified in the current design guidelines. Moreover, the speed and weight of the MASH TL-6 truck were assumed

*Corresponding Author: Ran Cao. Email: rcao@hnu.edu.cn

[1]Associate Professor, Key Laboratory for Damage Diagnosis of Engineering Structures of Hunan Province, Hunan Univ., Changsha, 410082, China; College of Civil Engineering, Hunan University, Changsha, 410082, China

[2]Professor, Dept. of Civil & Environmental Engineering, University of Michigan, Ann Arbor, MI, 48109

[3]Professor, Dept. of Civil and Environmental Engineering, The City College of the City University of New York, New York, NY, 10031

[4]Engineer, Federal Highway Administration, Baltimore, MD, 21201

Discussion period open till six months from the publication date. Please submit separate discussion for each individual paper. This paper is a part of the Vol. 1 of the International Journal of Bridge Engineering, Management and Research (© BER), ISSN 3065-0569.

to be constant, i.e., 80 kph and 360 kN. Further research is needed to develop a more comprehensive understanding of the demand model for the TL-6 barrier by varying the velocity and weight of the tractor-trailer. This study addresses these key limitations in the existing literature, which is quite limited to date. Concrete barriers are more commonly used for TL-6 test levels than steel railings. Hence, this study was mainly focused on the impact behaviors of TL-6 concrete barriers. Simulation results from this study could also serve as an important reference for developing new and refining existing design guidelines for barriers and bridge deck overhangs, such as Section 13 of AASHTO-LRFD.[1]

Finite Element Model of The Truck

Currently, there is no well-calibrated TL-6 tank-type tractor-trailer available. Hence, a representative MASH TL-6 tractor-tanker trailer model was developed by modifying a validated TL-5 van-type tractor-trailer. Details about the TL-5 truck can be found in Miele et al.[8]. Similar to the MwRSF study,[5] the van body on the TL-5 vehicle was replaced with an elliptical cylinder (tank) while keeping the original tractor and the rear tandem axle. Fig. 1 shows the developed TL-6 truck model in LS-DYNA,[9] where the tank model was constrained to the railings on top of the trailer bed. The geometry of the truck model was determined based on key requirements by MASH,[3] such as the overall length and location of the center of gravity of the truck.

Whitfield et al.[5] conducted a field survey on the geometry of the TL-6 trucks and provided the dimensions of typical tank-trailers. Based on their report, the tank modeled in this work has an elliptical shape with a dimension of 12.4 m (length) × 2.3 m (width) × 1.6 m (height). Shell elements were used to model the tank, and the shell's thickness was assumed to be 2.3 mm. The nonlinearity of the steel tank was modeled using *MAT_PLASTIC_KINEMATIC in LS-DYNA.[9] The strength of the steel was assumed to be

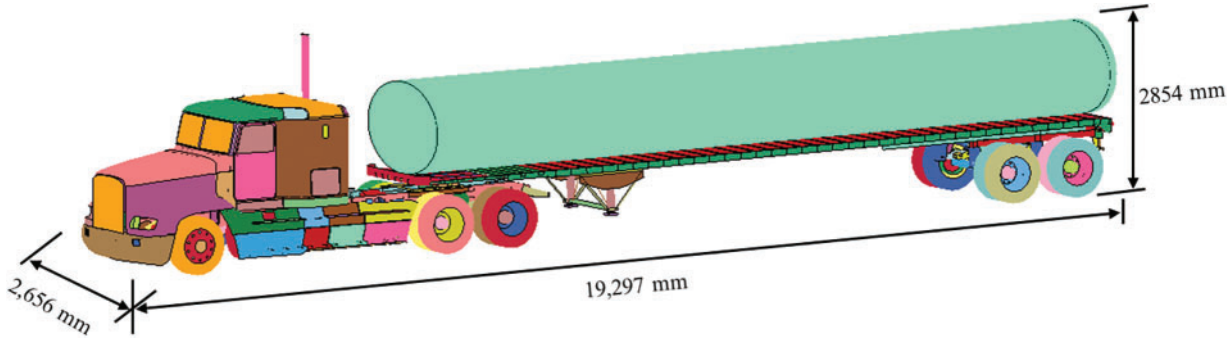

Figure 1. Developed FE model of the TL-6 truck

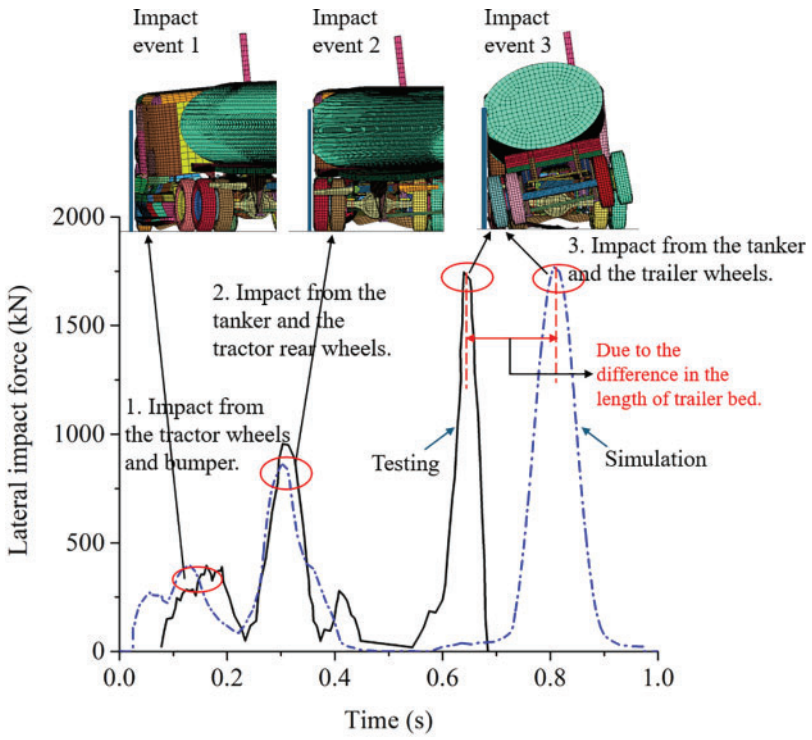

Figure 2. Impact force comparison of testing results and simulation

414 Mpa with a tangent modulus of 600 Mpa. The element size for the tank part is 100 mm in the simulation. The ballast in the tanker was modeled using soft materials to represent a flexible cargo with a Young's modulus of 1.5 Mpa. However, liquid sloshing in the tank was not considered. The center of mass for the ballast is 2,050 mm above the ground, and the overall length of the truck model is 19,297 mm, which both matched the requirements of MASH.[3] The total number of elements in the truck model is roughly 272,800.

To validate the developed TL-6 truck model, the 1989 TTI instrumented wall test[6] was simulated to compare the impact behaviors of the truck along with its impact force time histories with those from the test. According to the testing report,[6] the truck weight was 360 kN, the impact speed was 88 kph, and the impact angle was 16 degrees. Based on the testing report, the damage to the barrier was mostly cosmetic, and the detailed rebar drawing of the testing wall was not available. Therefore, the barrier wall was modeled as elastic with its height and length maintained the same as that in the testing.

Considering that the test is very old, the comparison was deemed preliminary. The focus of this validation was to ensure that the crash behavior of the tractor-trailer during the test and simulation were reasonably similar.

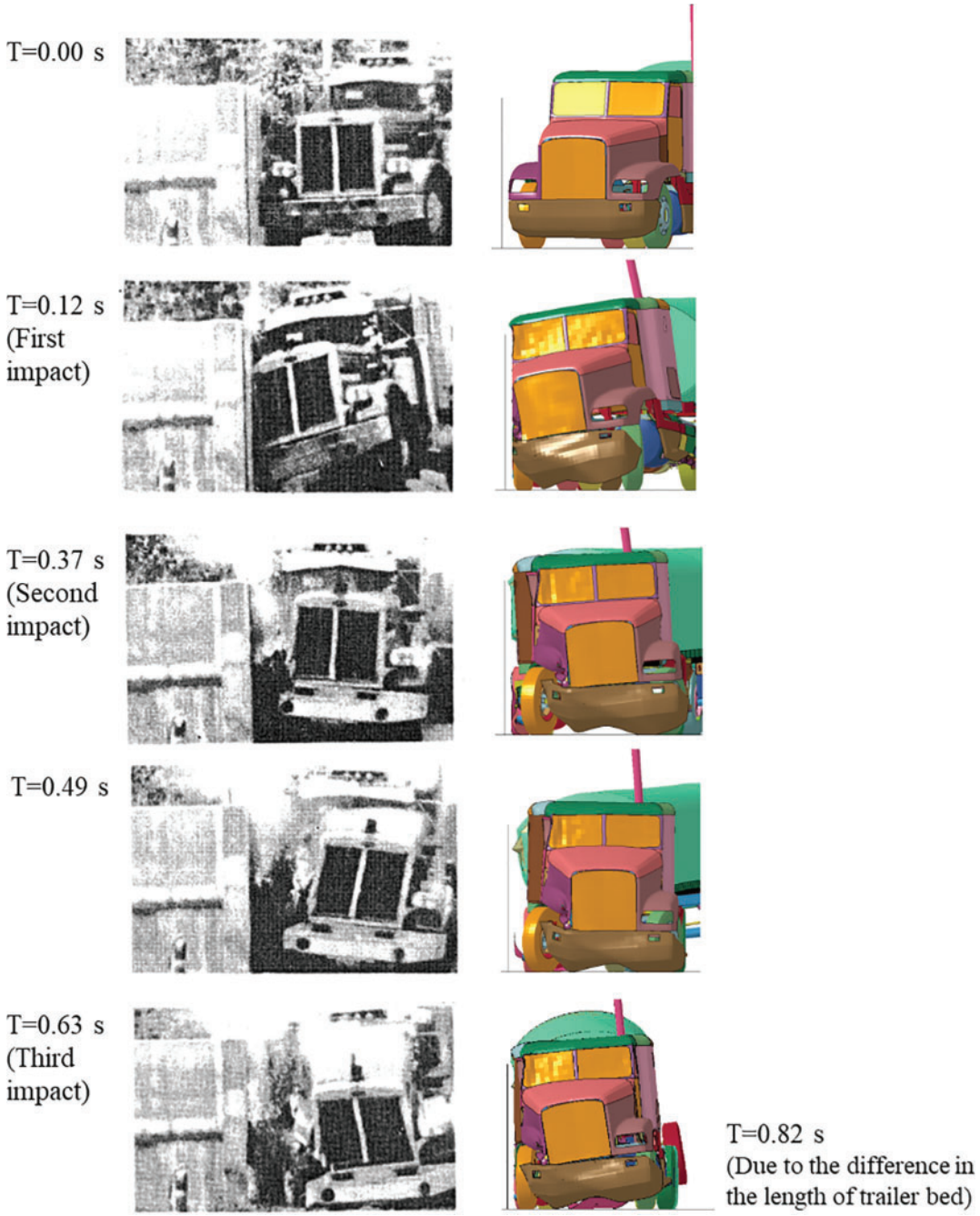

Figure 3. Comparison of truck behaviors between the crash testing and simulations (front view). (T is the time during the impact process.)

Based on the simulation in LS-DYNA,[9] Fig. 2 shows the comparison between the impact force time history from the simulation and the test. The impact force was obtained by defining the contact between the barrier and the truck from LS-DYNA. It can be observed from Fig. 2 that the simulated force time history matches the one from the impact test reasonably well. In Fig. 2, the crash process for the TL-6 truck consisted of three impact events. The first one was related to the impact from the tractor wheels and bumper; the second one was from the tanker and the tractor rear wheels; the third impact was related to the tanker and the trailer wheels (i.e., the back-slap), which is the most severe one. From Fig. 2, the simulated peak forces for each of the three impact events matched the testing results well.

Detailed comparison of the truck behaviors during the testing and simulations can be seen from Figs. 3 and 4. In the series of photos, the truck was well-directed, and the simulated truck behavior matched the testing results reasonably well. In particular, the inclined angles of the actual tractor and trailer were found to be similar to those from the simulations. It should be noted that a short time lag of 0.19 sec was observed during the third impact, which was due to the difference in the length of the trailer's bed. Given the results shown in Figs. 2–4, the TL-6 truck model was able to represent the MASH TL-6 truck and can be used to investigate the demand models further.

Truck Impact Simulation with MASH TL-6 Concrete Barriers

Fig. 5a shows the TL-6 concrete barrier model based on an actual design drawing from the Texas Department of Transportation (Fig. 5b). Based on a survey by Agrawal et al.,[2] the current TL-6 barrier design is quite standard, and

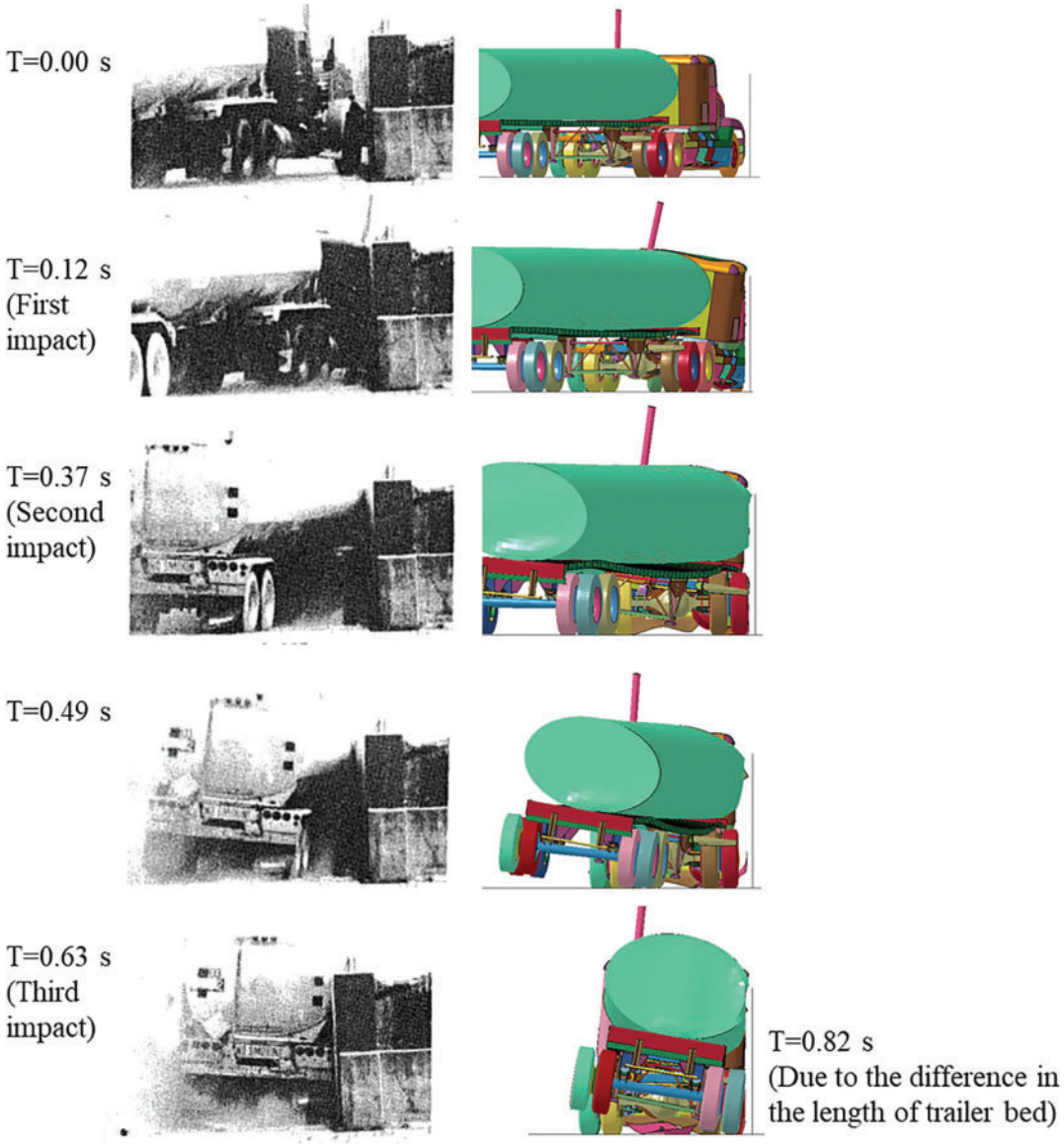

Figure 4. Comparison of truck behaviors between the crash testing and simulations (rear view). (T is the time during the impact process.)

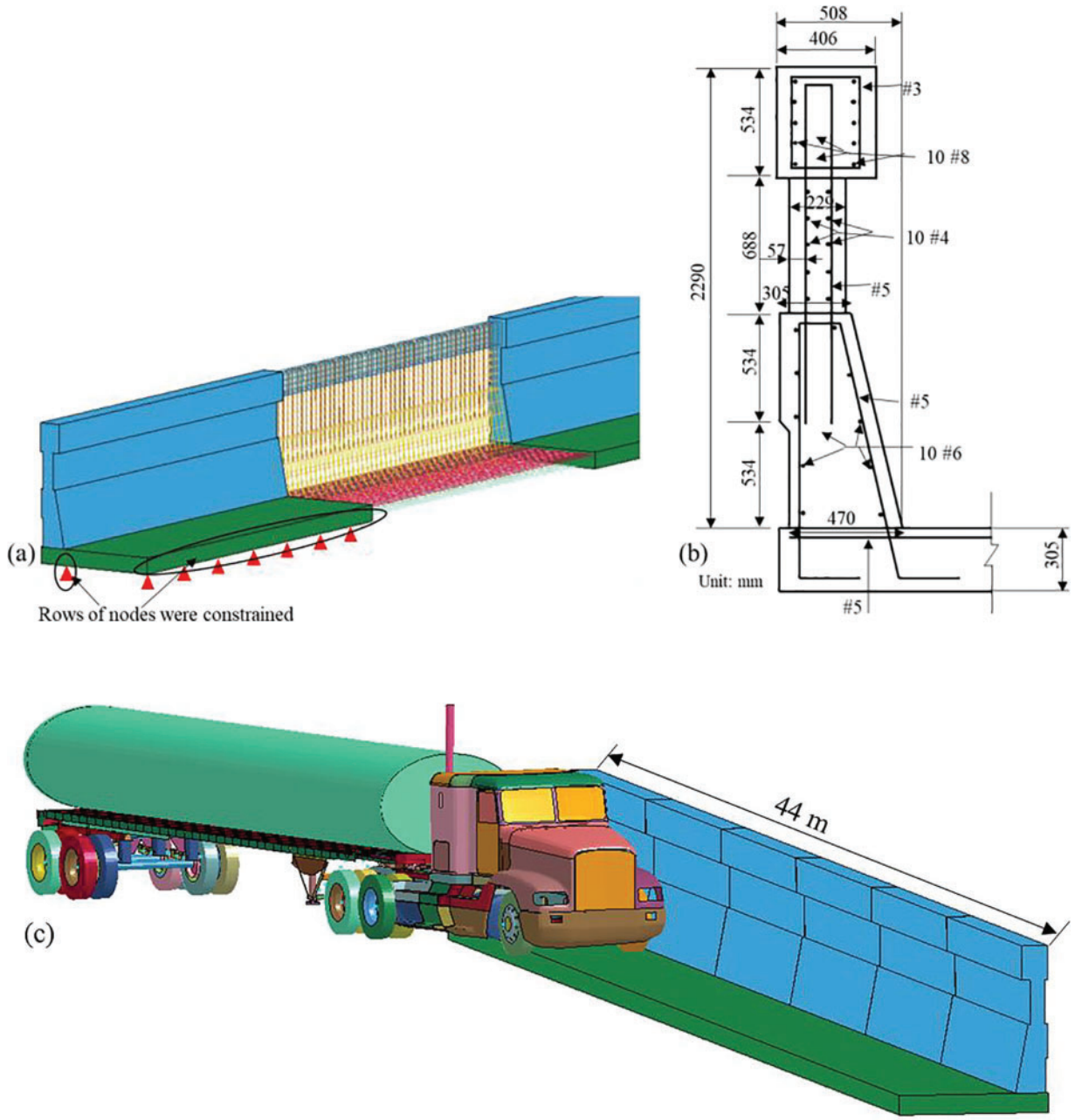

Figure 5. MASH TL-6 concrete barrier: (a) FE model of the barrier; (b) standard drawing; and (c) simulation setup

most TL-6 barriers used in the U.S. follow the drawings used in this work. The barrier is 2,290 mm tall, and the thickness of the slab is 305 mm. The behavior of the concrete material under impact loads was represented by the Continuous Surface Cap Model (MAT 159) in LS-DYNA.[9] As shown in Fig. 5a, the steel rebars were explicitly modeled using Hughes-Liu beam elements. The yielding and hardening behavior of the steel bars were modeled using material model MAT 3 in LS-DYNA.[9] The compressive strength of the concrete was assumed to be 25 Mpa and the strength of steel rebars in the parapet and deck was 414 Mpa and 276 Mpa. More details about the reinforced concrete modeling and its validations can be found in Agrawal et al.[10] and Cao et al.[11]. To simulate the overhang of the bridge, the nodes of the deck at the girder stems were modeled as fixed. Fig. 5c shows the simulation setup of the MASH truck impact in LS-DYNA, where the total length of the barrier is 44 m and the impact angle is 15 degrees.

As per MASH,[3] the weight of the TL-6 truck is 360 kN, and the impact velocity is 80 kph. The simulated impact responses of the barrier are shown in Fig. 6, including the time history curves of the impact force and barrier displacement. As shown in Fig. 6a, the peak impact force caused by the back-slap was around 930 kN with an impulse duration of less than 0.2 sec. The observed peak impact force is 20% higher than the prescribed design force for the TL-6 barrier in the current AASHTO-LRFD[1]—although comparing the forces is inappropriate because the former is the peak value

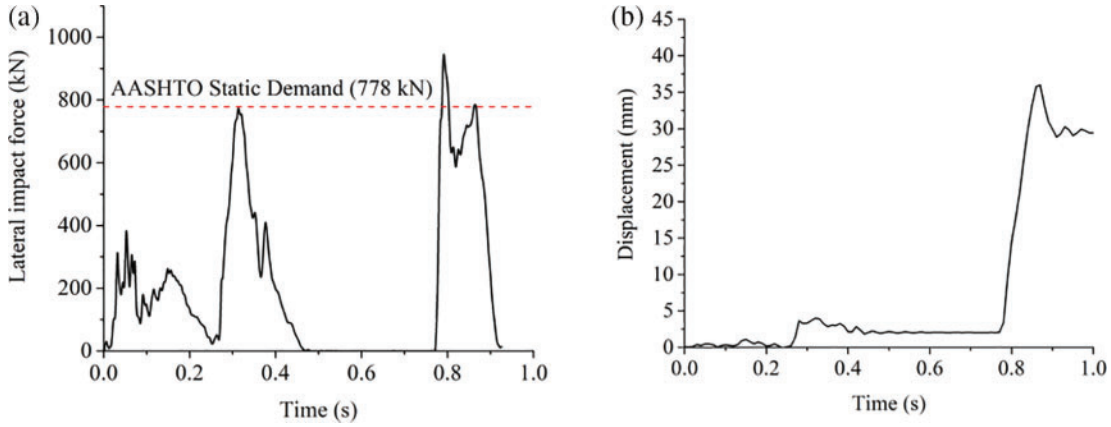

Figure 6. Time history response of TL-6 concrete barrier under MASH truck impact: (a) impact force; (b) lateral displacement of the barrier

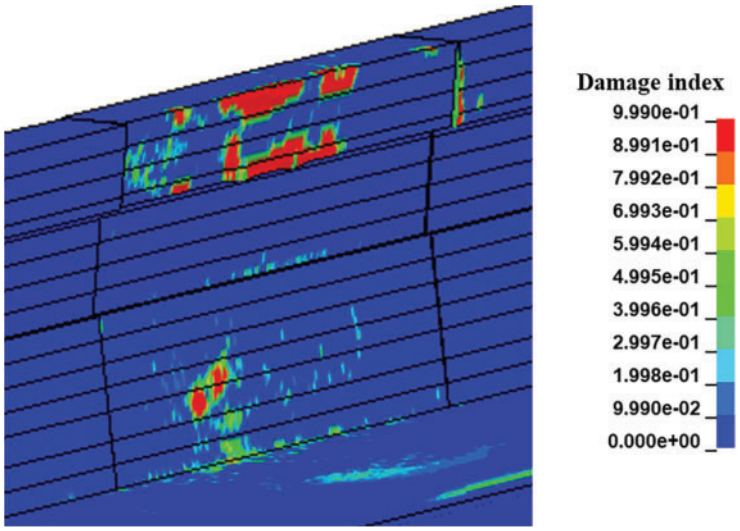

Figure 7. Damage to the barrier caused by MASH TL-6 truck impact

of a time history response, whereas the latter is an equivalent static design load. The peak displacement of the barrier was around 35 mm, as shown in Fig. 6b. The displacement was measured from the top of the barrier and above the impact region from the truck. The damage pattern of the barrier after the back-slap impact is shown in Fig. 7, where minor concrete cracking occurred in the front face of the barrier. The damage index shown in Fig. 7 was defined by Hallquist,[9] where 0.0 means no damage and 1.0 means total damage. Based on the simulation, the truck was successfully redirected and no rollover occurred.

Fig. 8 provides detailed information about the impact locations along the barrier height. The first impact occurred at 508 mm above the ground. The second and third impact events occurred at two different heights, one located at 380 mm above the ground by the wheels' impact and another from 1,780 to 2,286 mm above the ground by the tanker impact. It should be noted that the effective height to apply the TL-6 design load is assumed to be 1,422 mm in the current AASHTO-LRFD.[1] Based on the simulation, the prescribed loading height in AASHTO is between the hit points by the tanker (highest) and the wheels (lowest). It should also be noted that the loading length of the back-slap force was essentially the length of the two wheels and the trailer bed overhang, which was consistent with the prescribed loading length in AASHTO-LRFD.[1]

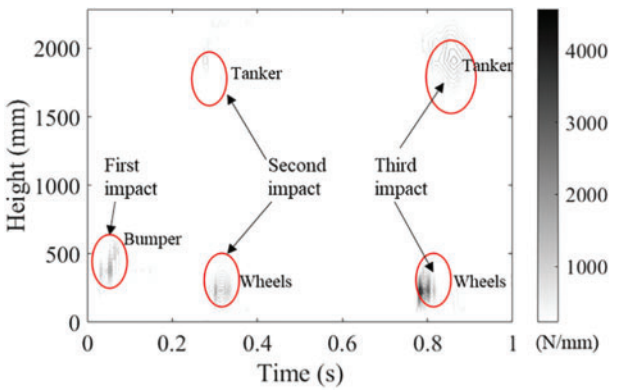

Figure 8. Distribution of impact force on the barrier under MASH TL-6 condition

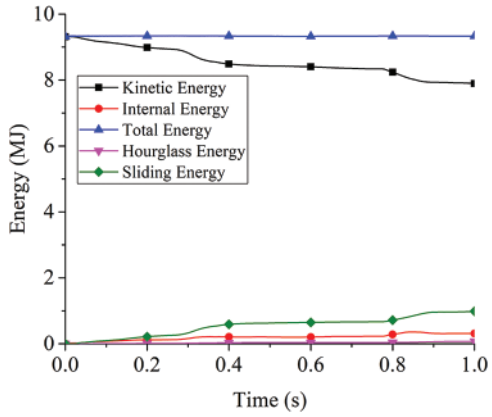

Figure 9. Energy conservation plots from the MASH TL-6 simulation

To further illustrate the validity of the simulation, Fig. 9 shows the energy conservation of the simulation, where the total energy was almost constant and the hourglass energy was effectively controlled. Since the barrier redirected the truck successfully and only showed minor damages, the kinetic energy from the truck did not decrease much and the internal energy of the system was relatively low (only 3% of the total energy).

Parametric Study

MASH [3] guidelines specify a given truck speed and weight for designing TL-6 barriers (i.e., 80-kph speed and 360-kN truck weight). To better understand the barrier's general response to impact and broaden the research space, parametric studies were conducted by varying the truck speed from 64 to 112 kph in increments of 16 kph and changing the truck weight from 180 to 360 kN in increments of 90 kN.

Fig. 10a shows the impact force time history for a 360 kN truck at different impact speeds. As shown in Fig. 10a, the peak impact force increased from 400 to 1,690 kN as the velocity increased from 64 to 112 kph. Fig. 10b shows the impact force time history for an 80-kph truck with different truck weights. In Fig. 10b, the back-slap force increased from 490 to 930 kN as the truck weight increased from 180 to 360 kN. It should be noted that the peak impact demand for the 180 and 270 kN trucks was not from the back-slap impact but from the second impact event by the rear tractor wheels and front of the tanker. The peak impact forces for the 180 and 270 kN trucks at 80 kph were around 890 kN.

The time histories of the lateral deformations of the barrier are shown in Fig. 11. In Fig. 11a, the 112-kph truck caused the highest deformations of 214 mm with only mild damage and a small portion of rebars yielded, while the 64-kph truck caused the least deformation of the barrier,

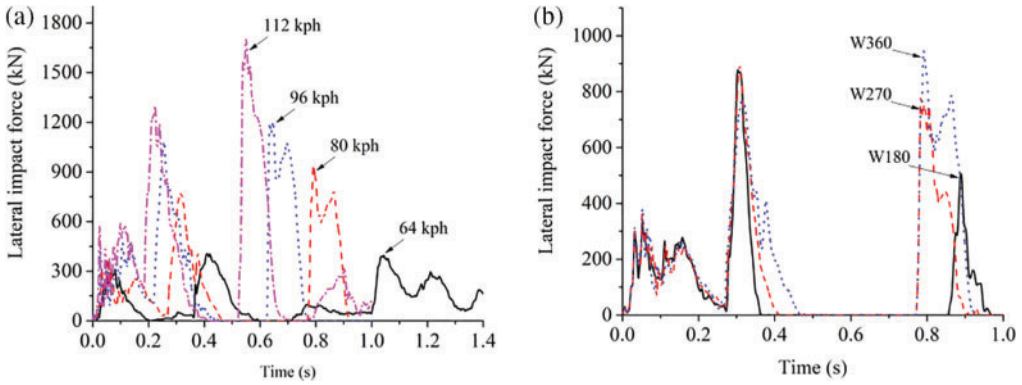

Figure 10. Impact force time histories: (a) truck weight of 360 kN; (b) speed of 80 kph

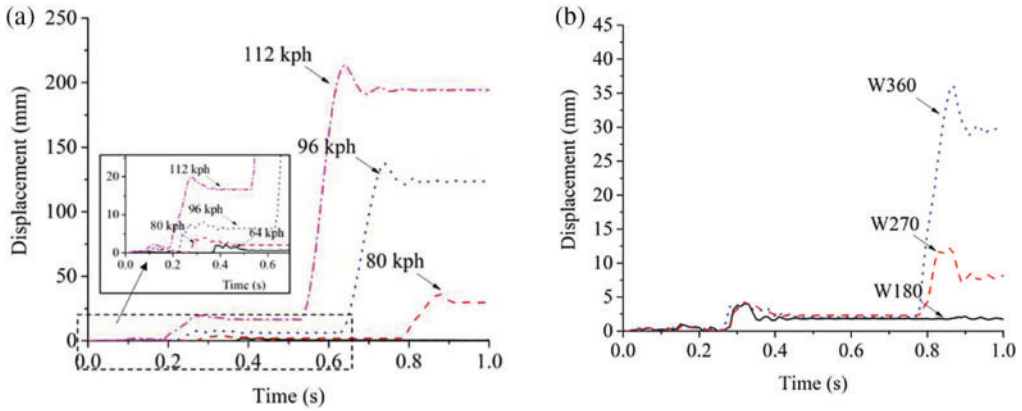

Figure 11. Lateral deformation time histories for truck-tank-trailer colliding with TL-6 concrete barriers: (a) truck weight of 360 kN; (b) truck speed of 80 kph

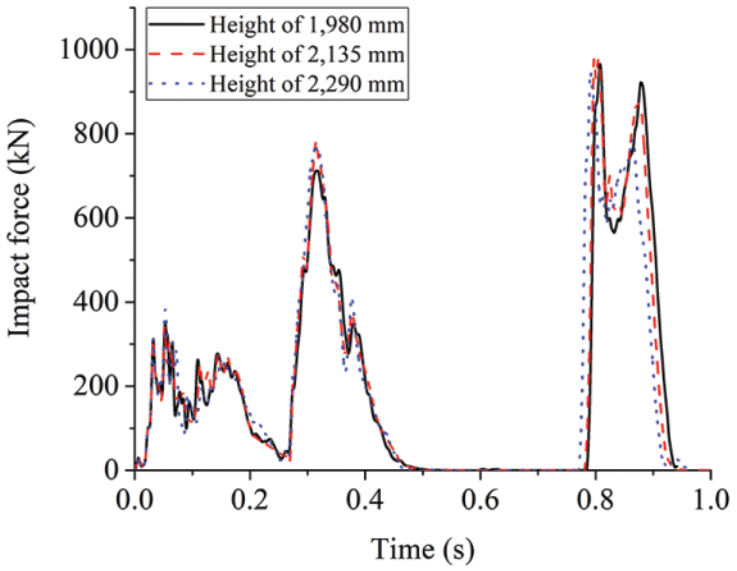

Figure 12. Impact force time-histories of barriers with different heights subjected to MASH conditions

at only 2 mm. It should be noted that the truck was well-redirected in all cases.

In the current AASHTO-LRFD,[1] the minimum barrier height for the MASH TL-6 barrier is 2,290 mm, which is over two times higher than that for TL-5 barriers. To study the influence of barrier height under the MASH condition, i.e., 80-kph speed and 360-kN truck weight, the original barrier height was adjusted in this study to 2,135 and 1,980 mm. In Fig. 12, the simulated impact forces were almost identical for the three different barrier heights. The trucks were also observed to be well-directed based on the simulations and no rollover or penetration occurred. Hence, TL-6 barriers with heights lower than 2,000 mm could be considered for future crash tests and installations.

Critique of AASHTO-LRFD Loading for TL-6 Barrier

As shown in Fig. 6, the dynamic peak impact force by the MASH truck was 20% higher than the 780 kN static design load prescribed by AASHTO-LRFD.[1] It should be noted that a direct comparison between the peak dynamic load and static load is not rigorous. In terms of loading effects, the equivalence of dynamic loads and static design load was validated using nonlinear simulations. To evaluate the accuracy of the AASHTO guidelines, a static load of 780 kN was applied to the barrier as a distributed line loading at a height of 1,422 mm per AASHTO-LRFD. The distribution length was 2,438 mm, as prescribed in the design guidelines.

Fig. 13 shows the simulated barrier deformations subject to truck impact and static loading, in which the AASHTO load predicted a significantly higher deformation than that caused by the MASH truck impact (nearly 6 times higher). Based on the simulation, a reduced static demand at 585 kN is proposed. As shown in Fig. 13 and Table 1, this load is selected to cause a similar deformation as that from truck simulations, which could be considered a more reasonable demand for TL-6 barrier design.

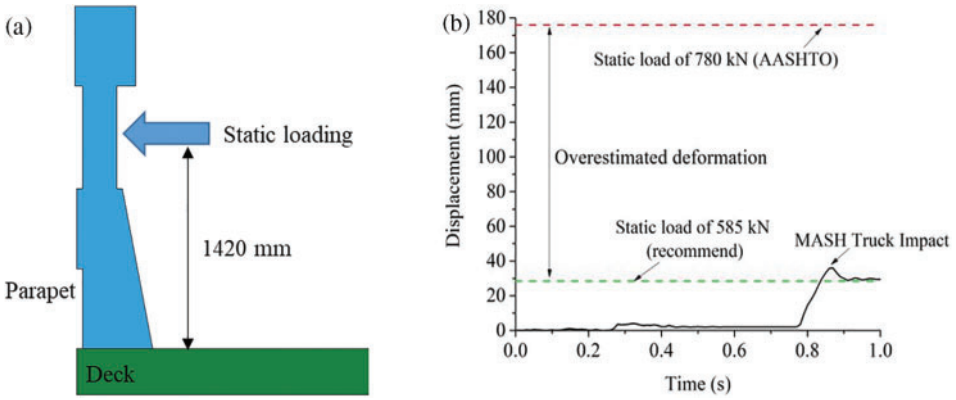

Figure 13. Comparison of the barrier deformation by truck impact and static loading: (a) application of the static loading per AASHTO-LRFD; (b) lateral displacement of the barrier

Table 1. Comparison of loading effects from truck impact and static loading

	Loading (kN)	Lateral deformation (mm)
MASH truck impact	930 (impulse, duration < 0.2 sec)	30
AASHTO	780 (static)	176
Proposed demand	585 (static)	30

Conclusions

A representative MASH TL-6 tractor-tanker trailer was developed and validated against an instrumented wall test. Using the validated TL-6 truck model, the characteristics of the truck impact loading on TL-6 barriers were investigated. Unlike previous studies that modeled the barrier as rigid, the nonlinear responses of the impacting truck and concrete barriers were both considered in the finite element simulations. It was found that the current MASH TL-6 barrier design could successfully redirect a 360-kN truck traveling at 112 kph with only mild damage to the barrier. This observation, coupled with the fact that the impact speed is 40% faster than the speed prescribed in the design guidelines, suggests that the barrier design in current use is overly conservative.

The effects of the barrier height on the MASH TL-6 truck demand were also discussed. The simulation showed that a 15% reduction in the barrier height would cause negligible effects on the impact force and truck behavior. Therefore, the applicability of TL-6 barriers with a lower height could be further investigated through field crash tests.

The design load for the TL-6 barrier prescribed in the current AASHTO-LRFD was further critiqued by comparing the barrier deformations caused by truck impact and the applied static design load. It was confirmed that the current design load could provide significantly higher deformation than that from the truck impact, which may lead to an uneconomical design of the barrier and the supporting bridge deck overhang. Based on the simulation results, a reduced static demand at 585 kN was proposed for a future TL-6 barrier design that delivers a similar loading effect as the truck impact. Further studies can be carried out to incorporate the demand model and calculations of barrier capacities in a performance-based design framework.

Acknowledegments

This work was supported by the National Science Foundation of China Grants 52108136, the National Key Research and Development Program of China (No. 2023YFC3806800), and the Fundamental Research Funds for the Central Universities. This research was also supported, in part, under National Science Foundation Grants CNS-0958379, CNS-0855217, ACI-1126113, and the City University of New York High-Performance Computing Center at the College of Staten Island. Any opinions, findings, conclusions, or recommendations expressed in this publication are those of the authors and do not necessarily reflect the views of the National Science Foundation of China.

Data Availability Statement

All data shown in the paper are available from the corresponding author by request.

References

[1] AASHTO-LRFD. *AASHTO LRFD Bridge Design Specifications*. Washington, DC, USA: American Association of State Highway and Transportation Officials; 2020.

[2] Agrawal AK, El-Tawil S, Cao R. *Numerical FE Crash Simulations of Typical TL-5 & TL-6 Barriers to Verify Correct Impact Forces*. McLean, VA: Federal Highway Administration; 2022 (under press).

[3] Manual for Assessing Safety Hardware (MASH). *AASHTO Subcommittee on Bridges and Structure*. Washington, D.C: American Association of State Highway and Transportation Officials; 2016.

[4] Bligh RP, Briaud JL, Abu-Odeh A, et al. *Design Guidelines for Test Level 3 (TL-3) through Test Level 5 (TL-5) Roadside Barrier Systems Placed on Mechanically Stabilized Earth (MSE) Retaining Wall*. NCHRP Project No. 22–20(2). College Station, Texas: Texas A&M Transportation Institute; 2017.

[5] Whitfield DL, Schmidt JD, Faller RK, et al. *Investigation and Development of a Test Level 6 Barrier, Phase I*. Lincoln, Nebraska: Nebraska Transportation Center; 2018.

[6] Beason W, Hirsch T, Campise W. *Measurement of Heavy Vehicle Impact Forces and Inertia Properties. Final Report*. College Station, Texas: Texas Transportation Institute, The Texas A&M University System; 1989.

[7] Rasmussen JD, Stolle C, Faller RK, et al. *Investigation and Development of a MASH Test Level 6 Barrier, Phase III*. Lincoln, Nebraska: Midwest Roadside Safety Facility, Nebraska Transportation Center; 2021. Report No. 25-1121-0005-004-13.

[8] Miele CR, Plaxico C, Stephens D, et al. *U26: Enhanced Finite Element Analysis Crash Model of Tractor-Trailers (Phase C)*. Knoxville, TN: Performed by National Transportation Research Center, Inc. University Transporation Center; 2010.

[9] Hallquist JO. LS-DYNA theory manual. *Livermore Softw Technol Corp*. 2006;3:25–31.

[10] Agrawal AK, El-Tawil S, Cao R, et al. *A Performance Based Approach for Loading Definition of Heavy Vehicle Impact Events*. McLean, VA: Federal Highway Administration; 2018.

[11] Cao R, Agrawal AK, El-Tawil S, et al. Performance-based design framework for bridge piers subjected to truck collision. *J Bridge Eng*. 2019;24(7):04019057. doi:10.1061/(ASCE)BE.1943-5592.0001423.

Appendix

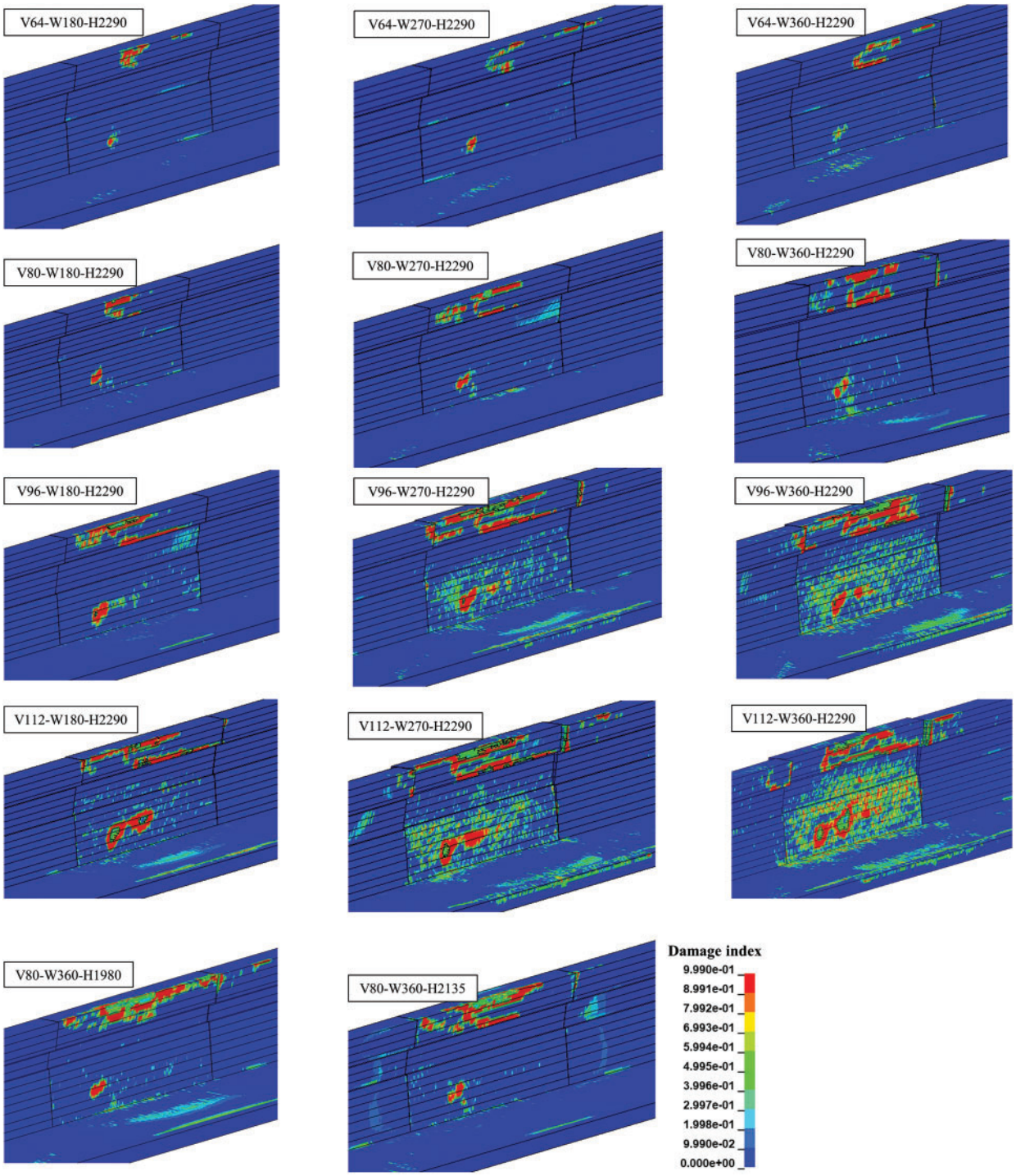

Figure A1. Damage mode of the concrete barrier from the parametric simulations. (V is the speed in kph, W is the weight in kN, and H is the barrier height in mm.)